

**SYNTHESIS AND SPECTROPHOTOMETRIC ACTIVITY OF
PHTHALOCYANINE CONJUGATED TO METAL NANOPARTICLES AND
EVALUATION OF THEIR ANTIBACTERIAL PROPERTIES**

NYAMU N. SAMUEL (MSc. Chemistry)

I84/32254/2015

**A THESIS SUBMITTED IN PARTIAL FULFILLMENT OF THE
REQUIREMENTS FOR THE AWARD OF THE DEGREE OF DOCTOR OF
PHILOSOPHY (CHEMISTRY) IN THE SCHOOL OF PURE AND APPLIED
SCIENCES OF KENYATTA UNIVERSITY**

NOBEMBER, 2021

DECLARATION

This thesis is my original work and has not been presented for a degree or any other award in any University or institution.

Signature..... Date.....

NYAMU NJUGUNA SAMUEL (I84/32254/2015)
Department of Chemistry

SUPERVISORS

We confirm that the work reported in this thesis was carried out and submitted by the candidate with our approval.

Signature..... Date.....

Dr. Eric Masika
Chemistry Department
Kenyatta University

Signature..... Date.....

Dr. Margaret Ng'ang'a
Chemistry Department
Kenyatta University

Signature..... Date.....

Dr. Lucy Ombaka
School of Chemistry and Material Science
Technical University of Kenya

DEDICATION

I dedicate this work to my spouse, Mary Njuguna, my son, Kennedy Njung'wa and daughter Praise Waigwe for their love, encouragement and moral support.

ACKNOWLEDGMENTS

I would like to acknowledge and give all honour and glory to God Almighty for the opportunity to study at Kenyatta University and for His provision and strength throughout my study period.

I am very thankful to my supervisors Dr. Eric Masika and Dr. Margaret Ng'anga of the department of Chemistry, Kenyatta University and Dr. Lucy Ombaka of the department of the School of Chemistry and Material Science, Technical University of Kenya for their expertise, guidance, endless help, encouragement, patience and support throughout my studies. Thank you for giving me the chance to work under your supervision.

I thank Kenyatta University and in particular the department of Chemistry for granting me the opportunity to conduct my research at their facilities. I also wish to thank the technicians in the department of chemistry for their great assistance, my colleagues at the laboratory including Margret Wangeci, Peter Githinji, Benson Wachira and Gerald Mbugua, for their moral support. I am indebted to my employer Teachers Service Commission (TSC) for granting me a study leave to undertake the PhD program. This study was funded by Kenyatta University through the Ministry of Higher Education, Science and Technology in collaboration with Africa Development Bank grant. I also acknowledge additional financial support by Kenya National Research Foundation (NRF2017/2018FY)

Finally, I give thanks to my spouse, Mary Njuguna, daughter Praise Waigwe and Son Ken Njung'wa for their resolute love and support. I also thank my dear mother Jane Waigwe and my brothers, Ken, Job and Jeremy, for their encouragement and constant prayers, May God bless you all.

TABLE OF CONTENTS

DECLARATION.....	ii
DEDICATION.....	iii
ACKNOWLEDGMENTS	iv
TABLE OF CONTENTS	vi
LIST OF TABLES	vi
LIST OF FIGURES	xii
ABBREVIATIONS AND ACRONYMS.....	xv
ABSTRACT.....	xvi
CHAPTER ONE	1
INTRODUCTION.....	1
1.1 Background.....	1
1.2 Statement of the problem and justification	5
1.3 Hypothesis.....	6
1.4 Objectives	7
1.4.1 General objective	7
1.4.2 Specific objectives	7
1.5 Significance and anticipated output	8
1.6 Scope and Limitations of the Study.....	9
CHAPTER TWO	10
LITERATURE REVIEW	10
2.1 Introduction.....	10
2.1.1 Structure of Pc.....	10

2.1.2 Synthesis of metal-free and metallo-Pcs.....	11
2.1.3 Synthesis of substituted Pc (peripheral and non-peripheral position)	15
2.1.4. Spectral properties of Pcs.....	16
2.1.5 Photophysical and photochemical properties of Pc	18
2.1.6 Recent applications of Pcs	24
2.1.7 Pc as photosensitizers in photodynamic inactivation of microbes.....	26
2.2 Metal nanoparticles.....	35
2.2.1 Synthesize of metal nanoparticles.....	35
2.2.2 Applications of metal nanoparticles.....	37
2.2.3 AgNp and their antibacterial activity.....	40
2.2.4 ZnO-Np and their antibacterial activity	41
2.3 Conjugation of Pcs to metal nanoparticles.....	43
2.4 Characterization of Pcs compounds and metal nanoparticles.....	44
2.4.1 Scanning electron microscopy (SEM)	44
2.4.2 Transmission electron microscopy (TEM)	45
2.4.3 Powder XRD.....	47
2.4.4 Fourier-transform infrared spectroscopy (FTIR).....	49
2.4.5 UV-Vis spectroscopy.....	50
2.4.6 Nuclear magnetic resonance (^1H NMR and ^{13}C NMR).....	51
2. 5 Antimicrobial susceptibility tests.....	54
2.5.1 Disk diffusion method.....	54
2.5.2 Minimum inhibitory concentration (MIC).....	55
2.5.3 Minimum bactericidal concentration (MBC).....	55

2.6 Cytotoxicity test	56
CHAPTER THREE	57
MATERIALS AND METHODS	57
3.1 Introduction.....	57
3.1.1 Reagents and chemicals	57
3.1.2 Cleaning of apparatus	58
3.2 Instrumentation	58
3.3 Synthesis of precursors and Pcs	59
3.3.1 Synthesis of 4,5-diiodophthalimide (1).....	59
3.3.2 Synthesis of 4-iodo-5-(3-methoxy prop-1-nyl) phthalimide (2).....	60
3.3.3 Synthesis of zinc Pc (4).....	61
3.3.4 Synthesis of 2,9,16,23-tetraiodo-3,10,17,24-tetra(3-methoxyprop-1-nyl) Pc (5)....	62
3.3.5 Synthesis of 2,9,16,23-tetraiodo-3,10,17,24-tetra(3-methoxyprop-1-nyl) ZnPc (6)	63
3.3.6 Synthesis of synthesis of 4-iodo-5-ethylsulphonyl phthalimide (7)	64
3.3.7 Synthesis of 2,9,16,23-tetraiodo-3,10,17,24-tetraethylsulfonyl Pc (9).....	65
3.3.8 Synthesis of 2,9,16,23-tetraiodo-3,10,17,24-tetraethylsulfonyl ZnPc (10)	66
3.4 Synthesis of metal nanoparticles.....	67
3.4.1 Synthesis of AgNps.....	67
3.4.2 Synthesis of ZnO-Nps.....	68
3.5 Conjugation of metal nanoparticles to Pcs.....	70
3.5.1 Conjugation of AgNps with Pc (6) and (10).....	70
3.6 Determination of photochemical parameters	74
3.6.1 Determination of fluorescence quantum yield (Φ_F)	74

3.6.2 Determination of singlet oxygen quantum yield ($\Phi\Delta$)	75
3.7 Antibacterial studies.....	76
3.7.1 Zone of inhibition using disk diffusion method.....	76
3.7.2 Determination of MIC and MBC.....	77
3.7.3 Cytotoxicity test.....	79
3.8 Complementary analytical techniques	71
3.8.1 UV-Vis absorption studies.....	71
3.8.2 Determination of functional groups using FTIR.....	71
3.8.3 Mass spectroscopy studies	72
3.8.4 Determination of morphology using SEM.....	72
3.8.5 Determination of morphology and particle size using TEM	73
3.8.6 Determination of crystallinity using powder XRD.....	73
3.8.7 ^1H NMR and ^{13}C NMR spectra studies.....	74
3.9 Data analysis	80
CHAPTER FOUR.....	81
RESULTS AND DISCUSSION	81
4.1 Synthesis and characterization of precursors and Pcs.....	81
4.1.1 Synthesis of 4,5-diiodophthalimide (1).....	81
4.1.2 Synthesis of precursors 3 and 7	83
4.1.3 Synthesis of un-substituted ZnPc (4).....	85
4.1.4 Synthesis of metal-free Pc 5 and Pc 9.....	87
4.1.5 Synthesis of Pc 6 and Pc 10.....	88
4.2 Synthesis and characterization of ZnO-Np and AgNp	93

4.2.1 FTIR spectrum of ZnO-Np and AgNp.....	94
4.2.2 Powder XRD analysis of ZnO-Np and AgNp.....	95
4.2.3 SEM and TEM analysis of ZnO-Np and AgNp.....	95
4.2.4 UV-Vis spectroscopy of AgNp and ZnO-Np.....	98
4.3 Conjugation of AgNps nanoparticles to Pcs	100
4.4 Photochemical analysis.....	103
4.4.1 Fluorescence quantum yield Pcs	103
4.4.2 Singlet oxygen quantum yield of the Pcs.....	104
4.5 Antibacterial analysis.....	106
4.5.1 Antibacterial activities of AgNps using disc diffusion test	106
4.5.2 Antibacterial activities of ZnPc, Pc 6, Pc 10 and there silver conjugates	109
4.5.3 Bactericidal and inhibitory minimum concentration of Pcs	117
4.5.6 Cytotoxicity test.....	119
CHAPTER FIVE	121
CONCLUSION AND RECOMMENDATION	121
5.1 Conclusions.....	121
5.2 Recommendations.....	123
REFERENCES.....	125
APPENDICES.....	139
APPENDIX I: Spectrums for synthesized compounds.....	139
APPENDIX 2: Published paper	157

LIST OF TABLES

Table 1.1:	Antibacterial-resistant infection in African countries	3
Table 2.1:	Generation of singlet oxygen and fluorescence quantum yield for various phthalocyanine	23
Table 2.2:	Antibacterial effect of phthalocyanine derivatives	32
Table 3.1:	Preparation of silver nanaoparticles	68
Table 3.2:	Preparation of zinc oxide nanaoparticles	70
Table 4.1:	FTIR bands for precursors 3 and 7	84
Table 4.2:	¹ H NMR and ¹³ C NMR bands for precursors 3 and 7	85
Table 4.3:	¹ H NMR and ¹³ C NMR bands for precursors 4	86
Table 4.4:	FTIR bands for precursors 4 and 9	87
Table 4.5:	Solubility of Pc 6 and 10 in different solvent	88
Table 4.6:	FTIR bands for precursors 6 and 10	89
Table 4.7:	UV-Vis absorption of Pc 6 and 10 in different solvents	90
Table 4.8:	¹ H NMR and ¹³ C NMR spectral data of Pc 6 and 10	92
Table 4.9:	AgNps and ZnO-Nps of different size under different concentrations	96
Table 4.10:	Photochemical parameters for synthesized Pcs in DMSO	105
Table 4.11:	Mean Antibacterial activities of size dependent AgNps	108
Table 4.12:	Antibacterial activities of the synthesized Pcs and their silver conjugate against selected bacteria strains	112
Table 4.13:	Minimum inhibitory concentration (MIC) and minimum bactericidal concentration (MBC) of the Pcs	117

LIST OF FIGURES

Figure 2.1:	Structure of phthalocyanine	10
Figure 2.2:	A selection of Pc synthesis precursors	12
Figure 2.3:	Substitution positions in phthalocyanine	15
Figure 2.4:	Absorption spectrum of Pc showing the B- and Q-band in DMSO	16
Figure 2.5:	Electronic transition in metallo-Pc	17
Figure 2.6:	Jablonski diagram of processes in photosensitive molecules	19
Figure 2.7:	Type I and II mechanism	21
Figure 2.8:	Absorption spectra band observed during the generation of singlet oxygen	22
Figure 2.9:	Application of phthalocyanine	24
Figure 2.10:	Gram-negative and gram-positive cell wall	26
Figure 2.11:	Approaches for synthesis of metal nanoparticles	35
Figure 2.12:	Application of metal nanoparticles	37
Figure 3.1:	Measurement of singlet oxygen generation.	75
Figure 3.2:	Layout of 96 well microtiter plate	78
Figure 3.3:	Conversion of MTT into a purple-colored formazan	80
Figure 4.1:	FTIR spectrum of 4,5-diiodophthalimide (1)	81
Figure 4.2:	UV-Vis spectrum of 4,5-diiodophthalimide (1)	82
Figure 4.3:	¹ H NMR spectrum of 4,5-diiodophthalimide (1)	83
Figure 4.4:	Color of Pc 6 and 10 when dissolved in DMSO	88
Figure 4.5:	UV-Vis spectrum of ZnPc, Pc 6 and Pc 10 in DMSO	91
Figure 4.6:	Distinctive colour of different sized silver nanoparticles	94
Figure 4.7:	TEM and SEM images of AgNps	98
Figure 4.8:	UV-Vis spectra of AgNps	99
Figure 4.9:	UV-Vis spectra of ZnO-Np	100
Figure 4.10:	Conjugation of Pc to AgNp	101
Figure 4.11:	TEM images of (A) Pc 6-AgNps and (b) Pc 10-AgNps	101
Figure 4.12:	FTIR spectra of Pc 6, Pc 10 and their respective AgNps conjugates	102
Figure 4.13:	UV-Vis absorption spectra of Pc 6, Pc 10 and their respective AgNps conjugates	103
Figure 4.14:	Absorption spectra for generation of singlet oxygen	104
Figure 4.15:	Zones of inhibition for AgNps	106
Figure 4.16:	Zones of inhibition of inhibition for Pc 6 and 10 against <i>S. typhi</i> , <i>E. coli</i> and <i>B. subtilis</i>	110
Figure 4.17:	Zone of inhibition for Pcs and AgNps conjugates	116
Figure 4.18:	Image of Vero cell before and after being subjected to Pc 6	119
Figure 4.19:	Image of Vero cell before and after being subjected to Pc 10	120
Figure 4.20:	Line graph of % cytotoxicity against concentration of compound 6 and 10 in µg/ml	120
Figure 6.1:	¹³ C NMR spectrum of 4,5-diiodophthalimide (1)	139
Figure 6.2:	HRMS spectrum of 4,5-diiodophthalimide (1)	139
Figure 6.3:	FTIR spectrum of 4-iodo-5-(3-methoxy prop-1-nyl) phthalimide (3)	140
Figure 6.4:	FTIR spectrum of 4-iodo-5-ethylsulphonyl phthalimide (7)	140

Figure 6.5:	¹ H NMR spectrum of 4-iodo-5-(3-methoxy prop-1-nyl) phthalimide	141
Figure 6.6:	¹ H NMR spectrum of 4-iodo-5-ethylsulphonyl phthalimide (7)	141
Figure 6.7:	¹³ C NMR spectrum of 4-iodo-5-(3-methoxy prop-1-nyl) phthalimide	142
Figure 6.8:	¹³ C NMR spectrum of 4-iodo-5-ethylsulphonyl phthalimide (7)	142
Figure 6.9:	HR-MS spectrum of 4-iodo-5-(3-methoxy prop-1-nyl) phthalimide	143
Figure 6.10:	HR-MS spectrum of 4-iodo-5-Ethylsulphonyl phthalimide (7)	143
Figure 6.11:	FTIR spectrum of ZnPc (4)	144
Figure 6.12:	UV-VIS spectrum of ZnPc (4)	144
Figure 6.13:	¹ H NMR spectrum of ZnPc (4)	145
Figure 6.14:	¹³ C NMR spectrum of ZnPc (4)	145
Figure 6.15:	FTIR spectrum of 2,9,16,23-tetraiodo-3,10,17,24-tetra(3-methoxyprop-1-nyl) Pc (4)	146
Figure 6.16:	FTIR spectrum of 2,9,16,23-tetraiodo-3,10,17,24-tetra ethylsulfonyl Pc (9)	146
Figure 6.17:	FTIR spectrum of 2,9,16,23-tetraiodo-3,10,17,24-tetra(3-methoxy prop-1-nyl) zinc Pc (6)	147
Figure 6.18:	FTIR spectrum of 2,9,16,23-tetraiodo-3,10,17,24-tetraethylsulfonyl zinc Pc (10)	147
Figure 6.19:	UV-Vis spectrum of Pc 6 in different solvent	148
Figure 6.20:	UV-Vis spectrum of Pc 10 in different solvent	148
Figure 6.21:	¹ H NMR spectrum of Pc 6	149
Figure 6.22:	¹ H NMR spectrum of Pc 10	149
Figure 6.23:	¹³ C NMR spectrum of Pc 6	150
Figure 6.24:	¹³ C NMR spectrum of Pc 10	150
Figure 6.25:	XRD spectrum of Pc 6	151
Figure 6.26:	XRD spectrum of Pc 10	151
Figure 6.27:	HR-MS spectrum of Pc 6	152
Figure 6.28:	HR-MS spectrum of Pc 10	152
Figure 6.29:	FTIR spectrum of ZnO-Np	153
Figure 6.30:	FTIR spectrum of glutathione and that of AgNP stabilized with glutathione	153
Figure 6.31:	XRD pattern of ZnO-Np	154
Figure 6.32:	XRD pattern of AgNp	154
Figure 6.33:	UV-Vis spectrum changes of Pc 6 along with the singlet oxygen quantum yield	155
Figure 6.34:	UV-Vis spectrum changes of Pc 6-AgNp with the singlet oxygen quantum yield	155
Figure 6.35:	UV-Vis spectrum changes of Pc 10-AgNps along with the singlet oxygen quantum yield	156

LIST OF SCHEMES

Scheme 2.1	Preparation of phthalocyanine from different precursors	13
Scheme 2.2	Mechanism of phthalocyanine formation	14
Scheme 3.1	Synthesis of 4, 5 diiodophthalimide	60
Scheme 3.2	Synthesis of 4-iodo-5-(3-methoxy prop-1-nyl) Phthalimide	60
Scheme 3.3	Formation of zinc Pc (4)	61
Scheme 3.4	Synthesis of 2,9,16,23 tetra iodo-3,10,17,24-tetra (3-methoxy prop-1-nyl) phthalocyanine	63
Scheme 3.5	Synthesis of 2, 9, 16, 23 tetra iodo-3, 10, 17, 24-tetra (3-methoxy prop-1-nyl) zinc phthalocyanine	64
Scheme 3.6	Synthesis of 4-iodo-5-ethylsulphonyl Phthalimide	65
Scheme 3.7	Synthesis of 2, 9, 16, 23 tetra iodo-3, 10, 17, 24-tetra ethylsulfonyl phthalocyanine	66
Scheme 3.8	Synthesis of 2, 9, 16, 23 tetra iodo-3, 10, 17, 24-tetra ethylsulfonyl zinc phthalocyanine	67

ABBREVIATIONS AND ACRONYMS

AgNp	Silver nanoparticle
AgNps	Silver nanoparticles
AMR	Antimicrobial resistance
AFM	Atomic force microscopy
CMR	Center for Microbiology Research
DBN	1,8-diazabicyclonon-5-ene
DCC	Dicyclohexylcarbodiimide
DCM	Dichloromethane
DMF	Dimethylformamide
DMSO	Dimethyl sulfoxide
DPBF	1,3-diphenylisobenzofuran
DLS	Dynamic light scattering
EDS	Energy dispersive spectroscopy
FTIR	Fourier transform infrared
KBr	Potassium bromide
KEMRI	Kenya Medical Research Institute
MBC	Minimum bactericidal concentration
MIC	Minimum inhibitory concentration
MPc	Metallo phthalocyanine
MTT	3-(4,5-dimethylthiazol-2-yl)-2,5-diphenyltetrazolium bromide
NAD(P)H	Nicotinamide adenine dinucleotide phosphate
Np	Nanoparticles
NCCLS	National Committee for Clinical Laboratory Standards
NMR	Nuclear Magnetic Resonance
PACT	Photodynamic antimicrobial therapy
Pc	Phthalocyanine
Pcs	Phthalocyanines
Pd(II)(OAc) ₂	Palladium acetate
PdCl ₂ (PPh ₃) ₂	Dichloro-bis(triphenylphosphine)-palladium(II)
PDT	Photodynamic therapy
PBS	phosphate buffered saline
SEM	Scanning Electron Microscopy
TEM	Transmission Electron Microscopy
THF	Tetrahydrofuran
TMS	Tetramethylsilane
UV-Vis	Ultraviolet-Visible
WHO	World Health Organization
XRD	X-ray Diffraction Spectroscopy
ZnO-Np	Zinc oxide nanoparticle

ABSTRACT

In recent times, microbial pathogens have increasingly shown multi-drug resistance leading to a growing concern. Analysis of 624 isolates from Kenya revealed 88% of isolates tested were multi-drug resistant. It is estimated that about 4,150,000 deaths will be attributed to antimicrobial resistance (AMR) in Africa by 2050. Therefore, current research is increasingly focusing on antimicrobial photodynamic therapy that utilizes non-toxic photosensitizer exhibiting visible light activity towards the generation of free radicals and singlet oxygen which kill pathogens. The photo-sensitizer may be conjugated to visible-light responsive nanoparticles to further increase their photochemical activities. Phthalocyanine (Pc) is one of the promising dyes that have shown notable photochemical stability, a high degree of aromaticity and ease of structural modification resulting in increased activities. Despite these attractive properties, its antibacterial properties remain under researched. Therefore, this study aimed to tuning the photodynamic antibacterial activity of Pc by using electron withdrawing and electron donating group, conjugating the obtained compounds to silver nanoparticles (AgNps) and zinc oxide nanoparticles (ZnO-Nps) and evaluating the activity of the resulting composites against drug resistant strains *Escherichia coli*, *Staphylococcus aureus*, *Bacillus subtilis* and *Salmonella typhi*. 2,9,16,23-tetra-iodo-3,10,17,24-tetra-(3-methoxyprop-1-nyl) Pc (**6**) and 2,9,16,23-tetra-iodo-3,10,17,24-tetra ethylsulfonyl Pc (**10**) were synthesized respectively. The Pc derivatives were synthesized upon exposure to microwave radiation under solvent-free conditions. Both Pc **6** and **10** were β -form in nature with monoclinic structure confirmed by powder XRD. Pc (**6**) had two absorption bands between 345-364 nm for B-band and 660-680 nm for Q-band while Pc (**10**) indicated two major absorption bands between 354-360 nm for B-band and 685-689 nm bands for Q-band of UV-Vis absorption in different solvents. FTIR confirmed the presence of attached substituent groups to the Pcs. Pc **6** and **10** showed singlet oxygen quantum yield ($\Phi\Delta$) values of 0.53 and 0.63 and fluorescence quantum yield (ΦF) value of 0.14 and 0.13 respectively. The Pc **10** exhibited zone of inhibition $>23\pm 0.12$ $\mu\text{g/ml}$ for all the strains, making it more effective as compared to Pc **6**. In addition, all strains of tested bacteria were susceptible to Pc **10** at a concentration > 31.25 $\mu\text{g/ml}$. This implies that substituting Pc with electron withdrawing allows it to release more singlet oxygen in presence of light and which results to oxidation of the bacterial wall. AgNp and ZnO-Np were synthesized by microwave assisted extraction. The UV-Vis was used to confirm the formation of nanoparticles and also characterization done using FTIR, TEM and SEM. AgNps were of diameters < 58.5 nm that easily conjugated to Pc while ZnO-Nps were of large grain size > 95 , the particles aggregated making it difficult to conjugate with Pcs. Conjugation of Pc **10** with AgNp < 10 nm resulted to a more superior antibacterial as compared to unconjugated Pc **10**. There was no significant different for zone of inhibition for Pc **10** conjugated to AgNp when compared to positive control ciprofloxacin at 500 $\mu\text{g/ml}$ for all the strains except for *B. subtilis*. It had minimum inhibitory concentration (MIC) values of 3.91, 1.96, 1.96 and 15.63 $\mu\text{g/ml}$, for *E. coli*, *S. aureus*, *B. subtilis* and *S. typhi* respectively. Both Pc showed no toxicity on Vero cells at concentration of 600 $\mu\text{g/ml}$. In overall, this work reports the successful tuning of the photo-chemical and antibacterial photodynamic properties of Pc using electron withdrawing and donating substituent. The Pc **10** with electron withdrawing group exhibit superior antibacterial activity which is further enhanced by conjugation with AgNp of < 10 nm.

CHAPTER ONE

INTRODUCTION

1.1 Background

Antibiotics medicines are important both in preventive and curative measures to stop infections caused by microbes by preventing them from reproducing or killing them. For decades, these medicines have been successfully used against a host of microbial infections. However, in the recent past there has been a frightening increase in antibiotic resistance by different bacteria (Wang *et al.*, 2018). Even with extensive research on areas of microbial infections and new arrivals of antibiotics drugs, the morbidity and mortality connected to microbial infections keeps on increasing. In Europe and US alone 50,000 lose their lives each year because of antibacterial-resistant infection. In the United States statistics indicates that more than 2,000,000 people are infected every year with antibiotic resistance diseases with at least up to over 1 % dying as a result of microbial infections (Consumption, 2018). Internationally, there is a growing concern over antimicrobial resistance (AMR) which is currently estimated to account for more than 700,000 deaths per year worldwide. If no appropriate measures are taken to halt its progress, it will cost approximately 10 million lives and about US\$100 trillion per year by 2050 (Tadesse *et al.*, 2017)

In Africa, World Health Organization estimates that 45% of total deaths per year are caused by microbial infections (Okeke and Sosa, 2010). It has been estimated that about 4,150,000 deaths will be attributed to AMR in Africa by 2050, (Taiwo, 2017). Antibiotics

are commonly inaccurately used in Africa resulting in antibiotic drug resistant. Statistics indicate that 36.2% of all patients who seek medication in Africa receive antibiotics, 37.7% of these do not utilize a doctor's prescription with 26.4% relying on self-medication to directly acquire the antibiotics over the counter (Okeke and Sosa, 2010). Isolates obtained from Kenyan patients indicated about 71% of the strain *Staphylococcus aureus* (*S. aureus*) demonstrated multiple resistance to antibiotics (Kimang'a, 2012). Analysis of 624 isolates from Kenya (Kenyatta National Hospital) revealed 88% of isolates tested were multi-drug resistant whereas 26% were extensively-drug resistant (Wangai *et al.*, 2019). *Klebsiella pneumoniae* (*K. pneumoniae*) and *Escherichia coli* (*E. coli*) had poor susceptibility to penicillins, (16–43%), monobactams (8–48%), cephalosporins (22–44%) and trimethoprim-sulfamethoxazole (7%) (Wangai *et al.*, 2019).

In Uganda *S. aureus* and *Pseudomonas aeruginosa* are reported to be resistant to amoxicillin and ampicillin (Frère and Rigali, 2016). Table 1.1 summarizes some African countries depicting high levels of resistance to commonly used antibiotics and the causative agent or disease. For instance, methicillin resistant (80%) *S. aureus* continues to be a problem in most African countries including Kenya. In Mozambique, increasing resistance to ceftriaxone, tetracycline and chloramphenicol has been observed. In Zimbabwe, over 90% of *Neisseria gonococci* (*N. gonococci*) isolates are resistant to trimethoprim and sulfamethoxazole (Kimang'a, 2012).

Table 1.1: The antimicrobial resistance in selected Africa countries

Country	Causative organism/disease	Antibiotic resistance	Ref
Guinea Bissau	<i>Vibrio cholerae</i>	Erythromycin, sulfamethoxazole, ampicillin, nalidixic acid, tetracycline, trimethoprim and aminoglycosides	3
Kenya	<i>V. cholera</i>	Ampicillin, cotrimoxazole, tetracycline and chloramphenicol	3
	<i>S. aureus</i>	Methicillin	1
	<i>E. coli</i>	Streptomycin, cephalosporins, tetracycline, streptomycin, quinolones and ampicillin	1
	<i>Haemophilus influenzae</i>	Amoxicillin, chloramphenicol and sulfamethoxazole	2
Somali	<i>E. coli</i>	Ampicillin, cotrimoxazole, tetracycline, chloramphenicol	
South Africa	<i>Neisseria meningitides</i>	Chloramphenicol	1
Mozambique	<i>N. gonococci</i>	Ceftriaxone and tetracycline	1
Rwanda	<i>Shigella flexneri</i>	Ampicillin, chloramphenicol and trimethoprim	2
Zimbabwe	<i>N. gonococci</i>	Sulfamethoxazole and trimethoprim	1

Source : (¹Kimang'a, 2012, ²Kirika, 2009, ³Okeke and Sosa, 2010)

Due to these increase in drug-resistant microbes there is need for more research for new antibiotics capable to minimize mortality.

Extensive studies are being carried out on photosensitizer and ways to increase their potent activities against microbes have been ongoing (Patir *et al.*, 2018). It is worth noting that effective photosensitizers should have high potential be toxic to bacteria cell when illuminated with light and a decrease in toxicity in the dark, it should be readily soluble in water and high quantum yields culminating in the generation of sufficient singlet oxygen (Belfield *et al.*, 2006; Ragàs *et al.*, 2013).

Different tetrapyrrole structures such as photofrin, phenothiazines, porphyrins, chlorins, bacteriochlorins and phthalocyanine (Pc) with appropriate functionalization have been widely explored as antimicrobials (Abrahamse and Hamblin, 2016a), but most of them exhibit limitations. For example, photofrin which is frequently used as a photosensitizer, has been found to have disadvantages such as limited absorbance at 630 nm reducing its photosensitizing capabilities, it also shows prolonged photosensitivity to the skin which affects the patients (Abrahamse and Hamblin, 2016a).

Current studies are focusing on porphyrins, phenothiazines and phthalocyanine (Pc) as they show high efficiency against microbes (Ghorbani *et al.*, 2018). Amongst these compounds, Pc dyes are potential photosensitizers in photo antibacterial therapy owing to their red light absorption, and the generation of more singlet oxygen due to their high quantum yield (Kaya, 2015). Unsubstituted Pc inherently shows low solubility in most solvents while substituted ones are soluble in water and have notable activity against microbes when irradiated with UV-Vis light (Özdemir *et al.*, 2016). Azo substituted Pc dyes have been reported in most literature as effective pesticides or antimicrobials (Özdemir *et al.*, 2016). Substituting Pc selectively with electron donating or withdrawing groups and conjugating them with metal nanoparticles has been shown to enhance their photo activity under UV-Vis light irradiation (Ghorbani *et al.*, 2018; Rapulenyane, 2013). Their solubility also improves upon substitution with various functional groups at the peripheral position (Meci and Hamuryudan, 2014).

The field of nanotechnology has also found application in medicine in areas such as drug delivery (Nikalje, 2016), diagnosis of diseases (Agnihotri *et al.*, 2014), and dealing with diseases such as diabetes and cancer (Nikalje, 2016). Nanotechnology is also a promising approach towards finding solutions to AMR (Ashe, 2011). Thus necessitating the need for more robust research in this area, in an effort to develop more effective nanotechnologically derived antibacterial agents (Franci *et al.*, 2015).

This study aimed at synthesizing substituted Pc with electron withdrawing and electron donating group, conjugating the obtained compounds to size-dependent Ag nanoparticles and evaluating the activity of the resulting composites against drug resistant strains *Escherichia coli*, *Staphylococcus aureus*, *Bacillus subtilis* and *Salmonella typhi*

1.2 Statement of the problem and justification

The alarming increase in antibiotic resistance by pathogenic microbes has been regarded as one of the main clinical problems facing the modern world (Wang *et al.*, 2018). Over a period of time, antibiotics have been used fight infectious diseases caused by microbes. The fight against infectious diseases has been affected by the emergence of microbes resistant to all classes of antibiotics drugs in use for the past 20 years (Li and Webster, 2018). The spread of these microorganisms all over the world due to movement of people, biochemical changes and mutation may lower the effectiveness of antibiotics against the microbes (WHO, 2014; Consumption, 2018). Resistance of these microbes to drugs has been reported ranging from single to multi-drug resistance. The strain *E. coli* have shown drug resistance to fluoroquinolones and cephalosporins. Methicillin-resistant

exhibited by *S. aureus*, and *S. flexneri* demonstrated drug resistance to fluoroquinolones (Consumption, 2018). As such AMR is a global threat to humanity and a growing concern to researchers from various fields.

The current efforts in research for new antibiotics are not adequate enough to face the increasing rate of drug resistant microbes. To fight this new global health challenges studies are focusing in developing non-toxic, stable, and new antimicrobial therapy that are efficient in fight of drug resistant microbes. The use of photosensitizers dyes are finding use in photodynamic treatment of infection caused by bacteria (Amos *et al.*, 2019). The photosensitizer absorbs visible light in the process they generate reactive oxygen species that destroy pathogenic cells. Their antibacterial properties further increase upon substitution with functional groups at peripheral positions and conjugation to light-responsive metal nanoparticles. Therefore, this study focused on the synthesis and the spectrophotometric activities of Pc substituted with electron donating and withdrawing groups. The compounds were further conjugated to size-depended AgNp and ZnO-Np and their activity against drug-resistant microbial *B. subtilis*, *E. coli*, *S.typhi* and *S. aureus* evaluated.

1.3 Hypothesis

- i. Substituting phthalocyanine with electron-withdrawing and donating groups enhances its photo chemical properties.
- ii. Substituting phthalocyanine with electron-withdrawing and donating groups increases its antibacterial properties.

- iii. There is a significant difference in size of AgNps and ZnO-Nps synthesized using different concentration of the precursors.
- iv. Conjugating phthalocyanine with metal nanoparticles enhances its antibacterial properties.
- v. The conjugated phthalocyanine has no cytotoxic effects on Vero cells.

1.4 Objectives

1.4.1 General objective

To synthesize and characterize phthalocyanine, conjugate the obtained compounds to size-dependent silver and zinc oxide nanoparticles and subsequently determine the composites' antibacterial activity against drug resistant human pathogens.

1.4.2 Specific objectives

- i. To synthesize and characterize phthalocyanine with substituted electron donating and withdrawing groups on the benzene ring.
- ii. To determine the effect of substituting the phthalocyanine with electron donating and withdrawing group on its photodynamic antibacterial activity against drug resistant bacteria *Bacillus subtilis*, *Escherichia coli*, *Salmonella typhi* and *Staphylococcus aureus*.
- iii. To conjugate the size-dependent zinc oxide and silver nanoparticles to Pc substituted with electron donating and withdrawing group and to evaluate the activity of the resulting composites as photodynamic antibacterial agents against *Bacillus subtilis*, *Escherichia coli*, *Salmonella typhi* and *Staphylococcus aureus*.

- iv. To determine the cytotoxic effects of the compounds against the Vero cells.

1.5 Significance and anticipated output

This work fundamentally contributes to the field of medicine by use of photosensitizers as antibacterial. Pcs have been used in many applications such as in nonlinear optical materials and as photosensitizers for photo dynamic therapy (PDT), and recent advances in photodynamic antimicrobial therapy (PACT). These uses require Pcs to have high triplet state and be able to generate singlet oxygen. Studies have shown Pcs generates singlet oxygen quantum yields by introduction of different substituents and central metal attached to it. A key limitation of the Pc is the poor water solubility and aggregation in aqueous environment (Nwahara, *et al.*, 2017).

Inclusion of electron donating or withdrawing group on peripheral of the Pc may increase singlet oxygen production and solubility, which is important for Pc as photodynamic effects. We thus combined Pc with electron donating (methoxyprop-1-nyl) and withdrawing group (ethylsulfonyl) for possible enhancement of singlet oxygen generating capacity. The study also explored the effects of combining metal nanoparticles on the photo physical behavior of Pc substituted with electron donating and withdrawing group. Metal nanoparticles particularly AgNps and ZnO-Nps have been very effective in supporting antimicrobial activities (Mondal and Bera, 2014). The metal nanoparticles can potentiate antibacterial Pc by improving photosensitizer solubility, and photochemistry optimizing the rate of production of singlet oxygen.

Therefore, this study focused on the synthesis and the spectrophotometric activities of Pc substituted with electron donating and withdrawing group. The compounds were further conjugated to size-dependent AgNps and ZnO-Nps and their activity against drug-resistant microbial *B. subtilis*, *E. coli*, *S. typhi* and *S. aureus* evaluated. The tuned Pc is anticipated to generate more singlet oxygen that will generate oxidative stress induction against microbes. This action in turn will make it difficult for bacteria cells to become resistant to Pc thus finding use in antibiotic delivery, wound healing, implantable devices and antibacterial coatings.

1.6 Scope and Limitations of the Study

Substituent groups that are either electron-donating (like alkoxy, alkylthio, aryloxy, thioalkyl and hydroxyl) or electron-withdrawing (such as nitro, halo, carboxylic and arylsulfonyl) successfully attached to Pc increases the photo-physical and chemical activities. This study only used an alkoxy as an electron-donating group and arylsulfonyl as an electron-withdrawing group attached substituted to the Pc. Antimicrobial properties of phthalocyanine can also be improved by conjugating it with nanoparticles, this study was selective and only used zinc oxide and silver nanoparticles shown in literatures to have antibacterial activities though underutilized. The study also only focused on the susceptibility of bacteria on synthesized Pc conjugated to the nanoparticles, the mechanism for antibacterial activity was not determined

CHAPTER TWO

LITERATURE REVIEW

2.1 Introduction

This section covers relevant literature on antimicrobial photo dynamic therapy (PDT) and using Pc as photosensitizers. Additionally, the principles of complementary analytical techniques including scanning electron microscopy (SEM), transmission electron microscopy (TEM), powder X-ray diffraction (XRD), ultraviolet-visible (UV-Vis), fourier transform infrared (FTIR) and nuclear magnetic resonance (NMR) are summarized

2.1.1 Structure of Pc

The chromogen metal free Pc Figure 2.1, first came in limelight in 1930s after being discovered by Linstead (Denekamp *et al.*, 2019) and reported as a vital chromogen. Since then, numerous accounts has reported its usage in diverse fields (Wöhrle *et al.*, 2012).

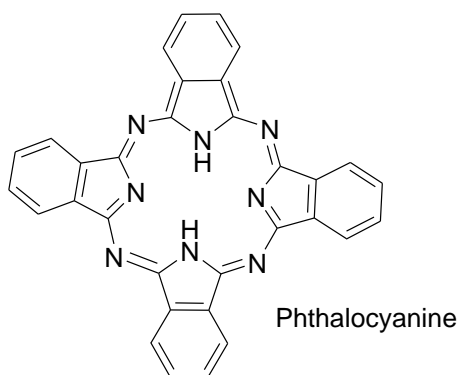


Figure 2.1: Structure of metal free Pc

The name Pc is coined from two words ‘phthalic’ acid as a precursor and ‘cyanine’ because of its color. Pc has a structure that resembles that of porphyrins, with 4 isoindole units joined by nitrogen atoms.

The basic structure of Pc consists of tetrapyrrolic and macrocyclic rings attached to planar shape aromatic compounds. They have 18 delocalized π -electrons that alternate between the nitrogen and carbon atoms (Denekamp *et al.*, 2019). Owing to their extensive 18- π electron cloud conjugation, Pc exhibit strong absorptions towards the red region of the visible spectrum. Numerous methods have been developed to synthesis Pcs with a great part of them involving cyclotetramerization of small molecules (Mohammed and Kareem, 2017).

2.1.2 Metal-free and metallo-Pcs

Synthesis of unsubstituted metal-free Pc has been achieved using the ortho-substituted benzene precursors depicted in Figure 2.2. These precursors include phthalimide, phthalic acid, 1,3-diiminoisoidoline, phthalonitrile amongst other compounds (Mohammed and Kareem, 2017). The most commonly used precursors are phthalonitrile and phthalic anhydride. Phthalonitriles are mostly used due to their good yields of Pcs (Staicu *et al.*, 2013). On the other hand, phthalic anhydride is chosen in bulk production of Pcs since is relatively affordable (Salia *et al.*, 2012)

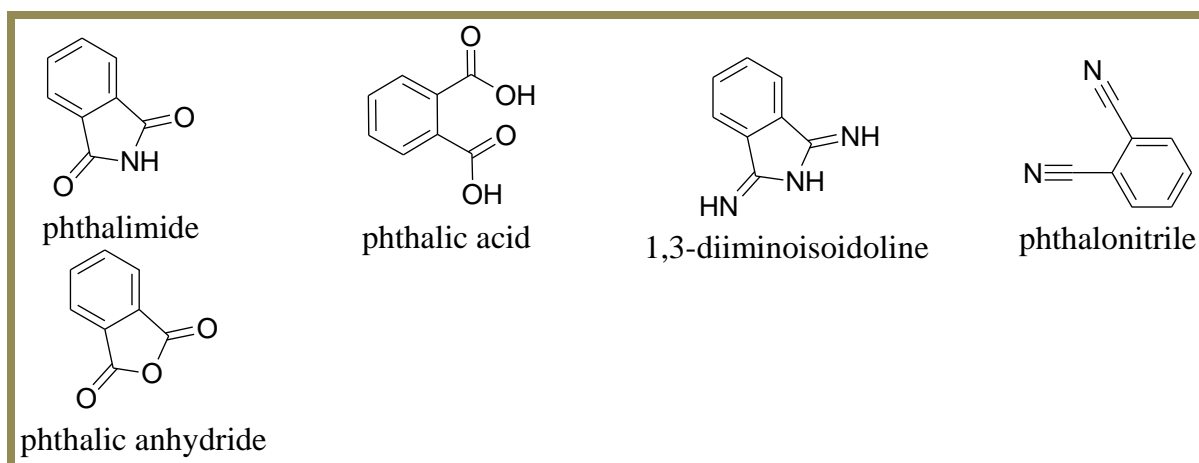
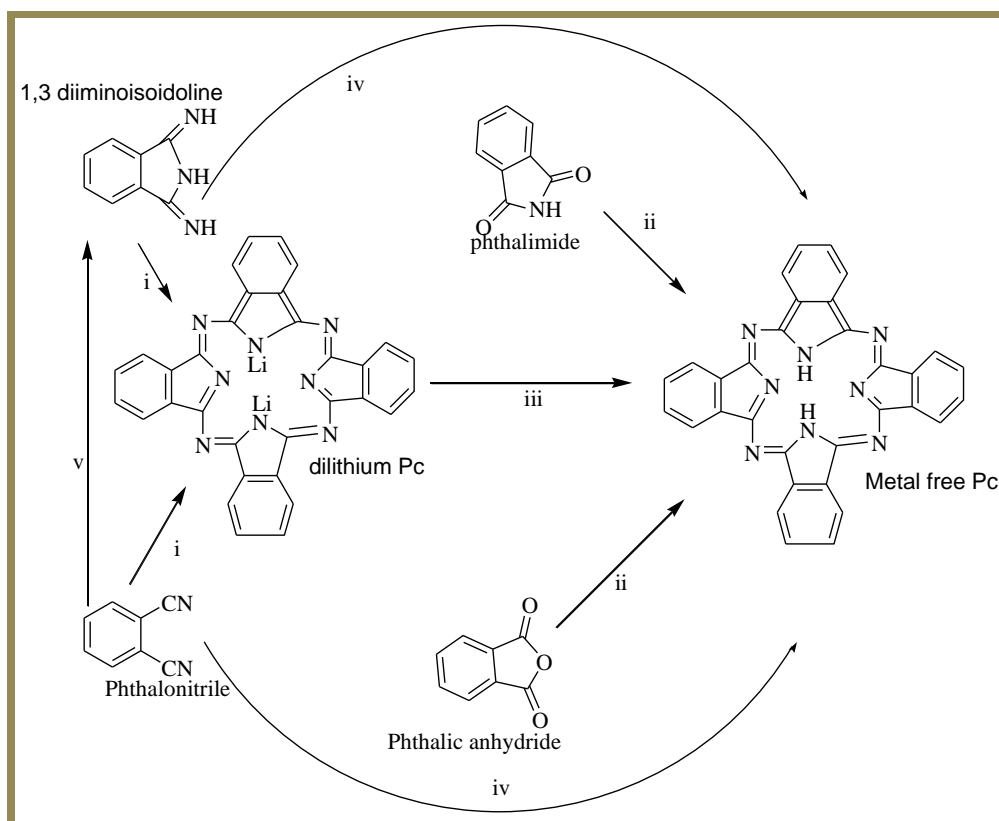


Figure 2.2: A selection of Pc synthesis precursors

Scheme 2.1 shows various routes used to prepare metal-free Pc. Firstly, 1,3-diiminoisoindoline or phthalonitrile as precursor following route **i** involves a condensation reaction. This is done by refluxing with lithium to form dilithium Pc. Reaction of dilithium Pc with dilute HCl *via* route **iii** ends up forming metal-free Pc. Alternatively, Pc can directly be synthesized from the two precursors (1,3-diiminoisoindoline and phthalonitrile) by heating *via* route **iv** at 160°C-170°C for 24 h in the presence of pentanol and 1,8-diazabicyclonon-5-ene (DBN). Phthalonitrile can be converted to 1,3-diiminoisoindoline *via* route **v** by bubbling ammonia through a solution of phthalonitrile. Then 1,3-diiminoisoindoline can then be condensed to phthalocyanine by heating to reflux in dimethylaminoethanol. Lastly, Pc can also be synthesized by the direct heating of phthalic anhydride or phthalamide in a solvent with high boiling point containing urea as depicted in route **ii** (Chauhan *et al.*, 2003). A greener approach towards synthesizing metallo-Pc is the solvent-free reaction of hydrated metal salts and phthalonitrile under microwave irradiation (Staicu *et al.*, 2013). Compared to reaction in solvents, solvent-free reactions are environmentally benignant, require shorter reaction periods and

simplify the product isolation procedures (Ombaka, *et al.*, 2014). Metallo-Pcs are prepared using a procedure similar to that of metal-free Pc with the exception that the condensation is achieved by the direct addition of the required metal salt.

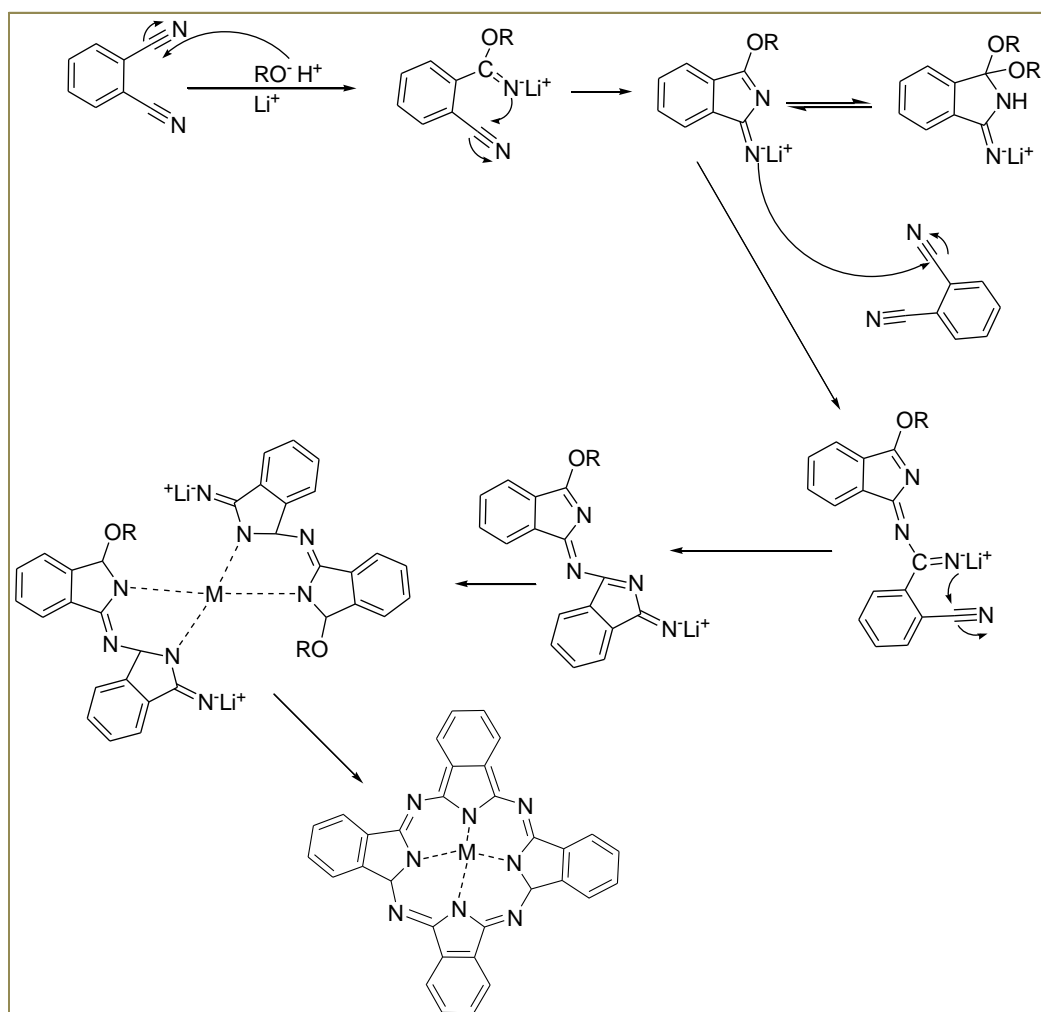


Scheme 2.1: Schematic routes for synthesis of Pc from precursors

Synthesis of substituted Pc can be done *via* the peripheral (β) or non-peripheral (α) positions of the planar macrocycle structure of Pc, or at axial center position where metals can attach (Kim *et al.*, 2015). Such substituents greatly increases the optical and chemical properties of the Pc increasing their applicability in the field of science (Nemykina and Lukyanets, 2010).

2.1.3 Mechanism of phthalocyanine formation

A proposed mechanism for formation of phthalocyanine was proposed by Linstead. It involves nucleophilic attack of phthalonitrile by an alkoxide ion to form monomeric alkoxyiminoisoindolenine intermediate. The intermediate reacts with another phthalonitrile to form dimeric intermediate, which may undergo self-condensation to form tetrameric intermediate. This latter undergoes ring cyclization with a two electron reduction to form phthalocyanine as shown in scheme 2.2 (Staicu *et al.*, 2013).



Scheme 2.2: Mechanism of phthalocyanine formation

2.1.4 Peripheral and non-peripheral substitution in Pc

Research has shown that substitution of a functional group on the macrocyclic ring of Pc can happen at peripheral position or at non-peripheral position (Isci and N-bridged, 2013). As such, the Pc has 16 positions where substituent functional group can occur on the macrocyclic ring as shown in the Figure 2.3 (Jianjun, 2006).

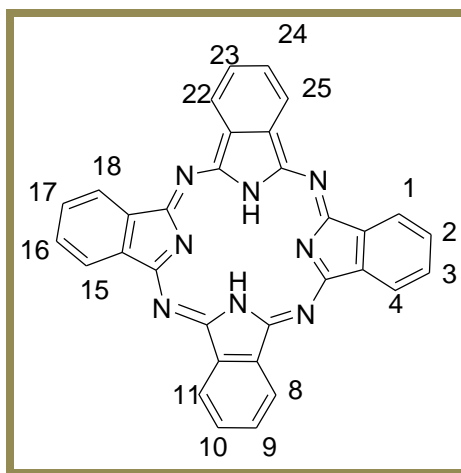


Figure 2.3: Positions where functional group can attach on Pc

Substitutions happening at 2,9,16, and 23 or 2,3,9,10,16,17,23 and 24 are termed as peripheral substitutions (β -position) while those at 1,4,8,11,15,18,22, and 25 or 1,8,15, and 22 positions are termed as non-peripheral substitutions (α -position) (Kim *et al.*, 2015). Substituent groups successfully attached to Pc to increase the photo-physical and -chemical activities include amines, ethers, alkyls and thiols among others. These functional groups also help to increase the solubility of Pc in polar solvent (Chernonosov *et al.*, 2014). Spectral properties of metal-free Pc and metallo-Pc are determined mostly by the Q-band which originates from π - π^* transition within the macrocyclic ring. The absorption of Q-band is important in forming new Pcs derivatives for particular

applications. The peripheral or non-peripheral substitution, nature of central metal and conjugation with metal nanoparticles affects the spectra and hence the properties of Pcs compounds.

2.1.5. Spectral properties of Pcs

The spectral properties of Pcs originate from their 18π electron system. The UV-Vis spectra of metallo-Pc have an intense Q-band between 650-720 nm appearing in the red region in the electromagnetic spectrum. Another weaker band is observed between 300-400 nm representing the B-(SORET) band (Figure 2.4) (Tayfuroğlu *et al.*, 2018). The positioning of the B- and Q-bands is based on the Gouterman's four-orbital model (Figure 2.4) (Fukuda *et al.*, 2010).

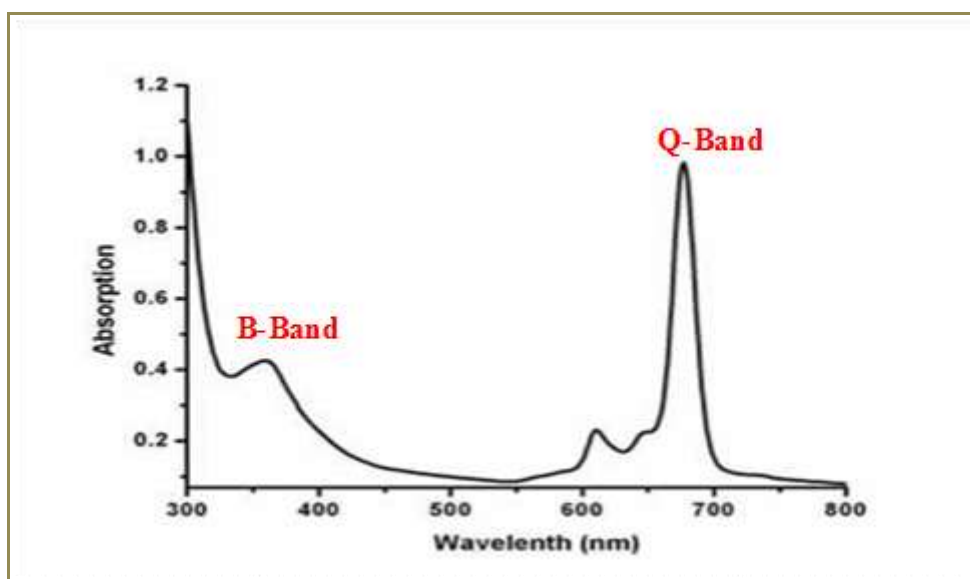


Figure 2.4: Absorption spectrum of Pc showing the B- and Q-band in DMSO

The model explains the transitions from a_{1u} , a_{2u} and b_{2u} , where the mentioned bands originate. The transition happening at a_{1u} highest occupied molecular orbital (HOMO) to

a doubly degenerate transition e_g of the lowest unoccupied molecular orbital (LUMO) results to Q-band while the shift from the a_{2u} or b_{2u} of the highest occupied molecular orbital to the e_g of the lowest unoccupied molecular orbital result in the B-bands (Figure 2.5)

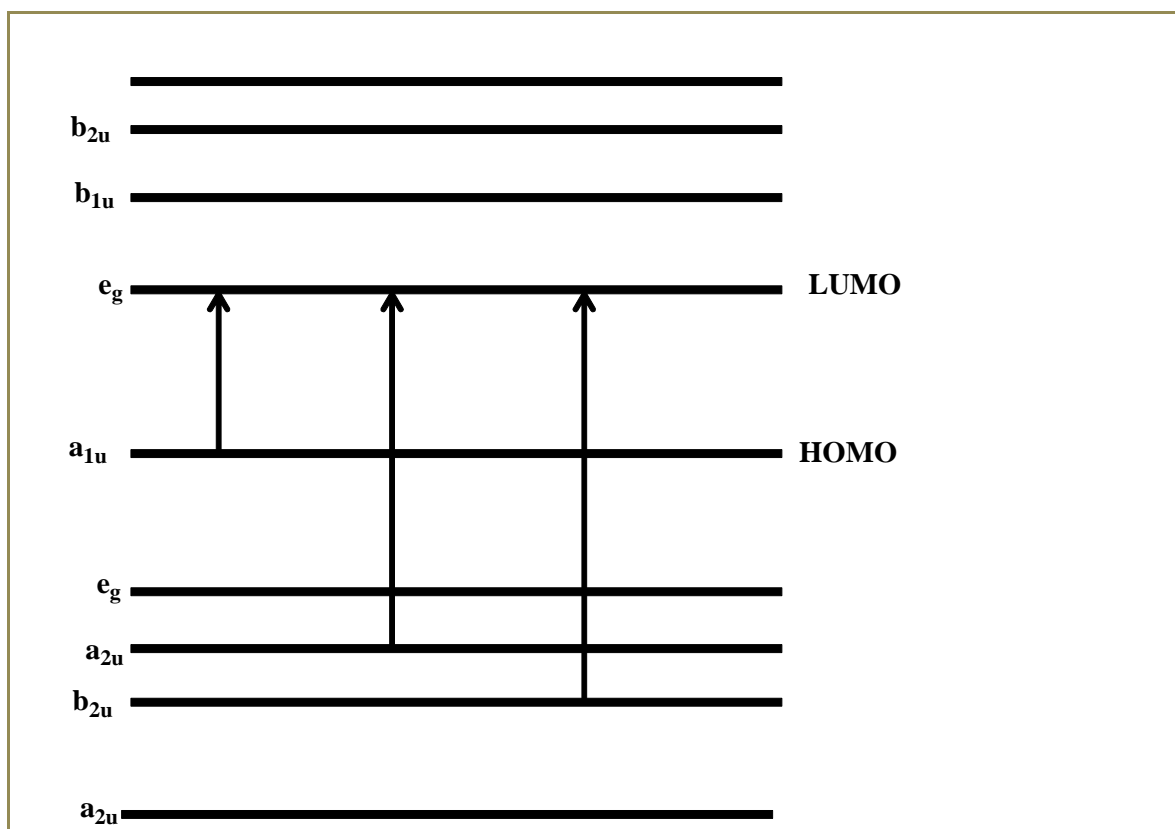


Figure 2.5: Electronic transition in metallo-Pc

The intensity, position and appearance of B- and Q-bands depend on axial metal, peripheral substitution, and the solvent used (Furuyama *et al.*, 2019). Symmetric substitution of Pc alters the optical properties of Pc and may cause a red or blue shift of the B- and Q-band depending on the type of substituents. When substitution of a functional group occurs at α -positions Pcs are usually more red-shifted compared to the β -position substituted (Furuyama *et al.*, 2019). Substitutions with electron withdrawing

and donating group at the α and β affects the Q- and B-band (Güzel *et al.*, 2019). The attachment of electron-donating functional group, like alkoxy, alkylthio, arylox, thioalkyl and hydroxyl at the four α -positions moves the Q-band to longer wavelengths because it raises the energy level of the HOMO. Electron-donating functional groups at the β -positions results to Q-band getting blue shifted. Substitution with electron-withdrawing groups such as nitro, halo, carboxylic and arylsulfonyl functional groups at the four α -positions, results in a blue shift of the Q-band, while substitution of the functional group at β -position leads to a red shift of the Q-band. The energy level of the α -carbons in the HOMO level are larger than those at the β -carbons (Nemykina and Lukyanets, 2010). The Pcs are most used compounds as photosensitizers since they have suitable photo-physical and photo-chemical properties.

2.1.6 Photo-physical and photo-chemical properties of Pc

The photo-physical processes in a molecule have the potential to influence its chemical properties. The mechanism of photo-physical and photo-chemical of Pc occur during relaxation processes are described using Jablonski diagram Figure 2.6 (Sakamoto and Ohno-okumura, 2009).

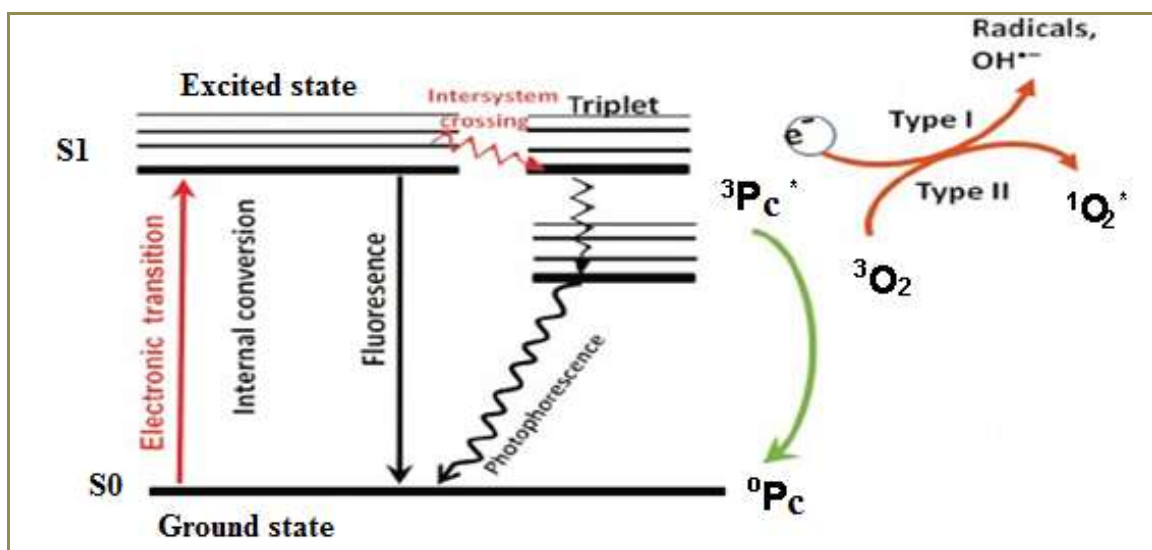


Figure 2.6: Jablonski diagram of processes in photosensitive molecules

Following absorption of a photon of a specific energy the Pc gets excited from ground level (S_0) to the first excited state (S_1). In terms of molecular orbital (MO), the excitations can be explained by elevation of electrons to upper MO ($\pi \rightarrow \pi^*$ transitions). Once excitation has taken place, the excited Pc (Pc^*) transit back to the ground states (Sakamoto and Ohno-okumura, 2009). This may happen by vibrational relaxation and internal conversions *via* the first excited state (Staicu *et al.*, 2013). The de-excitation occurs by fluorescence (radiative) or heat emission (non-radiative) (Nombona, *et al.*, 2012). It can also undergo a spin change through intersystem crossing to the triplet state, a process that occurs because of spin inversion (Jianjun, 2006). In the triplet excited state, $^3Pc^*$ follow the route to the ground state *via* radiative or non-radiative a process termed as phosphorescence. The $^3Pc^*$ can undertake two types of reactions; type I and type II mechanisms Figure 2.6. Therefore, Pcs undergoing through these photodynamic reactions will undergo intersystem crossing to the triplet state or fluorescence emission and as a result brings about photochemical reactions (Tahershamsi *et al.*, 2019)

2.1.6.1 Fluorescence emission

Fluorescence can be defined as release of light energy by a compound that has absorbed light. It happens when excited molecule, relaxes to a low energy state through emission of a photon Figure 2.6. It may have been directly excited at the ground state (S_0) and taken to singlet state by absorption of a photon of energy and subsequently emits a photon of a lower energy as it relaxes to ground state. Fluorescence emission occurs between 550-800 nm due to conditions such metal attached to Pc, solvents used and macrocycle substituents (Jianjun, 2006). The effectiveness of fluorescence mechanism can be calculated by the Φ_F , given by dividing the number of emitted photons by the number of absorbed photons (Gümrukçü *et al.*, 2014).

$$\Phi_F = \frac{\text{Numbers of photons emitted}}{\text{Numbers of photons absorbed}} \dots\dots\dots \text{Equation 2.1a}$$

$$\Phi_F = \Phi_F(\text{std}) \times \frac{F \times A(\text{std}) \times n^2}{F(\text{std}) \times A \times n^2(\text{std})} \dots\dots\dots \text{Equation 2.1b}$$

The Φ_F of unknown Pc can be calculated *via* a comparative method as depicted in **Equation 2.1 (a and b)**, Where A and A(std) represents absorbance of sample and standard respectively. The $\Phi_F(\text{std})$ represent fluorescence quantum yield of the standard, F and F(std) represent areas of fluorescence emission curves covered by the Pc and standard respectively (Sakamoto and Ohno-okumura, 2009). The **n** and **n(std)** represent the refractive index of the solvent used to dissolve the sample and standard (Gümrukçü *et al.*, 2014). Another route Pc can follow to bring about photochemical reactions is intersystem crossing.

2.1.6.2 Intersystem crossing

The Pc may undergo transition through intersystem-crossing to triplet state ($^3\text{Pc}^*$). The $^3\text{Pc}^*$ always has a much lower energy compared to that of singlet state, but has longer lifetime (10^{-3} s). The Pcs in the $^3\text{Pc}^*$ can transit to the ground state *Via* phosphorescence route or interacts with oxygen in either of the two reactions by type I or type II mechanism Figure 2.6.

The type I reaction mechanism, the $^3\text{Pc}^*$ can transfer electrons to surrounding substrate to generate free radical, like hydroxyl radical (HO^*) and superoxide anions (O_2^-) (Liang *et al.*, 2016 ; Jianjun, 2006). In the presence of oxygen, the radicals can react further to form an oxygenated product like hydrogen peroxide (H_2O_2). These generated products affect the functionality of the microbial cells when they come into contact with cell wall (Cieplik *et al.*, 2014; Sakamoto and Ohno-okumura, 2009). In type II reaction mechanism the excited Pc release energy from the $^3\text{Pc}^*$ to the oxygen, forming electronically excited and highly reactive singlet oxygen ($^1\text{O}_2$) Figure 2.7 (Rapulenyane, 2013). The formed singlet oxygen is very toxic to cell tissues of the targeted microbes resulting to their death.

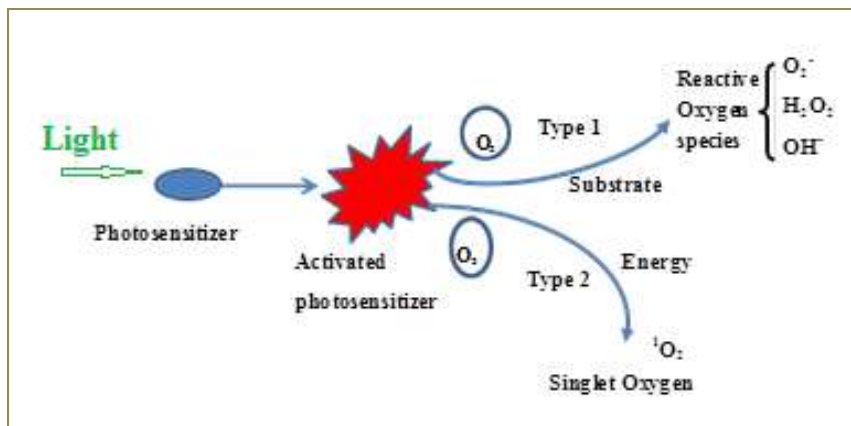


Figure 2.7: Type I and II mechanism

2.1.6.3 Singlet oxygen

The singlet oxygen quantum yield ($\Phi\Delta$) can be defined as the efficiency of a compound or molecule to produce $^1\text{O}_2$. This happens when $^1\text{O}_2$ is produced mainly *via* type II photosensitization methods whereby energy transition happens from the $^3\text{Pc}^*$ to ground state oxygen. The value of the $\Phi\Delta$ is determined either by a photophysical method or by a photochemical method. The photochemical method uses a singlet oxygen scavenger which is a compound that reacts with a released singlet oxygen. Examples of scavengers include furan, guanine and 1,3-diphenylisobenzofuran (DPBF). To measure the $\Phi\Delta$ of Pc *via* photochemical method, the Pc under investigation is mixed with a scavenger like DPBF and decay monitored for an irradiation period using a UV-Vis spectrophotometer. The release of $^1\text{O}_2$ is inferred from disappearance of the DPBF scavenger absorption band at 417 nm as depicted in Figure 2.8 (Rapulenyane, 2013).

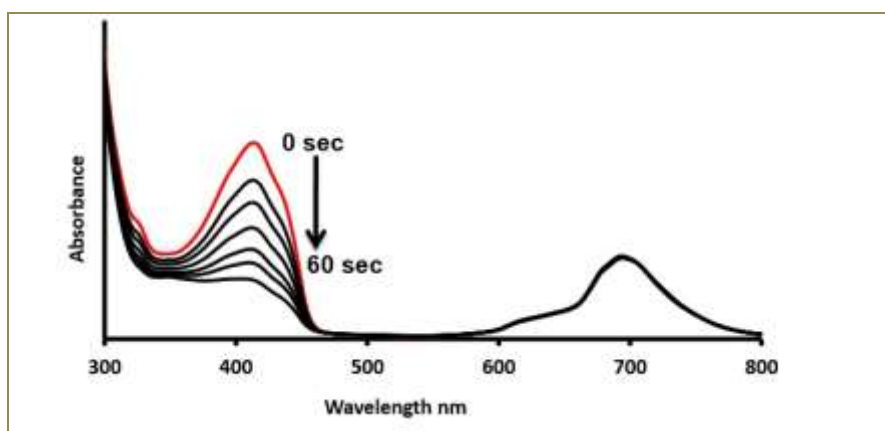


Figure 2.8: Absorption spectra band observed during the generation of singlet oxygen

The DPBF is preferred since its decomposition products do not affect the detection of the quencher or react with either the Pc or the $^1\text{O}_2$ generated. It also reacts immediately with the $^1\text{O}_2$ in organic solvents without any side reactions. The value of $\Phi\Delta$ is then determined using **Equation 2.2** (Gümrükçü *et al.*, 2014).

$$\Phi\Delta = \Phi_{\Delta}^{\text{std}} \times \frac{R I_{\text{abs}}^{\text{std}}}{R^{\text{std}} I_{\text{abs}}} \dots \dots \dots \text{Equation 2.2}$$

Where I_{abs} and $I_{\text{abs}}^{\text{std}}$ are the rates of light absorption by the Pc being determined and the standard respectively. The $\Phi_{\Delta}^{\text{std}}$ is the $^1\text{O}_2$ quantum yield of the standard 0.56 in dimethylformamide (DMF), \mathbf{R} and \mathbf{R}^{std} are quencher DPBF photo bleaching rates in the presence of the respective Pc being determined and the standard respectively. Table 2.1 shows various singlet quantum yield and quantum fluorescence yield generated by different Pc either attached to functional groups or metal cations.

Table 2.1: Fluorescence (Φ_F) and Singlet oxygen (Φ_Δ) quantum yield of Pcs in dimethyl sulfoxide (DMSO)

Metal Pc	Substituents	Φ_Δ	Φ_F	Ref
ZnPc	-	0.67		(Staicu <i>et al.</i> , 2013)
ZnPc	Fluconazole	0.14	0.19	(Cormick and Durantini, 2018)
ZnPc	1-(4-bromophenyl)ethanol	0.67	0.10	(Manieri <i>et al.</i> , 2015)
ZnPc	Enantioenriched (R) 1-(4-bromophenyl)ethanol	0.76	0.12	(Manieri <i>et al.</i> , 2015)
ZnPc	Enantioenriched (S) 1-(4-bromophenyl)ethanol	0.65	0.10	(Manieri <i>et al.</i> , 2015)
ZnPc	(1,2-diethylaminoethylthiol)-2-(captopril)	0.26	0.10	(Rapulenyane, 2013)
ZnPc	(1,2-diethylaminoethylthiol)-2-(captopril) with AgNp	0.57	0.06	(Rapulenyane, 2013)
ZnPc	Tetra sulfonyl	0.30	0.36	(Nyokong, 2007)
ZnPc	Phenoxy	0.60	-	(Nyokong, 2007)
ZnPc	Tertbutyl phenoxy	0.73	-	(Nyokong, 2007)
FePc	-	0.90	-	(Staicu <i>et al.</i> , 2013)
AlPc	Hydroxyl	0.41	-	(Staicu <i>et al.</i> , 2013)
AlPc	Tetra sulfonyl	0.36	0.35	(Nyokong, 2007)

2.1.7 Recent applications of Pcs

The macrocyclic nature of Pcs enables their application in different fields that take advantage of their distinctive chemical and optical properties that can be modified to absorb into near infrared. The uses of the Pcs due to the special chemical and optical properties are diverse and entail many applications, such as catalysis, data storage, pigments, photodynamic therapy, chemical sensors and solar cells (Figure 2.10).

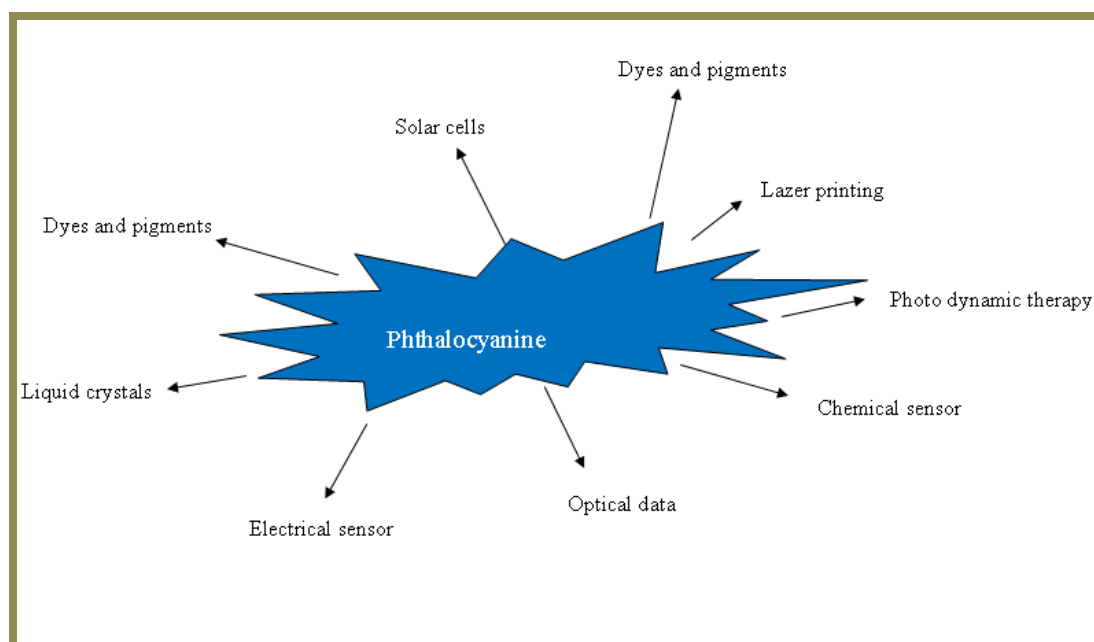


Figure 2.10: Application of Phthalocyanine

Amongst the numerous uses of Pcs (Figure 2.10) are increasingly being used as liquid crystals applicable as organic semiconductors of high viscosity and bulk mobility (Hanna, 2005). Derivatives of Pc such as copper Pcs are also being used in solar cells due to their longer exciton, wide spectral range high hole mobility (Walter *et al.*, 2010; Linares-flores *et al.*, 2015). In catalysis; metallo-Pc are widely used to degrade industrial waste by catalytic oxidation over a metallo-Pc complex catalyst (Bata, 2014). Pcs also shows promising applications in chemical sensors. For instance, Braik *et al.*, (2015) used a Co (II) Pc acrylate polymer to detect perchlorate anions. It is also used in photodynamic therapy of cancer in the field of medicine because they can be tuned to have long-wavelength absorption in the near-infrared. Pc derivatives are also promising photosensitizers applicable as antimicrobials (Ghammamy *et al.*, 2012).

2.1.8 Phthalocyanine as photosensitizers in photodynamic inactivation of microbes

Certain accounts report the development of novel Pc with improved inactivation properties against microbial pathogens both for gram-negative and gram-positive-bacteria (Rapulenyane, 2013).

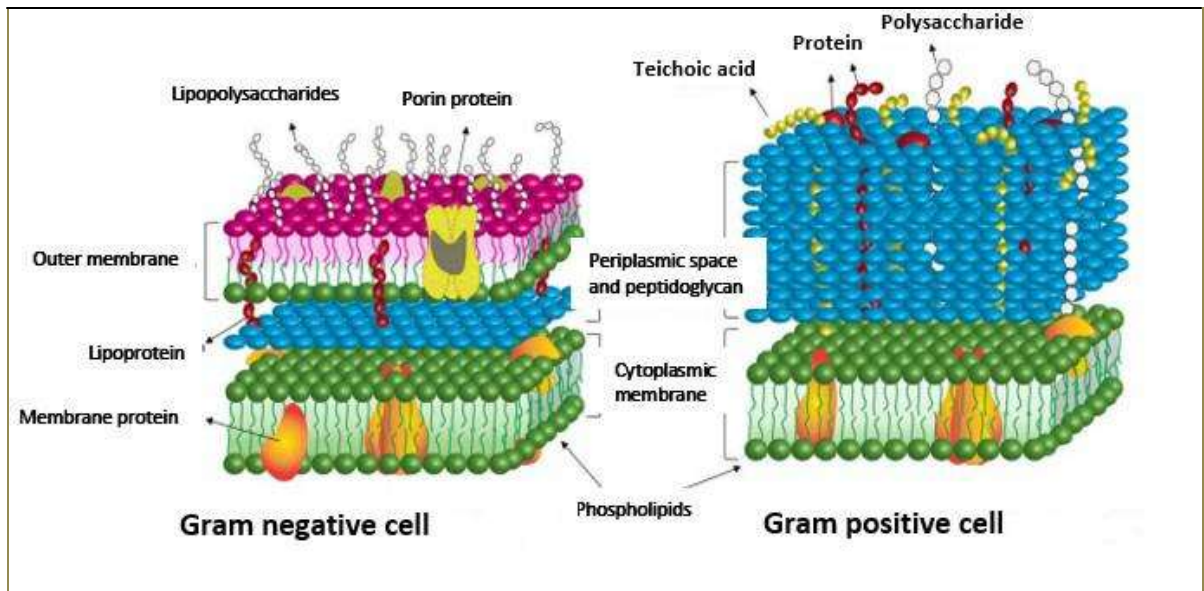


Figure 2.11: Gram-negative (left) and –positive (right) cell walls (Amos-Tautua *et al.*, 2019)

Various research done have shown gram-positive bacterial are more susceptible to Pc compounds as compared with gram-negative. This is because gram-negative bacteria have lipopolysaccharides as the main constituent in their outer membrane surface (Beveridge, 1999). It act as a barrier for the bacteria against chemicals and other materials that may penetrate the cell membrane interfering with internal make up such as the lipid bilayer Figure 2.11 (Liu *et al.*, 2015). The anionic in nature of the lipopolysaccharide cell wall makes it an vital for pathway for cationic Pcs compound (Friedrich *et al.*, 2000). Another constituents of outer layer of gram-negative bacteria is

phospholipid layer (Cieplik *et al.*, 2014; Ruiz-gonzález *et al.*, 2015). It is an effective barrier for bacteria against toxic substance from outside, rendering gram-negative bacteria to be resistant to various antibiotics drugs (Manieri *et al.*, 2015). This phospholipid lining comprises of bio-membranes that are hydrophilic in nature, making them permeable to water-soluble Pcs compounds (Liu *et al.*, 2015). Permeability to water soluble compounds decreases toward the center of the bilayer (Nikolić *et al.*, 2014).

Although Pcs have shown promise in the fight against microbes, improvements are still necessary to enhance their antimicrobial performance. Photodynamic inactivation of bacteria is based on photosensitizers which absorb light and generate reactive oxygen species, killing cells via oxidation. Photodynamic inactivation is evaluated by comparing viability with and without irradiation, where reduction of viability in the presence of the photosensitizer without irradiation is considered as dark toxicity. Good Pcs photosensitizers that are effective against microbes should have the following properties, first it should show no or minimal dark toxicity towards a given cell or tissues. Secondly it should be readily removed from normal tissue in order to reduce phototoxic side effects (Abrahamse and Hamblin, 2016a). Another property it should possess is to have high long-wavelength absorption in the near-infrared to enable the formation good yield of $^1\text{O}_2$ in presence of light. It should have quantum yields $\Phi\Delta > 0.4$ to be effective against microbes. In addition, it should also possess high microbe binding affinities and low binding affinity to mammalian cells (Cieplik *et al.*, 2014; Ragàs *et al.*, 2013). A significant amount of research has also been dedicated to develop Pcs with the following modified properties, solubility in water, nature of charge, central metal atom, charge

distribution, amphiphilic character, functional groups, and conjugation with metal-nanoparticles.

A major drawback in the utilization of potent Pcs as antimicrobials is their hydrophobic nature resulting in low water solubility (Meci *et al.*, 2014). The solubility of Pcs is important in determining its photo-physical and photo-chemical parameters (Kirika, 2009). This has prompted modification of the Pcs macrocyclic structure to improve its efficiency and optimize its performance as antimicrobial (Denis and Hamblin, 2011). The solubility of Pcs compounds can be enhanced by attaching substituent groups such as ethers, sulfonyls, amines, alkyls and thiols chains at the β -region in macrocyclic of the Pc (Staicu *et al.*, 2013).

Another factor that contributes to antimicrobial property of a Pc is the nature of charge attached to it. The cationic Pcs work by competing with positively charged ions like Ca^{2+} and Mg^{2+} ions found on the surface of microbes that helps to stabilize the cell membrane (Liu *et al.*, 2015). These cationic ions Pcs deteriorate the outer cell membrane of the microbes allowing the intake of Pc that will incapacitate the bacteria metabolic activities. Rapulenyane worked on tetrasulphonate and tetrapyradin zinc Pc as antimicrobials (Rapulenyane, 2013). From these work it is clear that balance between charge and hydrophobicity is significant function in deactivation of microbes (Rapulenyane, 2013). Synthesized Pcs with different cationic charges have been effective against gram-negative bacteria, the *E. coli* were found to be susceptible when subjected to water-soluble Pcs made synthesized with different cationic charges (Rapulenyane, 2013).

A chromium (III) Pc chloride complex synthesized by Mugdad, 2016 had a high activity against *Pseudomonas aeruginosa*, *E. coli* and *S. aureus* with zone of inhibition of 12, 10 and 9 mm respectively. The complex had negligible activities against the fungal *Aspergillus flavus* and *Candida albicans* species (Mugdad, 2016). The sensitivity of this complex against the bacteria may be as results of hydrogen bonds and the tertiary nitrogen of the macrocyclic ring of Pc with that of bacteria cell. The whole process interferes with the metabolic processes of the normal cells in microbes (Mugdad, 2016). Furthermore, the *S. aureus* and *Cryptococcus neoformans* were succesful photo inactivated with nanoemulsion of chloroaluminium Pc (Zafar *et al.*, 2016).

Kalhotka *et al* worked to find out the effects of different charged Pcs on gram-positive and gram-negative bacteria. They found out that negatively charged and neutal Pcs were only effective against gram-positive strains of bacteria. The gram-negative bacteria were found be susceptible when subjected to cationic Pc (Kalhotka *et al.*, 2012; Friedrich *et al.*, 2000; Ragàs *et al.*, 2013). The reason is because the walls of gram-negative bacteria are made of negatively charged cell wall and therefore allow cation to pass through the cell membrane (Vallemolinales *et al.*, 2015). Phthalocyanine synthesized with aluminum cation was found to have a antiviral action towards vesicular stomatitis and herpes simplex virus type 1 as compared to the equivalent anionic nanoemulsion (Zafar *et al.*, 2016).

Photosensitizers with more than one cationic charge have been found to be active in the photodynamic inactivation of both gram-negative and gram-positive strains of bacteria (Ince *et al.*, 2019). The increase in cationic charge directs the Pcs toward weakening cell metabolism of the microbes (Ragàs *et al.*, 2013). Mantareva, (2010) used different numbers of cationic charges in their synthesized Pcs which resulted to varying degree of microbial deactivation.

Tetra-N-methylpyridyloxy Pcs with cationic charge II, III and IV was found to have a higher singlet oxygen and fluorescence quantum yields as compared to monocationic (Mantareva, 2010). Zinc (II) and Silicon (IV) Pcs were found to have singlet oxygen yields of 0.41 and 0.68 respectively due to the number of cationic charges attached to them (Mantareva, 2010). With the high generation of singlet oxygen, *S. aureus* was found to be susceptible to these Pcs. The high singlet oxygen generated through type II kind of reaction proved to be phototoxic to microbes (Mantareva, 2010). The distribution of charge in a photosensitizer influences its activities against microbial.

Work done by Cells *et al.*, (2011) revealed an increase of amphiphilicity property when di-cationic Pcs had their charge occur at adjacent meso-phenyl position making them to have a polarized charge distribution. This in turn accounts to the photo sensitizers' high intake by the microbial cell (Cells *et al.*, 2011). Cationic charges at adjacent position of a Pc increases its infiltration into the cell membrane of a bacteria as compared to di-cationic Pc with charge in the opposite position of a Pc (Cells *et al.*, 2011). The penetration may be attributed to upsurge affinity to the lipids by such Pcs. Simões and the

group also demonstrated dicationic porphyrins photosensitizer with trimethyl ammonia having the positive charges being at adjacent position increased its activeness against *E. coli* when compared to the same positive charges being at the opposite sides of the macrocyclic ring (Simões *et al.*, 2016).

The high efficient antimicrobial properties of the cationic charges being in adjacent position in a pc is because of electrostatic repulsion that occurs between the nearby charged particles (Liu *et al.*, 2015). The number of cationic charges and their distribution in a Pc determines its amphiphilic character, which is a significant property in synthesis of antimicrobial.

The amphiphilic property plays a big role in fine tuning a Pc to be used as an antimicrobial (Revuelta-maza *et al.*, 2019). This amphiphilic character may be increased *via* distribution and increasing number of cationic charges on the surface of a Pc (Ragàs *et al.*, 2013). The cationic substituted group attached to the Pc is of significance in aiming at the intracellular and cellular constituent of bacterial cell like mitochondria where activities take place. The axial center where a metal can attach to Pc is also a significant factor in increasing the antimicrobial property of Pc (Nwahara *et al.*, 2017).

Attached metal at axial position of a Pc helps to increase the lifetime of the triplet oxygen and quantum yield which results to generation of singlet oxygen that destroy pathogenic microbes (Friedrich *et al.*, 2000; Manieri *et al.*, 2015). Vallemolinales *et al.* (2015) had their Pc activities against microbes increased when they synthesised Pc with attached metal at axial position (Vallemolinales *et al.*, 2015). Enhanced antimicrobial activities

were observed with Pcs attached to diamagnetic metals such as zinc compared to their paramagnetic counterparts such as iron and vanadium. A high zone of inhibition percentage (100 %) on *E. coli* strain was observed using Pc linked to zinc (Table 2.2) (Vallemolinarés *et al.*, 2015). This was because of produced singlet oxygen that are toxic to microbial cells wall membrane and also the reactive radicles generated due to type I chemical reaction (Cieplik *et al.*, 2014).

Table 2.2: Antibacterial effect of Pc derivatives on different microbes

Pc	Concentration	Target microbes	Efficacy reduction	Inhibition zone % reduction	Ref
Zinctetra(4-carboxyphenyl) Pc	39.50 µg/mL	<i>E. coli</i>		100.00 %	1
	22.02 µg/mL	<i>Enterococcus faecalis</i>		32.91 %	1
	10.43 µg/mL	<i>K. pneumonia</i>		100.00 %	1
	22.48 µg/mL	<i>P. aeruginosa</i>		12.25 %	1
	16.03 µg/mL	<i>S. aureus</i>		72.22 %	1
Cobalt 2,9,16,23-tetra-phenylimino Pc	500.00 ppm	<i>Xanthomonas campestris</i>		16.00 mm	2
		<i>Xanthomonas citri</i>		17.00 mm	
	500.00 ppm	<i>X. compstris</i>		19.00 mm	2
Nickel 2,9,16,23-tetra-phenylimino Pc	500.00 ppm	<i>X. citri</i>		19.00 mm	
		<i>X. compstris</i>		18.00 mm	2
Zinc 2,9,16,23-tetra-phenylimino Pc	500.00 ppm	<i>X. compstris</i>		18.00 mm	2
Zinc Pc (neutral)	2.00 mM	<i>X. citri</i>		19.00 mm	2
Tetra zinc (II) Pc	2.00 mM	<i>Aeromonas hydrophila</i>	< 0.5 log	-	3
Cationic zinc (II) Pc	64.00 µg/mL	<i>S. aureus</i>	5-6 logs	-	3
substituted with triamino	13.00 µM	<i>S. aureus</i>	4 logs	-	3
Neutral uncharged zinc (II) pyridyloxy Pc	10.00 µM	<i>E. coli</i>	0.5 logs	-	3
Chromium (III) Pc chloride complex	37.03 µg/mL	<i>E. coli</i>		12.00 mm	4
	37.03 µg/mL	<i>P. aeruginosa</i>		9.00 mm	4
	37.03 µg/mL	<i>S. aureus</i>		10.00 mm	4

	37.03 µg/mL	<i>Bacillus cereus</i>		11.00 mm	4
2,9,16,23-tetra-N-[4-(5-phenyl-1,3,4-oxadiazol-2-yl)phenyl]benzamido-nickel Pc	40.00 µg/mL	<i>S. aureus</i>		23.00 mm	5
		<i>P. aeruginosa</i>		27.00 mm	
		<i>K. pneumonia</i>		28.00 mm	
2,9,16,23-tetra-N-[4-(5-phenyl-1,3,4-oxadiazol-2-yl)phenyl]benzamido-cobalt Pc	40.00 µg/mL	<i>S. aureus</i>		26.00 mm	5
		<i>P. aeruginosa</i>		27.00 mm	
		<i>K. pneumonia</i>		28.00 mm	
Zinc Pc with sulphamidic substituents	50 mg/100 ml	<i>P. aeruginosa</i>	6log	-	6
		<i>E. coli</i>	4log		
		<i>E. faecalis</i>	< 0.5log		
Tris{ 11,19,27-(1,2-diethylaminoethylthiol)-2-(captopril) Pc Zn	20.00 µM	<i>E. coli</i>		90.00 %	7
Tris{ 11,19,27-(1,2-diethylaminoethylthiol)-2-(captopril) Pc Zn conjugated to silver nanoparticles	20.00 µM	<i>E. coli</i>		95.00 %	

(Vallemolinarie *et al.*, 2015¹; Khan, *et al.*, 2018²; Abrahamse and Hamblin, 2016b³; Suriati, *et al.*, 2014⁴; Mantareva, 2010⁵; Berad *et al.*, 2012⁶; Ragàs *et al.*, 2013⁷)

Work done by Kalhotka *et al.* (2012) indicated that bacteria's becomes more susceptible when the Pc is tuned by attaching a substituent group at peripheral position of Pc macrocyclic ring. This helps in enhancement of its photophysical and of photochemical parameters such as intersystem crossing and increased generation of singlet oxygen.

Khan *et al.* 2018 synthesised Pc 2,9,16,23-tetra-hydroxyphenylimino synthesized that revealed a maximum zone of inhibition against *Aspergillus niger*. They attributed its sensitivity to cytoplasmic membrane and nuclei damage by the Pc (Khan *et al.*, 2015; Paschoal and Duarte, 2017). Tetracarboxi Pc synthesized by Vallemolinarie *et al.* (2015) had zones of inhibition of > 80 % when tested against drug resistant *E. coli*, *S. aureus* and *K. pneumoniae*, (Table 2.2). The activeness of this Pc against the strains of bacteria tested

is because of the substituents group carboxyl attached to the Pc macrocyclic structure that caused adhesion of the Pc to the surface of the bacteria. The sensitivity of the Pc against these strains of bacteria was also due to the carbonyl functional group increasing Pc wavelength towards the red region. This in turn stimulate generation of reactive singlet oxygen (Vallemolinarés *et al.*, 2015).

The synthesized 2,9,16,23-tetra-phenylimino Pc by Khan *et al.* (2018) had high zone of inhibition against strains of *X. compstris* and fungi *A. niger*. The imino functional group substituted to the Pc makes it to be more potent against microbes. This is due to imino functional group increasing chemical properties and thermal stability of Pc. It improves the Pc to absorb light into near infrared for effective generation of singlet oxygen and reactive oxygen species (Khan *et al.*, 2018.). Metal nanoparticles also play a major role in improving photophysical properties of Pcs to be used as antimicrobials.

The specificity, photophysical and photochemical properties of Pc such as singlet oxygen quantum yield can be increased by coupling it with metal nanoparticles such as Zn, Ag, Fe, Co, and others (Staicu *et al.*, 2013). Rapulenyane (2013) indicated an enhanced Pc with an increased singlet oxygen quantum yield with a value of 0.26 to 0.57 after coupling AgNps to ZnPc (Table 2.1). Conjugation of metal nanoparticle to Pc improves the photochemical and photo physical properties such as reducing the aggregation, increasing permeability and retention effect (Zafar *et al.*, 2016).

2.2 Metal nanoparticles

2.2.1 Synthesis of metal nanoparticles

Nanotechnology involves the synthesis, characterization, investigation and application of nanosized (1-100 nm) substances for the progress of science (Lu *et al.*, 2013). Nanotechnology has proved potential to develop new materials and provide positive solution to increased world's problems related to water, nutrition, health, energy and agriculture (Hassan *et al.*, 2018). Metallic nanoparticles have different chemical and physical properties from bulk metals such as lower melting points, mechanical strengths, specific magnetizations, optical properties and higher surface areas. These improved properties of metal nanoparticles might demonstrate attractive use in generation of various industrial products (Khan *et al.*, 2017). The key properties of such metal nanoparticles are determined by composition, shape, size, crystallinity and morphology (Lu *et al.*, 2013).

Various approaches have been documented for the synthesis of metal nanoparticles such as physical, chemical and biological methods. These methods can be classified into two broad approach; bottom-up and top-down (Figure 2.12) (Soni *et al.*, 2018).

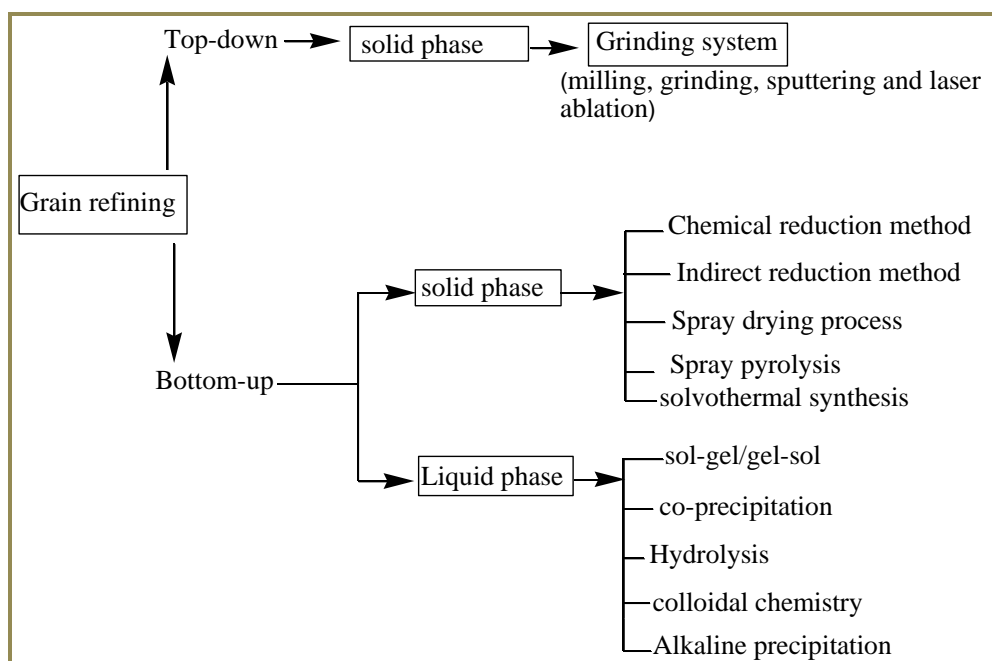


Figure 2.12: Various approaches for synthesis of metal nanoparticles

The Top-down technique involves breaking up of a bulk solid substance into small particles by size reduction. This is done by grinding system methods. The methods include techniques such as grinding, sputtering milling and laser ablation (Soni *et al.*, 2018). In bottom-up, technique the particles are formed by use of biological or chemical ways by atoms joining to form nuclei which forms into a particle of nano scale. Bottom-up method is classified into liquid and gaseous phase. Gaseous phase includes chemical vapor deposition that is caused by a chemical reaction. The physical vapor deposition on the other hand involves use of cooling of the evaporated material. Bottom-up technique may in the process be either nontoxic or toxic. For toxic processes it is classified into sol-gel process, chemical precipitation, spray pyrolysis, laser pyrolysis, vapor deposition and aerosol pyrolysis (Soni *et al.*, 2018). Nanoparticles have found use in manufacturing industries, agriculture, food technology, medicine electronic and environment.

2.2.2 Applications of metal nanoparticles

When materials are transformed from bulk materials to form nanoparticles, they also get transformed significantly their chemical and physical properties. Percentage of surface of nanoparticles compared to that of bulk molecule is high and this in turn increases the activities of the metal particle in nano form. This makes metal nanoparticles to be used in various fields such as catalysis (Ombaka *et al.*, 2015), biosensors, biomedicine, magnetic resonance imaging (MRI) (Khan *et al.*, 2017), Water treatment, painting, fuel cell, electronics, cosmetics and as antimicrobials (Figure 2.12) (Hoet *et al.*, 2004)

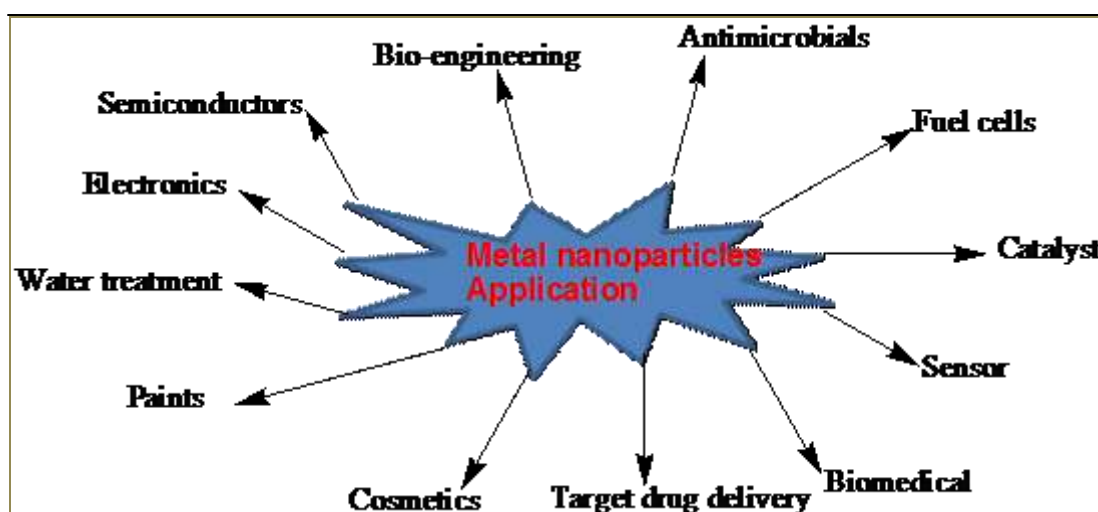


Figure 2.12: Application of metal nanoparticles

Literature has documented use of metal nanoparticles as catalyst for various kinds of chemical reactions (Ombaka *et al.*, 2015). The metal nanoparticles have catalytic sites located on their surfaces. Small nanoparticles ranging between 1-10 nm have effectively been used as catalysts. Decreasing particle size helps increase the ratio of surface atoms improving its catalytic properties.

The advantages of metal nanoparticle as catalysts are that, nanoparticles dispersed in solutions have potential to be used as photo catalysts since they are transparent to light. Secondly, metallic nanoparticles dispersed in solution helps lower the temperature below the boiling point of the solvent. Last but not least the preparation of nanoparticles shape and size and can be controlled easily. The Pd, Ni, Pt, and Ag, have found application in catalysts in certain chemical reactions in industries and laboratories. However, for certain metal like Au, the dissociative adsorption of oxygen or hydrogen molecules prevents reaction to be done on their smooth surfaces and at a temperature below 200 °C. This therefore, makes such metal to be inactive as a catalyst due to oxidation and hydrogenation reactions. Their catalytic properties may only be initiated by synthesizing their nanoparticles.

Nanoparticles are also being used in painting/Coatings industry. This has developed to be an important area for protecting existing infrastructure from corrosion and erosion, improving surfaces such as smart coating and improving the performance of equipment. The functionality of metal nanoparticles depends on their optical properties which are strongly enhanced by size and shape of particle. For example, Au appears yellow when reflected with light, while Au nanoparticles appear blue in presence of light. As the particle size decreases further a characteristic change of color is observed from blue to orange, steadily to purple and finally to red (Sadiku *et al.*, 2018).

Metal nanoparticles are becoming more useful in human medical application such as in drug delivery and imaging organs. Nanoparticles are currently used to transport drugs to the targeted organs and tissues where they are absorbed by cells. Distribution of drugs into various cell, tissue, or even organelle may be improved or controlled by being enclosed in colloidal nano sized materials (Khan *et al.*, 2017). Another area being studied extensively in medicine is use of nanoparticle to deliver drug into target cells or organs. In current use is in drug delivery is polymer–drug conjugates. The small-molecule drug delivery agents, for example anticancer chemotherapeutic compounds, have two properties that make them not to be effective: non-site-specific targeting and short circulation half-life, which leads to frequent administrations. These factors cause systemic side effects in the body. The coupling of drugs molecules to polymeric nanoparticles carries can eliminate the adverse side effects (Zhang, *et al.*, 2007)

Among the many uses, nanoparticles have shown potential to be used as antimicrobials. Nanoparticles may be chiefly beneficial in combating microbial infections (Wang and Shao, 2017). Such areas where nanoparticles are being used is antibacterial coatings of surfaces, promote wound healing, for medicinal materials, implantable devices, in antibiotic delivery systems to treat disease, in antibacterial vaccines to control bacterial infections and in bacterial detection systems to generate microbial diagnostics. The antimicrobial mechanisms of nanoparticles is not well understood, the currently mechanisms explained involves metal ion release, oxidative and non-oxidative stress mechanisms (Wang and Shao, 2017). Currently, the AgNp and ZnO-Np are thoroughly being explored and extensively investigated as potential antimicrobials.

2.2.3 AgNps and their antibacterial activity

Studies done in the past have shown that AgNps exhibit excellent combination of properties such as high electrical double layer capacitance, well-developed surfaces, catalytic activity and unique optical properties associated with the surface plasmon resonance. All these properties help in development of new-generation optical, antiseptics, in the field of photography catalysis (Khan *et al.*, 2017), electronic and sensor devices (Wöhrle *et al.*, 2012). AgNp is widely used in catalytic conversion of methanol to formaldehyde and ethylene to ethylene oxide by oxidation. Colloidal AgNp is of particular interest because of its distinct antibacterial activity (Baptista *et al.*, 2018).

The alteration of energy level by changing from continuous band to discrete band of AgNps in correspondence with nano-size particles results to size dependent physical and chemical properties. The AgNp have shown low toxicity to human cells with high toxicity to microbial cells making it useful for antimicrobial application (Wöhrle *et al.*, 2012).

The optical properties of AgNps are determined by size, shape, composition, environment and structure of adsorption materials. The main feature of an absorption spectrum of AgNps with particle size above 2 nm is the presence of a strong band in the visible range. This band is referred to as surface plasmon resonance, it occurs when light falls on the surface of AgNps releasing conduction electrons. Surface plasmon for spherical AgNps with particle size between 2-100 nm, their absorption band appears at around 400 nm. Silver nanoparticles produces highest plasmon resonance band as compared to other metal nanoparticles (Wöhrle *et al.*, 2012).

The mechanism of how AgNps works on bacteria has been explained by various scientific reports. The solution of AgNps contain Ag^+ ions that are bactericidal when it comes in contact with bacteria metabolism destroying it (Li *et al.*, 2010). The Ag^+ ions have high affinity towards sulphur and phosphorous, The Ag^+ ions get attached to these atoms that make up proteins molecule of the bacteria causing destruction to the cell membrane. AgNps with diameter < 10 nm can infiltrate the proteins of bacteria and attach to sulphur and phosphorous leading to penetrability of the cell membrane by foreign substance. This in long run leads to death of bacteria. Most studies show that AgNp act by physically interacting with bacterial cell surfaces (Baptista *et al.*, 2018). This property is propelled by the shape, size and concentration of the AgNps (De Matteis *et al.*, 2008; Iravani *et al.*, 2014). AgNp of dimension < 30 nm have been found more active against *K. pneumonia* as they are able to infiltrate through the cell wall of the microbes (Baptista *et al.*, 2018). AgNp have been synthesized using various approaches which can be categorized into two namely chemical and physical techniques. The Chemical process involves use of hydrazine, and sodium borohydride (Preetha *et al.*, 2013). While the physical process includes condensation, laser ablation and evaporation (Noroozi *et al.*, 2012)

2.2.4 ZnO-Np and their antibacterial activity

Most studies have been done on Zinc oxide (ZnO) for its potential of ultra violet absorbance, luminescence at high temperatures, wide chemistry and piezoelectricity (Hassan *et al.*, 2018). ZnO has found use in electronics, plastic, paints, cosmetics, pharmaceuticals and rubber manufacturing (Ashe, 2011). The obstacle for these

applications is that for bulk ZnO properties are mostly not stable and therefore, cannot be developed to meet modern necessities. ZnO–Np rooted on the surfaces of polymer for example starch enhances its functional properties making it to have prospective uses such as UV-protection ability in sunscreens, textiles and as antimicrobials. Studies done by Hassan *et al.* (2018) indicated the excellent antimicrobial properties of ZnO-Np impregnated onto cotton fabrics against, *K. pneumoniae* and *S. aureus* (Hassan *et al.*, 2018).

Although the exact antimicrobial mechanisms of how ZnO-Nps works to cause bacterial death is not yet well understood, scientific works reports on toxic action of reactive oxygen species. These reactive oxygen species are produced on the surface of the nanoparticles causing antibacterial effect. Zinc ion released infiltrate in cell membrane of bacteria interfering with bacteria metabolism and membrane dysfunction leading to cell death (Hassan *et al.*, 2018). The work done by Hassan *et al.* (2018) revealed ZnO-Nps had potent properties in fighting both positive and gram-negative bacteria. It had high zone of inhibitions against *S. aureus* and *K. pneumoniae*. Its effectiveness against bacteria depended on concentration and size of ZnO-Nps while the particle shape and crystallinity showed no correlation (Hassan *et al.*, 2018).

ZnO-Nps have been synthesized following various approaches such as precipitation, spray pyrolysis, sol-gel synthesis, thermal decomposition, micro-wave irradiation, chemical vapor method, vapor condensation method and laser synthesis techniques

(Aneesh *et al.*, 2007). The surfaces of AgNps and ZnO-Nps can be easily functionalized in order to conjugate them with Pcs.

2.3 Conjugation of Pcs to metal nanoparticles

The conjugation of nanoparticles (gold, zinc oxide, silver and others) to Pcs is currently being investigated to determine their effectiveness as antibacterial. Their photochemical activity when irradiated with UV-Vis increases when conjugated with Pcs. Their quantum size effect, electrodynamic interactions and surface-to-volume ratio due to their small size allows application of nanoparticles to the field of antimicrobials (Mondal and Bera, 2014). Metal nanoparticles have been conjugated with different compounds such as antibodies, photosensitizers, amino acids and bio-polymers (Hoet *et al.*, 2004).

Rapulenyane 2013 explored the effectiveness of conjugating Pcs to enhance their biocidal activities. The work entailed coupling AgNps with Pcs with the aim of increasing its photosensitizing abilities. The conjugation of metalloPc to AgNps led to an enhanced photochemical and photophysical activities (singlet oxygen, triplet state and fluorescence quantum yields) of the Pcs. This led to improved antimicrobial properties when the Pcs were irradiated with light of certain wavelength. The coupling of this Pc and AgNps led to improved light toxicity at 5–10 mM, with potent antimicrobial sensitivity against *E. coli* in the presence of light. The synthesized metal nanoparticles are examined using various spectroscopic and microscopic techniques: UV-Vis spectroscopy, SEM, TEM, energy dispersive spectroscopy (EDS), atomic force microscopy (AFM), dynamic light scattering (DLS), powder XRD, FTIR, and Raman spectroscopy.

2.4 Characterization of Pcs compounds and metal nanoparticles

The choice of characterization methods for compound or element is subject to the properties of the compound being investigated. Different methods are used to analyze the morphology, structure, size, chemical and physical properties, optical properties and elemental composition.

2.4.1 Scanning electron microscopy (SEM)

The SEM instrument is used for observation of sample surfaces. It was first invented by Knoll in the 1930s and thereafter a new model was developed by Jeol in Japan (Akhtar *et al.*, 2019). It involves scanning of the surface of material using a focused beam with highly energetic electrons that generate secondary electrons from the sample surface (Seyforth, 2015). Topography of the surface which includes texture, crystalline structure, and chemical composition can be observed from the image obtained from detected secondary electrons (Akhtar *et al.*, 2019). Figure 2.13 shows the basic schematic construction of SEM instruments and an image of ZnO-Np (right) reported by Midatharahalli *et al.*, 2019.

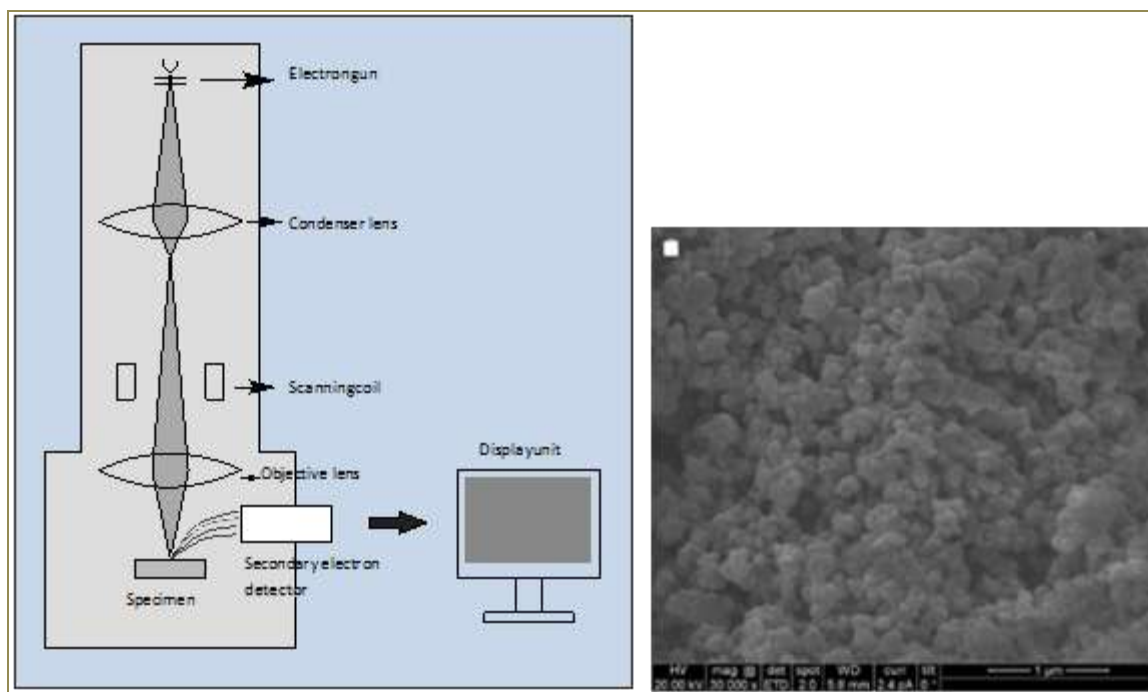


Figure 2.13: Basic schematic construction of SEM (left) and SEM images of ZnO-Np reported by Midatharahalli *et al.*, 2019 (right)

The working principle of SEM begins by the gun emitting the electron beam enclosed in a vacuum. The beam follows a vertical path between electromagnetic fields and through the lenses. Electron beam is directed to the sample by objective lens. The beam scans the targeted surface area of the sample by sweeping across with the help of deflector coils. The coil is controlled using scan generator.

2.4.2 Transmission electron microscopy (TEM)

A TEM is an imaging technique that uses an accelerated beam of electrons transmitted through a sample, an image is formed, magnified and displayed on a fluorescent screen or layer of photographic film (Shieh, and Qiao, 2006). The technique was invented by German scientists Ernst Ruska and Max Knoll in 1931 (Lambert and Mulvey, 1996).

Since then it has developed to become an important tool in the field of science study the surface of micro and nanoparticles (Shieh, and Qiao, 2006). The application of TEM in nanoparticles is to study the morphology and distribution of particle size of the materials being analyzed. Though, TEM requires very thin sample that electrons are able to penetrate through, it takes a longer time to prepare the sample. In a TEM, an electron gun, fires a beam of fast moving electrons (Akhtar *et al.*, 2019). High voltages and electromagnetic coils are used to accelerate the electrons to high speeds. The high accelerating voltage makes it possible to achieve far greater resolved images compared to SEM. Figure 2.13 shows various components of a TEM instrument and a sample micrograph of AgNp produced by the instrument.

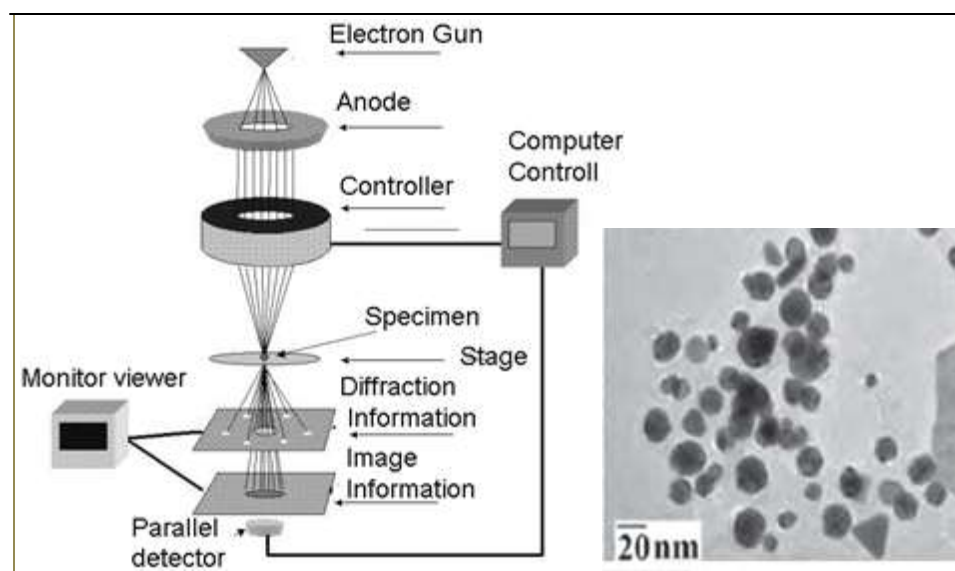


Figure 2.13: Diagram of a TEM instrument (left) and TEM micrograph of AgNp reported by Santra *et al.* (2015) (right)

The electron beams generated are converged by a condenser lens into a thin beam of required electrons. The condenser lens is made up of an aperture that eliminates high angle electrons. When these electron has enough acceleration, they move through the

ultra-thin specimen and reflection beam are conveyed subject to how transparent the material is to electrons (Akhtar *et al.*, 2019). The micrograph generated by the TEM, is reflected onto a screen that is phosphorescent.

2.4.3 Powder XRD

The use of X-rays was first discovered by Roentgen in 1895 (Tubiana, 1996). The technique was later developed over the years and in 1947 Phillips introduced the first commercial powder diffractometer (Etter and Dinnebier, 2014). Powder XRD belongs to the family of X-ray crystallography and although it is an established technique for bulk materials, it has now become a routine tool to nondestructively characterize nanostructures as well. It helps to interrogate the crystal orientations, preferred phases, average grain size and crystal defects among others (Bunaciu *et al.*, 2015). Diffraction occurs when a wave interferes with monochromatic beam of X-rays leading to constructive interference or by cancelling each other leading to destructive interference. An X-ray from a copper cathode ray tube passes through a nickel filter. The filter allows monochromatic radiation to pass through. It is then passed onto the sample in the sample holder. The detectors detect diffraction beams from the sample (Figure 2.13) (Bunaciu *et al.*, 2015).

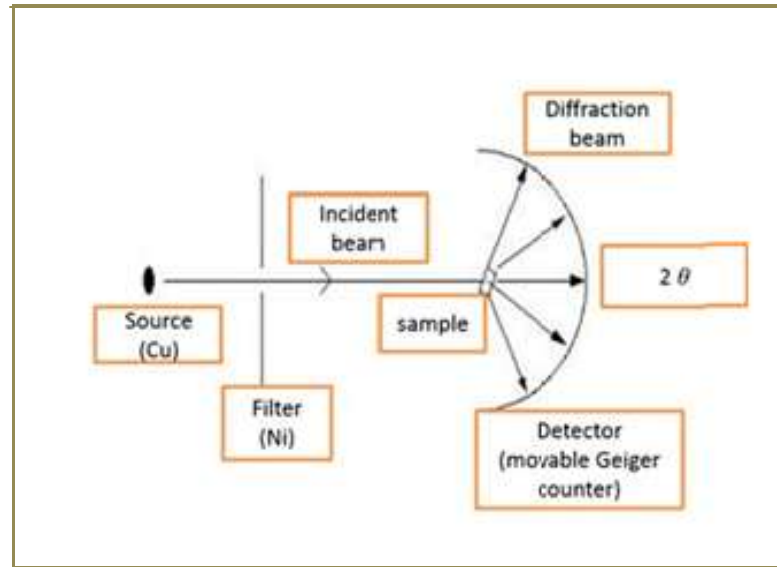


Figure 2.13: Schematic diagram of the powder XRD components

The X-ray wavelengths generated are of the order of inter planer spacing in a sample material. This information is obtained using Bragg's diffraction **Equation 2.3**,

$$n\lambda = 2d\sin\theta \quad \text{.....Equation 2.3}$$

Where λ is the wavelength of X-rays, d is the inter planer distance, n is the order of diffraction and θ is the angle of diffraction.

X-ray spectral pattern is of importance in determining crystal size in a powder sample. The lines in a diffraction pattern are of finite breadth, but for small particle sizes there is an increased broadening due to decreasing particle size. The reason for broadening is because of incomplete destructive interference. The XRD pattern of a sample obtained confirmed by comparing it with diffraction pattern of known standard files stored in the software of the instrument that is Joint Committee on Powder Diffraction Standards (JCPDS) or the International Centre for Diffraction Data (ICDD) (Bunaciu *et al.*, 2015).

2.4.4 Fourier-transform infrared spectroscopy (FTIR)

The genesis of FTIR can be traced back as early as 1880 when Albert Michelson invented interferometer (Svedberg, 2004). The FTIR instrument helps to obtain infrared spectrum generated by emission or absorption of a gas, liquid or solid. The infrared region lies between the visible and microwave regions (700 nm to 0.1 cm) in the electromagnetic spectrum. The infrared spectrum has three regions, that is near-IR spectrum (4000-13000 cm^{-1}), mid-IR spectrum (400-4000 cm^{-1}) and far-IR spectrum ($< 400 \text{ cm}^{-1}$). The mid infrared is mostly used due to the presence of characteristic vibrational modes (Nandiyanto *et al.*, 2019). The spectrum reads percent transmittance or absorbance in the vertical axis as a function of wave number (cm^{-1}) in horizontal axis. It helps identify functional groups in the Pcs and absence or presence of functional groups in metal nanoparticles (Nandiyanto *et al.*, 2019). The instrument is made up of an interferometer, an IR source, a detector, an analytical cell, and a computer for running the instrument and processing of data (Figure 2.14) (Svedberg, 2004).

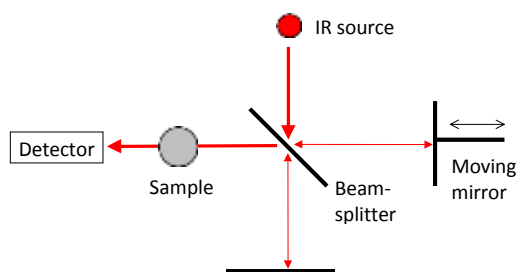


Figure 2.14: Schematic diagram of the FTIR components

The technique of FTIR involves, light source generates infra-red light that that is transmitted to interferometer *via* the optical path. Interferometer is made of a fixed mirror, beam splitter and the moving mirror. The beam splitter separates the beam of light into two which gets reflected by moving mirror and fixed mirror. It is then converged

together by the beam splitter. The strength of the interference of light is recorded in an interferogram and the x-axis is recorded optical path difference (Svedberg, 2004). The interference pattern, detected by the infrared detector as variations in the infrared energy level, is what yields spectral information.

The FTIR spectra of metallo-Pc and metal-free Pc both show strong absorptions associated with C-H bending in the wavelength range of $750\text{-}800\text{ cm}^{-1}$. Absorption of C-C bond stretching is between $1450\text{-}1600\text{ cm}^{-1}$, while the absorptions of C-H bond stretching are evidenced between $3000\text{-}3050\text{ cm}^{-1}$ (Tayfuroğlu *et al.*, 2018). Difference between metal-free Pc and metallo-Pc is strong absorption evidenced at 3289 cm^{-1} associated with N-H bond stretching in metal-free Pc (Ziminov *et al.*, 2006); Gorduk *et al.*, 2017). For both metal-free and metallo-Pc, C-H stretching bond appears between $3000\text{-}3050\text{ cm}^{-1}$ (Ziminov *et al.*, 2006).

2.4.5 UV-Vis spectroscopy

UV-Vis spectroscopy is an instrumental method that helps record absorption spectra of a sample using ultraviolet (UV) and visible (Vis) of the spectrophotometer (Moeur *et al.*, 2006). Analyzing of solids, liquids and gases is made possible by use of radiant energy that occurs in the visible, near and far ultraviolet and near infrared regions of the electromagnetic spectrum.

In the electromagnetic spectrum, near infrared is between $765\text{ to }3200\text{ nm}$, for Vis is between $400\text{ to }765\text{ nm}$ and for UV is $300\text{ to }400\text{ nm}$ (Moeur *et al.*, 2006). The

instrument UV-Vis is made up of light source from a tungsten filament, compartment for holding sample, detector system, signal processor for interpreting the data and readout system (Figure 2.15) (De Caro, 2015).

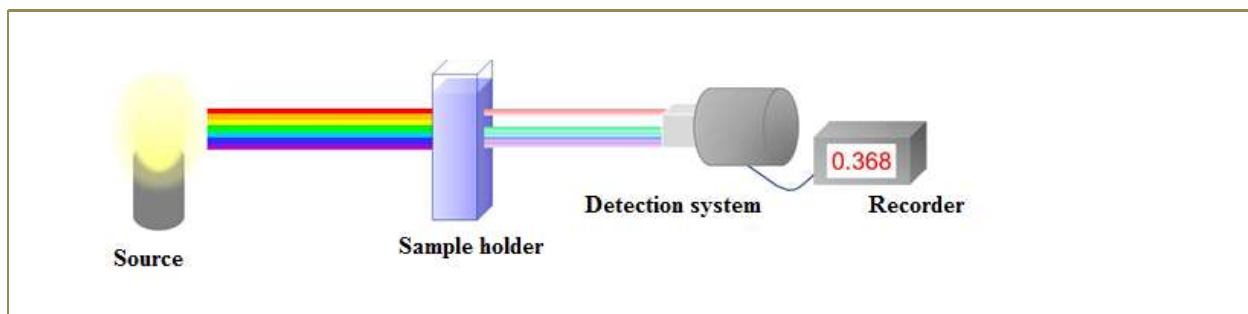


Figure 2.15: Basic components of UV-Vis

The working of a UV-Vis involves a beam of light from light source passing through a sample solution placed in a cuvette. The sample absorbs a given amount of light energy from the beam of light passing through it. The remaining amount light energy that has not been absorbed is then measured using a photo detector, the results gives the absorbance of the sample (De Caro, 2015). Information is represented inform of transmittance or absorbance(Moeur *et al*, 2006). The intensity is related to the concentration of the sample being analyzed.

2.4.6 Nuclear magnetic resonance (^1H NMR and ^{13}C NMR)

Edward Mills in 1946 first described NMR phenomena, as absorption of radio-frequency energy (4 to 900 MHz) due to energy transitions corresponding to different states of nuclear spins in a strong, constant applied magnetic field (Gerothanassis *et al*, 2002). In NMR it is the nuclei that are sensitive towards the surrounding electronic environment. Therefore, the nuclei will resonate at different frequencies depending on the local

electronic environment surrounding the atom. The nuclei consist of spin that are electrically charged. External magnetic field causes an energy transfer to take place from the base energy to a higher energy level.

Transmission of this energy happens at wavelengths comparable to radio frequencies. Therefore, when the spin returns to its ground level, it produces energy that corresponds to a given frequency. The frequency signal is measured in order to yield an NMR spectrum for the nucleus being investigated. Structural components and functional groups of organic compounds can be identified based on the observed spectrum (Gerothanassis *et al*, 2002). The NMR instrument consists of a number of components which includes sample holder, magnetic coils for inducing magnetic field when current flows through them, permanent magnet to provide homogeneous magnetic field at 60-100 MHz, radio frequency transmitter (RF) that produces a short powerful pulse of radio waves, radio frequency receiver (detector) that detects radio frequencies emitted as nuclei relax to a lower energy level and read out systems for analyzing and recording the data (Figure 2.16).

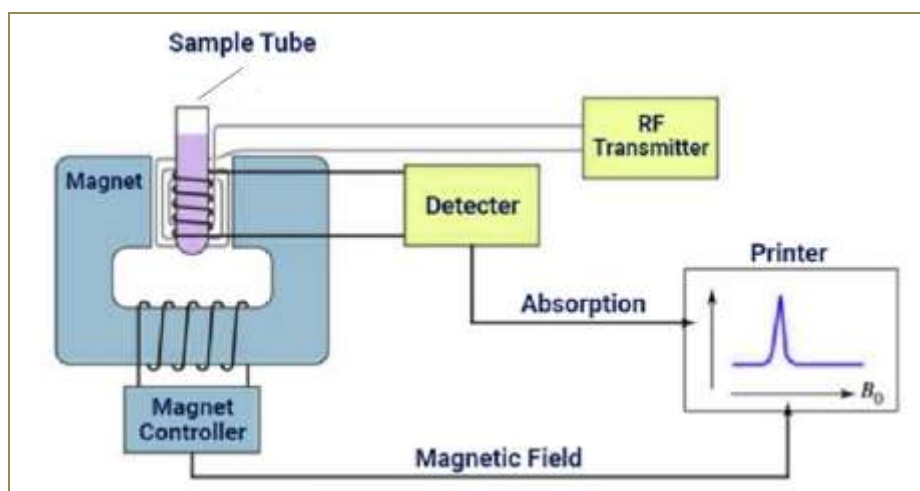


Figure 2.16: Basic components of NMR

Materials to be analyzed are introduced to an area with magnetic field through sample holder. A frequency signal is generated by excitation of the nuclei of a sample with radio waves into nuclear magnetic resonance. The signal is received by detector with sensitive radio receivers for interpretation. The information of a structure of a molecule is determined when the intramolecular magnetic field changes the resonance frequency. The frequency generated will give the information of electronic structure of a molecule and the functional groups of the molecule. Apart from identification, NMR provides information about the chemical environment of molecules (Gerothanassis *et al.*, 2002).

The ^{13}C NMR and ^1H NMR are the most common types of NMR used in spectroscopy. The proton (^1H) peaks and their areas help to give the number of protons that are responsible for these peaks. Chemical shifts of ^{13}C and ^1H nuclei are measured (in ppm) using Trimethylsilane (TMS) as reference. It ranges from 0 to about 250 ppm for ^{13}C and 0 to 12 for ^1H . As in proton spectra, the accurate chemical shift of a nucleus depends on the atom or atoms attached to it and there are correlations with the electronegativity of substituents.

The NMR spectra's of unsubstituted Pcs portrays similar signal intensities for protons in the non-peripheral and peripheral positions. Octa-substituted Pc is monoisomeric while tetra-substituted Pc shows various isomers. This makes NMR signals of tetrasubstituted Pc to be broad compared to that of octa-substituted Pc (Kim *et al.*, 2015). Depending on the substitution and its position, the signals of the magnetic fields are either shifted downfield or on up field. The NMR signals of electron-withdrawing substituents are

preferentially shifted up field while electron donor groups commonly result in a downfield shift (Sergeyev *et al.*, 2007).

2. 5 Antimicrobial susceptibility tests

2.5.1 Disk diffusion method

Susceptibility of microorganisms to certain antimicrobial compound can be determined using various techniques and disk diffusion is one of them. Disk diffusion was first developed in 1940 by Kirby and Bauer (Hudzicki, 2016). The method involves inoculating a sterile agar plate with known bacteria. Filter paper disk 6-mm in diameter containing a known amount compound to be tested against bacteria is placed on a Mueller-Hinton (MH) agar plate.

The antimicrobial compound is capable to infiltrate through the agar layer. Disk plates are then stored for incubation for 18-24 hours. Diffusion through the agar takes a longer time as compared to release of the antimicrobial compound out of the disk. This makes concentration of the test compound to be highest near the disk and reduction is experienced far away from the disk. The time of incubation the microorganism diffuse through the agar impregnated with the test compound. The test compound if it has antimicrobial properties it inhibits the growth of these microorganisms. The region where there is no growth of the microorganism is referred to as zone of inhibition, it is measured and compared to known standards (Figure 2.17) (Hudzicki, 2016)

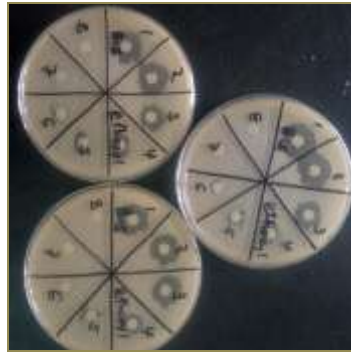


Figure 2.17: Disk diffusion method

2.5.2 Minimum inhibitory concentration (MIC)

The MIC determines the lowest concentration of a test compound that inhibit the growth of a bacteria after 24 hours of incubation (Owuama, 2017). MIC is obtained using disk plates with solid growth medium by Kirby-Bauer disk or through the use of broth dilution technique after a pure culture is isolated (Joray *et al.*, 2015; Owuama, 2017). *Via* broth dilution method the MIC can be determined by adding culture of bacteria to wells of liquid with decreasing concentrations of test compound. The MIC is the value between concentrations of the last well where there was no visible growth and the next lower dose that allowed bacterial to grow (Owuama, 2017).

2.5.3 Minimum bactericidal concentration (MBC)

The MBC helps to get the value of the lowest concentration in which the test compound is able to kill a particular bacteria (Owuama, 2017). MBC is obtained by carrying out broth dilution to MIC concentration. While the MIC test reveals the lowest level of a compound to be used as an antimicrobial to prevent growth of a bacteria, MBC shows the lowest concentration of the test compound that results to microbial death (Owuama, 2017).

2.6 Cytotoxicity test

The 3-(4,5-dimethylthiazol-2-yl)-2,5-diphenyltetrazolium bromide (MTT) calorimetric test is commonly applied technique for the evaluation of cell viability and cytotoxicity for substances to be used as drugs (Mosmann, 1983). The test method involves the reduction of MTT salt (yellow) as a result of cellular metabolic activities brought about by nicotinamide adenine dinucleotide phosphate (**NAD(P)H**) by oxidoreductase enzymes to form an insoluble (*E,Z*)-5-(4,5-dimethylthiazol-2-yl)-1,3-diphenylformazan purple in color (Bahuguna *et al.*, 2017).

Cells that are healthy reduce MTT salt to form formazan (Figure 2.18), cells that are inactive will fail to convert MTT to formazan. Cell viability in MTT test is carried out by analysis of formazan soluble in DMSO at a wavelength between 490 nm to 720 nm. The results is linearly associated with the enzyme activities and related to the number of viable cells (Nasr *et al.*, 2018). The high intensity of purple color indicates higher cell viability and the reduction in purple color intensity shows decreases in cell number due to cytotoxicity effects of the test compound (Bahuguna *et al.*, 2017).

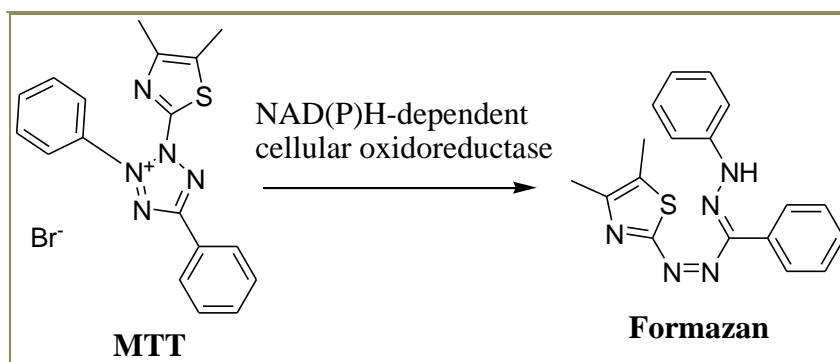


Figure 2.18: Conversion of MTT to formazan

CHAPTER THREE

MATERIALS AND METHODS

3.1 Introduction

This chapter presents the materials and chemicals used to synthesize ZnPc, AgNps, ZnO-Nps and Pcs conjugated to ZnO-Nps and AgNps. In addition, the techniques used to characterize the synthesized compounds and materials, conduct photochemical and antimicrobial analysis are outlined.

3.1.1 Reagents and chemicals

All solvents and reagents used were of analytical grade and were obtained from Merck chemicals (German). These included ammonium chloride 99%, ammonium molybdate 99%, copper (I) Iodide 99%, dichloro-bis(triphenylphosphine)-palladium(II) ($\text{PdCl}_2(\text{PPh}_3)_2$) 98%, dichloromethane 99%, dicyclohexylcarbodiimide 99%, diisopropylamine 99%, 1,3-diphenylisobenzofuran (DPBF) 99%, dimethylformamide 99%, ethanethiol 97%, ethyl acetate 99%, fuming sulphuric acid 30%, hexane 95%, iodine 99.99%, L-glutathione 98%, methanol 96%, 3-methoxypropyne 97%, MTT (3-(4,5-dimethylthiazolyl-2)-2,5-diphenyltetrazolium bromide), phthalimide 99%, potassium carbonate 99%, silica gel 60 Å (average pore diameter) 70-230 mesh, silver nitrate 99%, sodium borohydride 99%, sodium hydroxide pellets 98%, sodium thiosulphate 98%, starch (soluble GR for analysis 1.01252 Millipore), tetrahydrofuran 99% (THF), urea ACS reagent 99%, Whatman filter papers No-1, zinc acetate 99%, zinc chloride 99%, Zinc phthalocyanine dye content 97 % (ZnPc*) and, zinc nitrate tetrahydrate 99%.

3.1.2 Cleaning of glassware apparatus

Glassware were cleaned by first soaking them in nitric acid (2 M) overnight to remove stains, washed with distilled water using a detergent and rinsed three times with distilled water. They were then dried in an oven at 100 °C for a period of 2 hour and stored for subsequent use.

3.2 Instrumentation

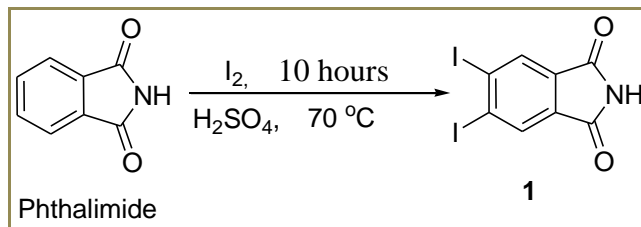
The UV-Vis absorption spectra were recorded on a Shimadzu 2550 spectrophotometer. Micrographs of SEM were obtained using a JEOL JSM 6100 (Institute de Ciencia material-Madrid Spain). The TEM micrographs obtained using JEOLTEM 1210 at an accelerating voltage of 100 KV (Institute de Ciencia material-Madrid Spain). FTIR spectra were acquired using a Shimadzu IRT racer-100 (Chemistry labs Kenyatta university), mass spectrum was measured using HR-MS Shimadzu QP-2010 plus mass spectrometer at 70 ev. X-ray diffraction patterns were registered on a D8 Advance diffractometer supplied by BRUKER AXS, Germany. Measurements were done using Cu K α radiation ($\lambda = 1.54060 \text{ \AA}$). The patterns were recorded in the 2θ range between 10 and 90° with increment of 0.028°. ^{13}C CP MAS-NMR spectra obtained using a Bruker Avance 400 spectrometer with an external magnetic field of 9.4 Tesla. ^1H NMR spectra recorded with Bruker AMX 400 MHz or a Bruker Avance II+ 600 MHz NMR spectrometer (Institute de Ciencia material-Madrid Spain). Microwave oven (Domestic model RM 240, output 800W and 2450 MHz) was used for heating purpose to take advantage of rapid synthesis and reduce use of solvent (Chemistry labs Kenyatta university). Photo-irradiations for singlet oxygen and bacterial inactivation studies were

carried out through the use of a general electric quartz line lamp (GE EXR 300 W 82 V). A 600 nm glass filter (Schott) was used to filter off infrared and ultraviolet radiations respectively. An interference filter (Intor, 670 nm with a band width of 40 nm) was also placed before the sample. Stirring was done on a Lab Smart MSH-Pro+ model hot plate (Chemistry labs Kenyatta university).

3.3 Synthesis of precursors and Pcs

3.3.1 Synthesis of 4,5-diiodophthalimide (1)

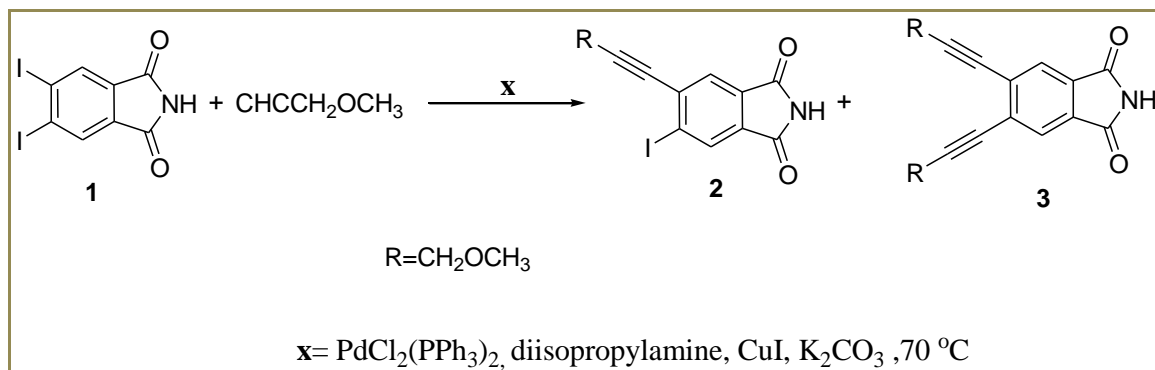
Synthesis of compound **1** was done following the method described by Yamamoto (2016) with some modifications. Briefly, the procedure involved adding 15 g (102 mM) of phthalimide to 100 ml of 30% fuming sulphuric acid followed by 25 g (198 mM) of iodine as shown in scheme 3.1. The resulting solution heated at 70 °C for 10 hours in a fume chamber. The formed compound was slowly poured into 500 g of ice and left to settle for 30 minutes. Precipitated solid was filtered using a glass frit funnel, and washed with 200 ml distilled water. The solid was then washed with 100 ml of 2 % potassium carbonate (K_2CO_3), 50 ml saturated solution of sodium thiosulphate ($Na_2S_2O_3$) and dried at 100 °C in oven for 3 hours. The Soxhlet extractor was used to extract the solid using 150 ml of acetone. The formed precipitate was a mixture of two compounds with bright yellow in color. The mixtures were isolated using column chromatography using ethyl acetate and chloroform in the ratio 1:4 as the eluent.



Scheme 3.1: Formation of 4,5-diiodophthalimide (1)

3.3.2 Synthesis of 4-iodo-5-(3-methoxy prop-1-ynl) phthalimide (2)

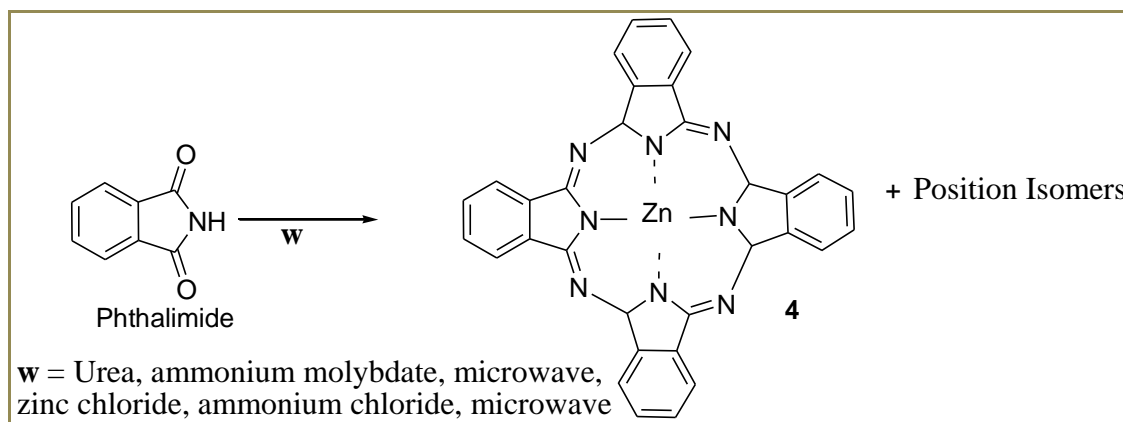
The method by İşci *et al.* (2014) was adopted to synthesis of compound **2** with some modifications. The steps employed included mixing 2 g of the prepared **1**, 0.18 g (0.25 mM) of dichloro-bis(triphenylphosphine)-palladium (II) ($\text{PdCl}_2(\text{PPh}_3)_2$), 1.2 g (0.02 mol) of 3-methoxypropyne, 20 ml of diisopropylamine and 0.03 g (0.16 mM) of copper (I) iodide in 50 ml two necked round bottom flasks as shown in scheme 3.2. This mixture was left to stir at 70 °C for two hours. The resultant was cooled to 25 °C by stirring using a glass rod followed by vacuum filtration and the residue washed with 20 ml of dichloromethane. The filtrate obtained was concentrated using rotary vapor at 38 °C to obtain a crude solution. This was then purified by using silica gel column chromatography with solvent mixture hexane: ethyl acetate as eluent in the ratio 3:1.



Scheme 3.2: Formation of 4-iodo-5-(3-methoxy prop-1-ynl) phthalimide (2)

3.3.3 Synthesis of zinc Pc (4)

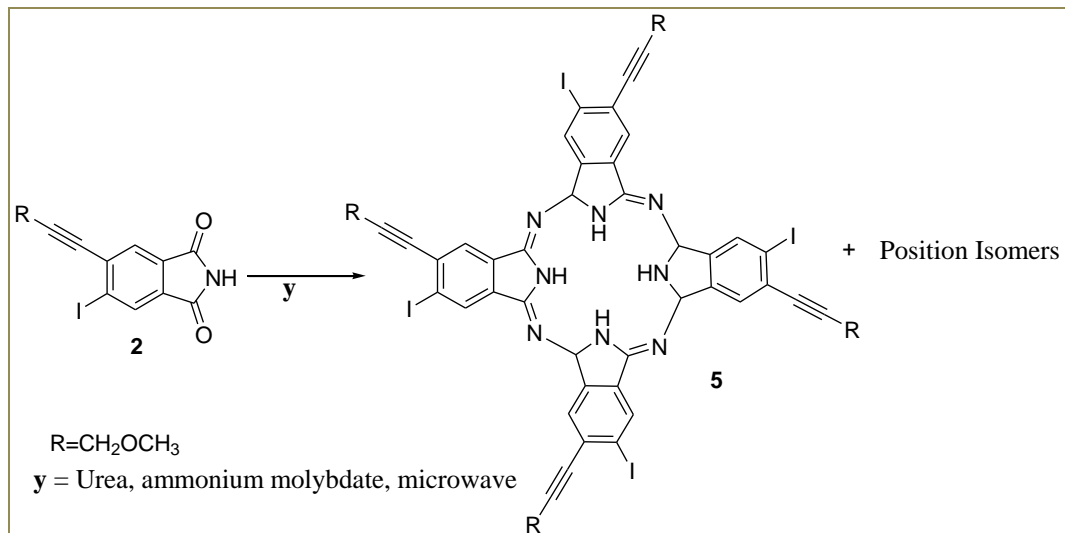
Compound **4** was synthesized following the protocol described by Shaabani, 1999 with modifications. The procedure involved grinding (clean pestle and mortar) into fine powder a mixture of 9 g of phthalimide, 18.0 g (299.70 mM) of urea, 3.0 g (56 mM) of ammonium chloride, 0.05 g (0.26 mM) of ammonium molybdate as catalyst and 1.0 g (7.35 mM) of zinc chloride (scheme 3.3). The resultant homogeneous mixture was transferred to a 250 ml beaker, covered with an evaporating dish and subjected to microwave oven heat at high power (800 W) for 4 minutes. After the 4 minutes, the power of the oven was turned to medium power for another 2 minutes. The product was washed with 300 ml hot H₂O (70-80 °C) and oven-dried at 70 °C for 4 hours. Crude **4** was subsequently purified two times by subsequent recrystallization by transferring it in 15 ml concentrated H₂SO₄ and pouring it in 250 ml of distilled water. Soxhlet extraction was used for purification using 150 ml acetone and then oven-dried at 50 °C for 6 hours.



Scheme 3.3: Formation of zinc Pc (4)

3.3.4 Synthesis of 2,9,16,23-tetraiodo-3,10,17,24-tetra(3-methoxyprop-1-nyl)Pc (5)

The protocol described by Yogesh *et al.* 2014 was used to synthesis compound **5** with some modifications. The steps employed included mixing 0.50 g of compound **2**, 1 g (16.65 mM) of urea and 0.09 g (0.46 mM) of ammonium molybdate as shown in scheme 3.4. The mixture was crushed thoroughly to form a homogeneous mixture using clean pestle and mortar and transferred to a 250 ml glass beaker then covered with an evaporating dish. The beaker and its contents were placed in a microwave oven and heated (high power-800 W) for 3 minutes and thereafter cooled to 25 °C by stirring using a glass rod. After cooling, the formed blue solid was transferred to a filter-funnel and washed 3 times with 50 ml of distilled water, 20 ml of 0.1 M NaOH and, then followed by rinsing with 20 ml 0.1 M HCl respectively. The insoluble impurities were removed by washing the Pc through silica gel column chromatography with tetrahydrofuran (THF). The obtained Pc from the column was dissolved in 40 ml of THF. The Pc was precipitated by the addition of 20 ml methanol and separated by centrifugation at 2000 rpm for 4 minutes

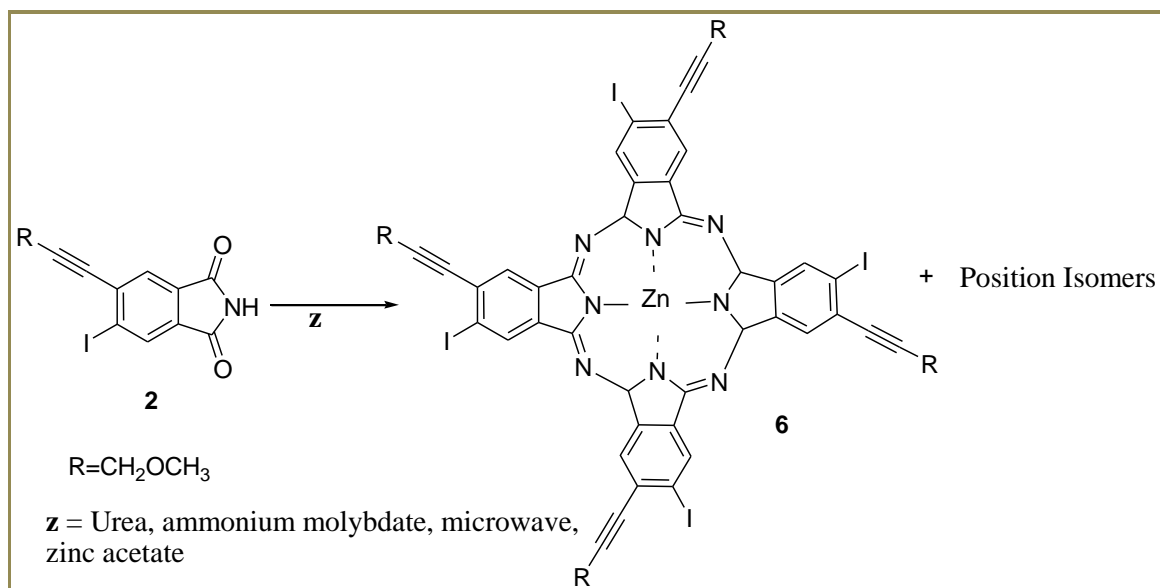


Scheme 3.4: Synthesis of 2,9,16,23-tetra iodo-3,10,17,24-tetra (3-methoxy prop-1-nyl) Pc (5)

3.3.5 Synthesis of 2,9,16,23-tetraiodo-3,10,17,24-tetra(3-methoxyprop-1-nyl) ZnPc (6)

The protocol described by Yogesh *et al.* (2014) was used to synthesis compound **6** with some modifications. The steps employed included mixing 0.50 g of compound **2**, 1.00 g (16.65 mM) of urea, 0.09 g (0.46 mM) of ammonium molybdate and 0.5 g (2.73 mM) of zinc acetate as shown in Scheme 3.5. The mixture was crushed thoroughly to form a homogeneous mixture in a mortar with a pestle, transferred to a 250 ml beaker then covered with an evaporating dish. The beaker and its contents were placed in a microwave oven and heated (high power-800 W) for 3 minutes at one-minute interval then left to cool to 25 °C for 20 minutes. After cooling, the formed blue solid was transferred to a filter-funnel washed with 50 ml of distilled water, 20 ml of 0.1 M NaOH and, then followed by rinsing with 20 ml 0.1 M HCl. The insoluble impurities were

removed by washing the Pc through silica gel column chromatography with tetrahydrofuran (THF). The obtained Pc from the column was dissolved in 40 ml of THF. The Pc was precipitated by the addition of 20 ml methanol and separated by centrifugation at 2000 rpm for 4 minutes

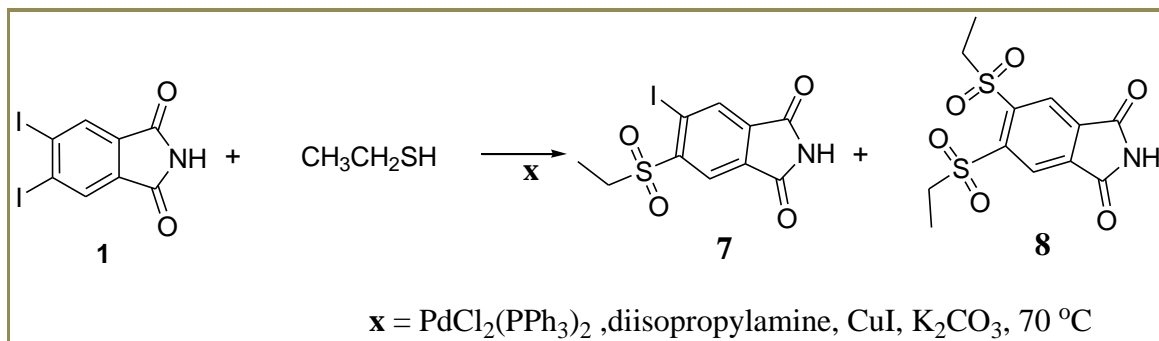


Scheme 3.5: Synthesis of 2,9,16,23-tetra iodo-3,10,17,24-tetra (3-methoxy prop-1-nyl) ZnPc (6)

3.3.6 Synthesis of 4-iodo-5-ethylsufonyl phthalimide (7)

The method by İsci *et al.* (2014) was adopted to synthesis of **7** with some modifications. The procedure involved mixing 2.00 g of **1**, 0.18 g (0.26 mM) of $\text{PdCl}_2(\text{PPh}_3)_2$, 10 ml of ethanethiol, 20 ml of diisopropylamine, 0.03 g (0.16 mM) of copper (I) iodide and 3.0 g (21 mM) of K_2CO_3 and placed in a 50 ml two necked round bottom flask as shown in Scheme 3.6. This mixture was left to stir at a speed of 100 rpm at 70 °C for two hours under nitrogen atmosphere. The mixture was cooled to 25 °C by stirring using a glass rod

followed by gravity filtration and residue washed with 20 ml of dichloromethane. The filtrate solution was concentrated by rotary vapor at 40 °C to give a crude product which was purified by using silica gel column chromatography with solvent mixture hexane: ethyl acetate as eluent in the ratio 3:1.

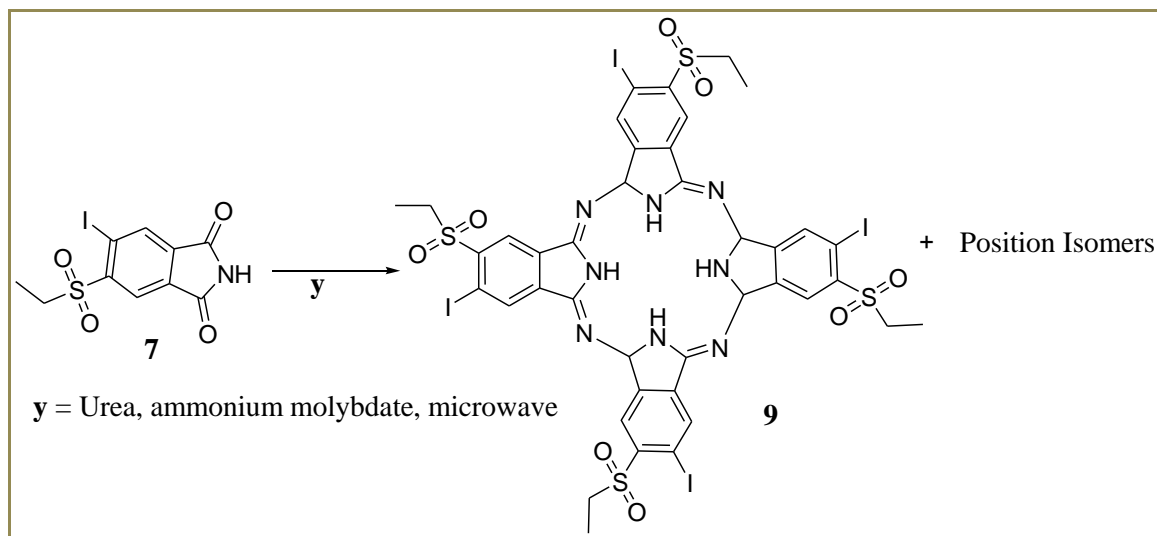


Scheme 3.6: Synthesis of 4-iodo-5-ethylsulfonyl phthalimide (7)

3.3.7 Synthesis of 2,9,16,23-tetraiodo-3,10,17,24-tetraethylsulfonyl Pc (9)

Synthesis of **9** was carried out following a protocol described by Yogesh *et al.* (2014) with some modifications by use of microwave. 0.5 g of compound **7**, 1 g (16.65 mM) of urea and 0.09 g (0.46 mM) of ammonium molybdate were mixed (scheme 3.7). The mixture was crushed thoroughly to form a homogeneous mixture using clean pestle and mortar and transferred to a 250 ml glass beaker then covered with an evaporating dish. The reactants were placed in a microwave oven and heated (high power-800 W) for 3 minutes at one-minute interval and thereafter cooled to 25 °C by stirring using a glass rod. After cooling, the blue solid was transferred to a filter-funnel and washed 3 times with 20 ml of 0.1 M NaOH and, then followed by rinsing with 20 ml 0.1 M HCl respectively. The impurities were removed the formed solid by washing it using

tetrahydrofuran (THF) through silica gel column chromatography. The obtained Pc from the column was dissolved in 40 ml of THF. The Pc was precipitated by the addition of 20 ml methanol and separated by centrifugation at 2000 rpm for 4 minutes

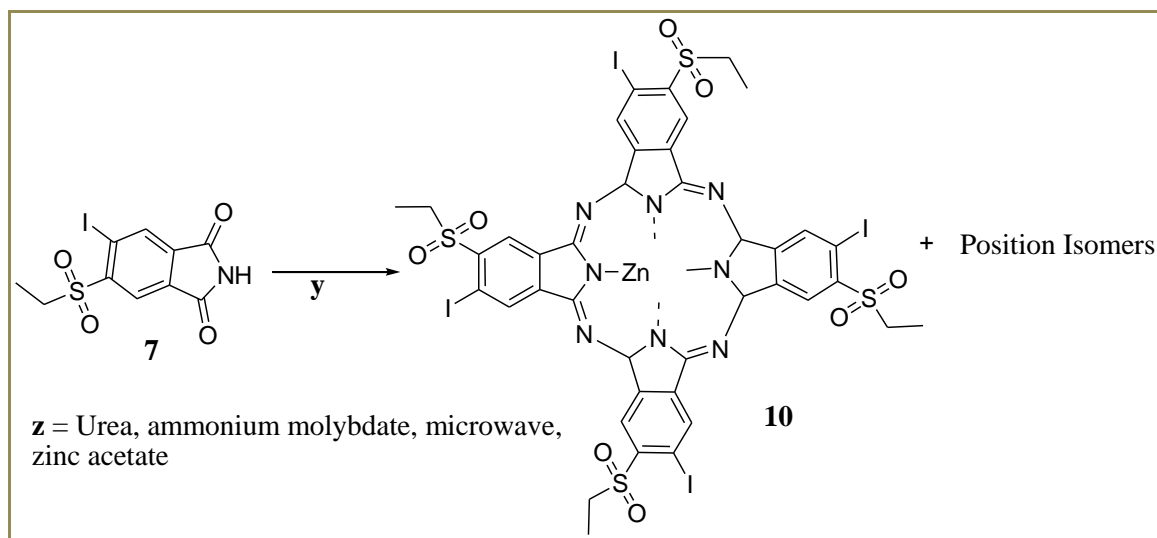


Scheme 3.7: Synthesis of 2,9,16,23-tetraiodo-3,10,17,24-tetraethylsulfonyl Pc (9)

3.3.8 Synthesis of 2,9,16,23-tetraiodo-3,10,17,24-tetraethylsulfonyl ZnPc (10)

The protocol described by Yogesh *et al.* 2014 was used to synthesis compound **10** with some modifications A mass of 0.5 g of compound **7**, 1 g (16.65 mM) of urea, 0.09 g (0.46 mM) of ammonium molybdate and 0.5 g (2.73 mM) of zinc acetate were mixed for a reaction as shown in scheme 3.8. The mixture was crushed thoroughly to form a homogeneous mixture using clean pestle and mortar and transferred to a 250 ml glass beaker then covered with an evaporating dish. The beaker and its contents were placed in a microwave oven and heated (high power-800 W) for 3 minutes at one-minute interval then cooled to 25 °C by stirring using a glass rod. After cooling, the green solid was transferred to a filter-funnel and washed 3 times with 20 ml of 0.1 M NaOH and, then

followed by rinsing with 20 ml 0.1 M HCl respectively. The residue was further purified by washing it using tetrahydrofuran (THF) through silica gel column chromatography. The obtained Pc from the column was dissolved in 40 ml of THF. The Pc was precipitated by the addition of 20 ml methanol and separated by centrifugation at 2000 rpm for 4 minutes



Scheme 3.8: Synthesis of 2,9,16,23-tetra iodo-3,10,17,24-tetra ethylsulfonyl ZnPc (Pc 10)

3.4 Synthesis of metal nanoparticles

3.4.1 Synthesis of AgNps

AgNps were synthesized by chemical reduction protocol described by Wicramarachchi and Hettiarachchi, (2011) with some modifications. In brief, AgNps were synthesized by varying the concentration of silver nitrate from 0.5 to 4 mM to yield AgNp0.5, AgNp1, AgNp2, AgNp3 and AgNp4 nanoparticles as shown in Table 3.1

Table 3.1: Different precursors concentration for synthesis of AgNps

Nanoparticles samples	AgNO₃ (mM)	NaBH₄ (mM)
AgNp0.5	0.5	2
AgNp1	1	2
AgNp2	2	2
AgNp3	3	2
AgNp4	4	2

The nanoparticles labeled AgNp0.5 was synthesized by dissolving 7.57 mg AgNO₃ in 200 ml of ice-cold distilled water, to give a 0.5 mM solution. At the same time, a 2 mM aqueous solution of sodium borohydride (NaBH₄) was prepared by dissolving 33.99 mg of NaBH₄ to 200 ml of ice-cold distilled water. Thirty millilitre of 2 mM NaBH₄ (reducing agent) was transferred in 250 ml conical flasks followed by the addition of 4 ml of 0.5 mM AgNO₃ drop wise while stirring with glass rod.

The conical flask with the content was irradiated in microwave for 30 seconds at high power (800 W). The formed yellow colloidal solution of AgNp1 was allowed to cool to 50 °C, subsequently 10 ml of 10 mM L-glutathione was added while stirring with glass rod for 3 minutes to stabilize the nanoparticles. The powder precipitate of AgNp1 was collected by centrifugation at speed of 5,000 rpm for 10 minutes, and then washed twice with a 100 ml mixed solution of water and ethanol in the ratio of 20: 80 to remove by-products. The final product was oven-dried for 7 hours at 80 °C.

The same procedure was repeated for preparation of other nanoparticles samples labeled AgNp2, AgNp3 and AgNp4 by varying the concentration of AgNO₃ while that of

reducing agent NaBH_4 was maintained constant at 2 mM. The formed AgNps were characterized using UV-Vis and analyzed using FTIR, SEM, TEM and powder XRD.

3.4.2 Synthesis of zinc oxide nanoparticles (ZnO-Nps)

ZnONps were synthesized via a modified wet chemical approach using sodium hydroxide (reducing agent) and zinc nitrate tetrahydrate ($\text{Zn}(\text{NO}_3)_2 \cdot 4\text{H}_2\text{O}$) (Hassan *et al.*, 2018). In brief, ZnONps were synthesized by varying the concentration of zinc nitrate tetrahydrate from 10 to 80 mM. Starch (5 g) (soluble GR for analysis 1.01252 Millipore) used for stabilization was dissolved in 500 ml of distilled water and heated in microwave at high power (800 W) for 2 minutes to obtain a starch solution (0.5 %) and left to cool for 30 minutes to 25 °C.

The synthesis ZnO-Nps involved mixing 20 ml of 1M NaOH with 20 ml of $\text{Zn}(\text{NO}_3)_2 \cdot 4\text{H}_2\text{O}$ (10 mM) solution in a conical flask, followed by the addition of 10 ml of the prepared starch solution for stabilization. The flask and its content were then heated in a microwave oven (high power- 800W) for one minute to form a white colloidal solution, and then cooled to room temperature 25 °C while stirring with a glass rod. The powder precipitate was collected by centrifugation at speed of 1,500 rpm for 15 minutes, and then washed twice with distilled water followed by 10 ml of ethanol to remove by product. The precipitate was then oven-dried at 105 °C for 5 hours. The formed ZnO-Nps powders were then treated by calcinations in the furnace at 500 °C for 5 hours and labeled ZnO-Np10. The procedure was repeated for preparation of other nanoparticles

labeled ZnO-Np40 and ZnO-Np80 with increasing concentrations of $\text{Zn}(\text{NO}_3)_2 \cdot 4\text{H}_2\text{O}$ as shown in Table 3.2.

Table 3.2: Synthesis of ZnO-Nps of different particles size by varying concentration

Solution	$\text{Zn}(\text{NO}_3)_2 \cdot 4\text{H}_2\text{O}$ (mM)	NaOH (M)
ZnO-Np10	10	1
ZnO-Np40	40	1
ZnO-Np80	80	1

3.5 Conjugation of metal nanoparticles to phthalocyanine

The synthesized Pcs were conjugated only with AgNps because it formed the desired particles (5-10 nm), (15-20 nm) and (50-80 nm). ZnO-Nps were not used for conjugation since they formed big particles > 100 nm and aggregated forming secondary nanoparticles.

3.5.1 Conjugation of AgNps with Pc (6) and (10)

The conjugation of metal nanoparticles with Pcs were done following a protocol described by Rapulenyane, (2013). Conjugation was done by taking 0.02 g of AgNps and dissolving them in 20 ml of DMF in a 250 ml beaker. To the solution 0.017g, (0.082 mM) of dicyclohexylcarbodiimide (DCC) was added to activate the carboxylic acid functional groups. The resulting solution was stirred at a speed of 500 rpm for 24 hours at room temperature. Later 10 mg of Pc (6) or (10) in 15 mg (8.5 μmol) of DMF was slowly transferred to the content in the beaker while stirring with glass rod for 15 minutes and left fortnight at room temperature. The Pc-conjugates were obtained by precipitation using methanol, then separated by centrifugation at a speed of 2000 rpm for 10 minutes

and washed three times using ethanol. The formed blue and green solid were then oven-dried at 80 °C for 5 hours and labeled Pc **5AgNp** and Pc **10AgNp** respectively. The complexes were analyzed using UV-Vis, FTIR and TEM.

3.6 Complementary analytical techniques

The Pcs and nanoparticles were analyzed using the following characterization techniques UV-Vis, FTIR, mass spectroscopy, TEM, SEM, XRD, ¹H NMR and ¹³C NMR.

3.6.1 UV-Vis absorption studies

The UV-Vis was used to successful analyze the synthesized Pcs and nanoparticles spectroscopically, by observing Q-bands and the surface plasmon resonance respectively. The Pcs were accurately weighed and used to make standard solutions. Solutions containing different concentration (ranging between 1.00×10^{-5} to 8.00×10^{-5} M) in DMF, DMSO or DCM were prepared under ultrasonic oscillation for UV-Vis analysis using 4 mL cuvettes. The prepared AgNps and ZnO-Nps solution was diluted 3 times with distilled water then put in 4 mL cuvette for UV-Vis. Distilled water was used as the blank. Scanning for metal nanoparticles and Pc was done between 300 to 800 nm.

3.6.2 Determination of functional groups using FTIR

The FTIR analysis was carried out to confirm presence of functional groups in Pcs and the respective functional groups used to stabilize the metal nanoparticles. For Pcs, 0.1500 g was mixed with 15 g of KBr then ground into homogeneous powered and pressed into a pellet at pressure of 5 tons for 5 min in a hydraulic press, the pellet disks were scanned at

wavelength ranging from 350 – 4500 cm^{-1} . The AgNps and ZnO-Nps solution were centrifuged at 5,000 rpm for 10 minutes then filtered. Residue obtained was mixed with KBr in the ratio 1:200 (nanoparticles: KBr) then ground for 2 minutes to form a homogeneous mixture. The formed mixture was compressed into a pellet then subjected for FTIR scanning from 350 - 4500 cm^{-1}

3.6.3 Mass spectroscopy studies

For mass spectral data of Pcs, the stock solution was diluted prior to analysis to a concentration of 5 – 10 $\mu\text{g/ml}$ using a mixture of acetonitrile/DMSO (10:1). ESI-MS data was acquired in the positive ion mode on a QP-2010 plus spectrometer equipped with an ion trap and an electrospray source. All samples were introduced into the electrospray source at flow rate of 3 $\mu\text{L/minute}$. The mass range was 50 – 3000 amu (standard mode) and up to 6000 amu for maximum value. The Ion source voltages were set at 16.7 and 19 kV, while the lens was set at 8.50 kV. The voltages for reflector 1 and 2 were set at 21 and 9.7 kV, respectively for positive ion mode.

3.6.4 Determination of morphology analysis using TEM

The morphology of the samples was investigated using TEM and SEM analysis. TEM micrographs were taken using JEOLTEM 1210 at an accelerating voltage of 100 KV using carbon-coated copper grids for analysis. Sample preparation for TEM was as follows; a drop of the dispersion was diluted with 4 ml of ethanol and subjected to ultrasonic water bath treatment for 5 minutes. A drop of the sample was placed on 230 mesh carbon-coated grids and allowed to air dry at room temperature for 20 minutes then

placed in machine for analysis to generate micrograph. From the micrograph, Image J software was used to compute the particle size of Ag and ZnO-Nps (Granbohm *et al.*, 2018)

3.6.5 Determination of morphology analysis using SEM

SEM analysis was conducted on a JEOL JSM 6100 field emission scanning electron microscope operated at 10-20 kV. Double-sided coated carbon stubs, were used as sample holders. The preparation of the sample was as follows; one gram of the solid sample was placed in 5 ml of ethanol and sonicated for 5 minutes then followed by dilution with 5 ml of water. A drop of the diluted sample was sprinkled on top of a carbon tape, allowed to air dry at room temperature for 30 minutes then subjected for analysis

3.6.6 XRD analysis

Phase purity and the crystallinity nature of Pcs and nanoparticles were determined by powder XRD spectrometer. Prior to the analysis the Pcs and metal nanoparticles were oven-dried at 60 °C overnight, then ground to a fine powder using a pestle and motor. The powder sample mounts were prepared for XRD using front loading by pressing the powder into sample holder cavity (steel rings) with a frosted glass slide to make the surface of the powder mount smooth and flat. The diffractograms were collected at scanning of 1° min^{-1} , filter time was constant at 2.5 s per step, width slit of 6.0 mm and at 2θ ranges recorded with ELISA reader. The XRD pattern of a sample obtained confirmed

by comparing it with diffraction pattern of known standard files stored in the software of the instrument (Bunaciu *et al.*, 2015).

3.6.7 ^1H NMR and ^{13}C NMR spectra studies

For ^{13}C NMR spectra, synthesized Pcs samples were placed in zirconia rotors sample holders. Mono-dimensional spectra obtained at 25 °C and the samples spinned at 10 kHz around the magic angle with a standard cross-polarization pulse sequence. Spectrometer frequencies were set at 100.62 and 400 MHz for ^{13}C and ^1H NMR respectively. A contact time of 2 milli-seconds was set with a period between successive accumulations maintained at 5s to reduce saturation effects and the number of scans maintained at 360. Chemical shift values were referenced to trimethyl silane.

3.7 Determination of photochemical parameters

3.7.1 Determination of fluorescence quantum yield (Φ_F)

The Φ_F was determined following a protocol described by Manieri *et al.*, 2015. The fluorescence spectra of the ZnPc* standard together with synthesized Pcs were obtained by ensuring the absorbance of each at their excitation wavelength was not more than 0.05 to prevent filter effects. ZnPc standard and Pcs were measured in DMSO solvents. The area covered by emission curves were determined to calculate the fluorescence quantum yields using equation 2.1 (chapter 2). ZnPc* was used as a reference standard with $\Phi_F = 0.20$ and refractive index (n_D) = 1.479 in DMSO (at 20 °C and 589 nm)

3.7.2 Determination of singlet oxygen quantum yield ($\Phi\Delta$)

The $\Phi\Delta$ was determined following a protocol described by Manieri *et al.*, 2015. The $\Phi\Delta$ determinations for Pcs were done by using 1,3-diphenylisobenzofuran (DPBF) as an oxygen quencher. The reaction of $^1\text{O}_2$ with DPBF leads to decreasing absorption band at around 420 nm. Briefly, 400 mg of DPBF was dissolved in 20 ml of DMSO, 24 hours before analysis and stored it in the dark. Sample solution was prepared by mixing 14 μl of DPBF with 20 μl solutions of either of the synthesized ZnPc, Pc **5**, Pc **10**, or the Pc conjugated to nanoparticles (Pc-5AgNp and Pc-10AgNp). The irradiation (from 0 s up to maximum 60 s) was carried out in 1 cm path length stoppered cuvette cell and then photolysed at the Q-band (600-700 nm) using a general electric quartz lamp (300 W). A 600 nm glass filter (Schott) was used to filter off infrared and ultraviolet radiations respectively. An interference filter (Intor, 670 nm with a band width of 40 nm) was also placed before the sample. Intensities of light were measured with a POWER MAX5100 power meter and were found to be 4.12×10^{16} photons $\text{s}^{-1} \text{cm}^{-2}$ for $\Phi\Delta$ studies Figure 3.1.

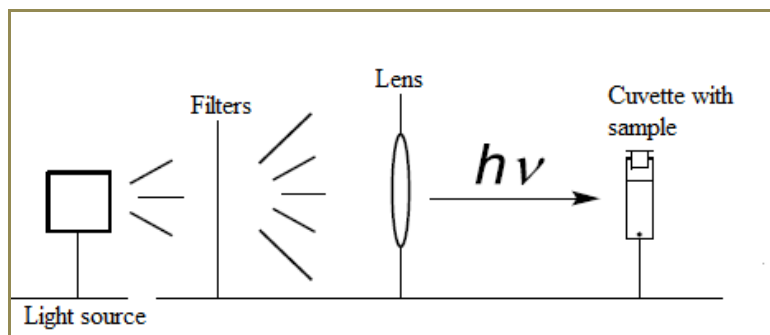


Figure 3.1: Illustration of experimental setup for measurement of singlet oxygen generation.

A UV-Vis graph was plotted for the mixture solution showing maxima absorption bands registered in DMSO. Monitoring of the decay of DPBF was done spectrophotometrically by use of UV-Vis at a wavelength of 420 nm. The equation 2.2 was used to evaluate singlet oxygen quantum yield for the synthesized ZnPc, Pc 5, Pc 10, Pc 5AgNp and Pc 10AgNp. ZnPc* was used as a reference standard in DMSO with $\Phi\Delta=0.56$.

3.8 Antibacterial studies

The biological strains namely *Escherichia coli* (ATCC 25922) (gram negative), *Bacillus subtilis* (ATCC 6633) (gram positive), *Staphylococcus aureus* (ATCC 25923) (gram positive), and *Salmonella typhi* (ATCC 700623) (gram negative) were obtained from the Center for Microbiology Research (CMR) in Kenya Medical Research Institute (KEMRI).

3.8.1 Determination of zone of inhibition

The method of determining the zone of inhibition of antibacterials was adopted from the National Committee for Clinical Laboratory Standards (NCCLS) (CLSI, 1999). Pure bacterial cultures *B. subtilis*, *S. typhi*, *E. coli*, and *S. aureus* were sub-cultured for 24 hours. Inoculum suspension was prepared for bacteria species using a sterile inoculation loop to select independent similar colonies to be added to a saline solution. The turbidity bacterial suspension mixed with of 0.5 MacFarland was analyzed against a white background with a contrasting black line. A spectrophotometer (microplate reader-Biochrom, MA, USA) helped to make sure each bacterium suspension was of equal turbidity with absorbance reading of 0.08-0.1 at 625 nm (Eleonor, 2004). After

confirmation the inoculum formed was of correct turbidity, it was smeared onto growth medium using a sterile cotton swab. Stock solutions of the respective test compound were prepared by dissolving grounded compound in DMSO to a final concentration of 1000 µg/ml. The serial dilutions from the stock solution were made ranging from 500-3.91 µg/ml. The dissolved discs paper (6 mm) in AgNps, Pc 5, Pc 10, conjugated Pcs, ciprofloxacin, and DMSO (in the prepared dilutions) were put on the petri dishes with spread bacteria and incubated in dark and another set irradiated using general electric quartz line lamp (GE EXR 300 W) for 24 hours at 37 °C. Ciprofloxacin was used as a positive control and DMSO as a negative control. Zones of inhibition caused by the test compounds were determined after 18 hours of incubation by measuring it from the back of the agar dish, against a dark background using reflected light. All tests were replicated three times and the results are given as the means and standard error of the means (SEM) of the diameters of the zones of growth inhibition.

3.8.2 Determination of Minimum inhibitory concentration (MIC) and minimum bactericidal concentration (MBC)

The MIC for each test compound was determined by broth microdilution method according to CLSI standard (CLSI, 1999). The synthesized Pcs were dissolved in DMSO to give a stock solution of 1000 µg/ml. The prepared serial dilutions from the stock solutions of Pcs ranging from 500-3.91 µg/ml were used to determine the MIC. Firstly, 90 µl of Mueller-Hinton broth was dispersed in each well of microtitre plates (Figure 3.2). An aliquot of 100 µl from solution of Pc was added into the wells from column 1 to 10. Finally, 10 µl from each microbial suspension (1×10^6 CFU/ml of *B. subtilis*, *E. coli*,

S. typhi or *S. aureus*) was added to all the wells from column 1 to 11. Positive control consisted of antibiotic, Mueller-Hinton broth and test organism. Sterility control (column 12) consisted of Mueller-Hinton broth and DMSO. The well plates were covered and incubated in the dark and another set irradiated using a general electric quartz line lamp (300 W) both for a period of 24 hours at 37 °C. The highest dilution of the tested Pcs to inhibit growth (no turbidity in the tube) was considered as the MIC value of this Pcs batch against the tested bacterial species.

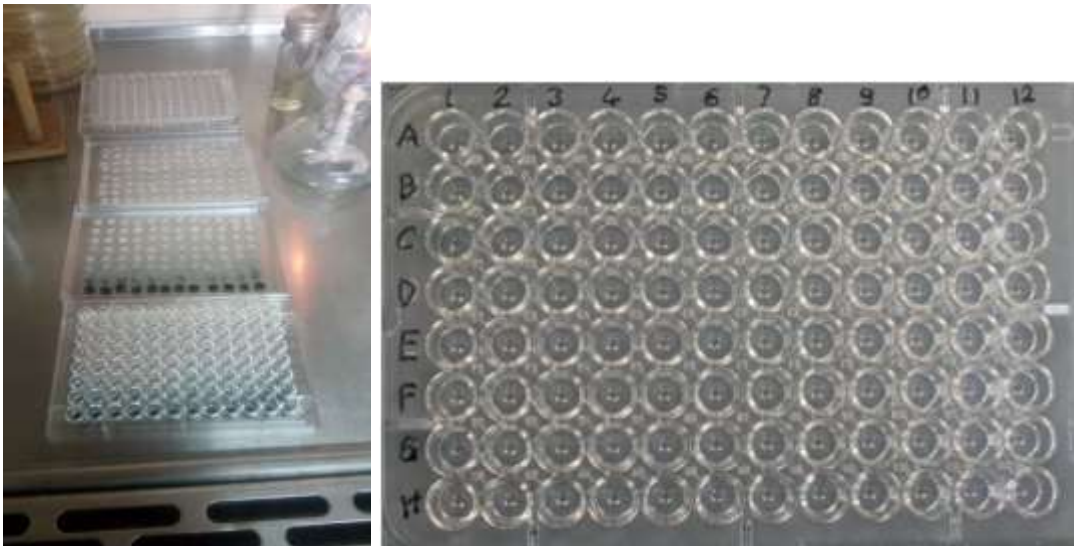


Figure 3.2: Layout of 96 well microtitre plate

The MBC were determined by a method based on the CLSI standard (CLSI, 1999). This was done by taking the tubes that showed no growth signs or with no visible signs of turbidity in MIC, loopfuls were inoculated by streak plate method onto sterile Mueller Hinton agar plates. The plates were then incubated overnight at 37 °C. The least

concentration that did not show any growth of tested bacteria's was considered as the MBC value of the tested Pcs compound against the tested bacterial species.

3.8.3 Cytotoxicity test

Vero cells (African green monkey kidney cell lines) were obtained from the Center for Microbiology Research (CMR) in Kenya Medical Research Institute (KEMRI). The cytotoxicity of compound **5** and **10** were evaluated on Vero cells using 3-(4,5-dimethylthiazol-2-yl)-2,5-diphenyl tetrazolium bromide (MTT) test following the protocol by Mosmann (1983). The test compounds were prepared by dissolving 10 mg of each compound in 100 μ l DMSO followed by the addition of 9900 μ l of phosphate buffered saline (PBS) to make 10,000 μ g/ml of stock concentration. The MTT stock solution was prepared by dissolving 500 mg of MTT powder in 10 ml PBS. The resulting mixture was stirred with a magnetic stirrer at 500 rpm for 10 minutes at room temperature. The mixture was filtered using a 0.22 mm syringe filter (MF-millipore membrane filter) then stored in the dark

Vero cells (100 μ l/well) were put in 96-well culture plates ensuring concentration of 2×10^4 cells in columns 1, 2, 4, 5, 7, 8, 10 and 11 while columns 3, 6, 9 and 12 served as control. The cells were allowed to incubate for 24 hours to culture at 37 °C in a humidified atmosphere with 95% O₂ and 5% CO₂ to maintain the pH. After 24 hours incubation, the test compounds with two-fold serial dilution were added starting with high concentration in the first row (500-3.91 μ g/ml). The whole set was carried out in duplicate and the cell together with the test compounds incubated for 48 hours for

interaction. After 48 hours, 10 μ l of MTT dye was added to all the wells and incubated for 3 hours for crystals of formazan to be formed (purple in color) (Figure 3.3). At the end of the third hour, the formed formazan crystals were dissolved in 100 μ l of DMSO. The absorbance intensity of each well was measured using a standard microplate reader set at a wavelength 540-720 nm. Cell viability was calculated using Equation 3.1

$$\% \text{ Cell viability} = \frac{\text{Absorbance of the sample}}{\text{Absorbance of control}} \times 100 \dots \text{Equation 3.1}$$



Figure 3.3: Conversion of MTT into a purple colored formazan for compound 5 and 10 with Vero cells

3.9 Data analysis

Mean values, standard deviation (SD) and ANOVA analysis was done using the SPSS data software version 19.0. Post hoc analysis was done using Turkey at 95% confidence level. Results were significant when $P > 0.05$.

CHAPTER FOUR

RESULTS AND DISCUSSION

The chapter reports on the results of synthesis and characterization of precursors, Pcs, AgNps, ZnO-Nps and Pcs-nanoparticle conjugates. Photochemical and antibacterial studies are also discussed.

4.1 Synthesis and characterization of precursors and Pcs

4.1.1 Synthesis of 4,5-diiodophthalimide (1)

The synthesis of compound **1** yielded a white powder with a mass of 22.00 g. The compound had a melting point of 298-300 °C at 1 atmospheric pressure. It was soluble in DCM, CHCl₃, THF, acetonitrile, toluene, DMF and DMSO. FTIR spectrum of compound **1** displayed peaks of strong intensities at (KBr) 3438 (N-H), 2270 (C-N), 1870 (C=O), 1760 (C-H), 570 (C-I) cm⁻¹ as shown in Figure 4.1. The results are in agreement with that obtained by Andrew *et al.* (2016).

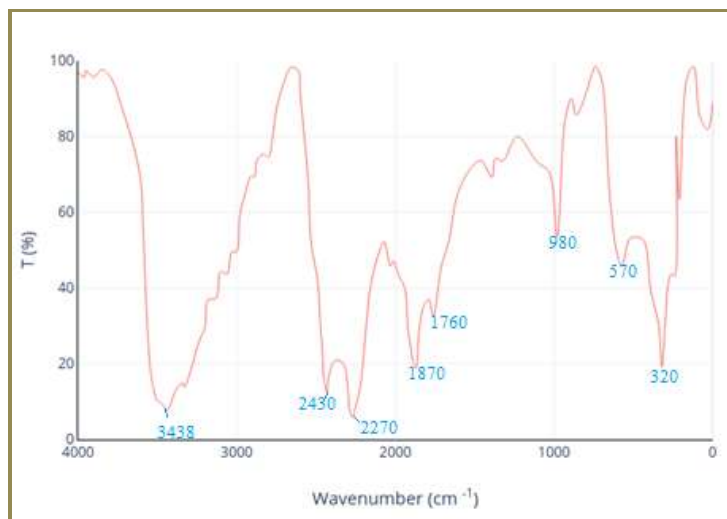


Figure 4.1: FTIR spectrum of 4,5-diiodophthalimide (1)

UV-Vis spectrum of compound **1** was recorded with values between 300-800 nm. It had a remarkable characteristic absorption at the wavelength 360 nm (Figure 4.2), due to aromatic π system and C=O in the carboxylic structure. The results were comparable to that obtained by Nayab *et al.* (2015).

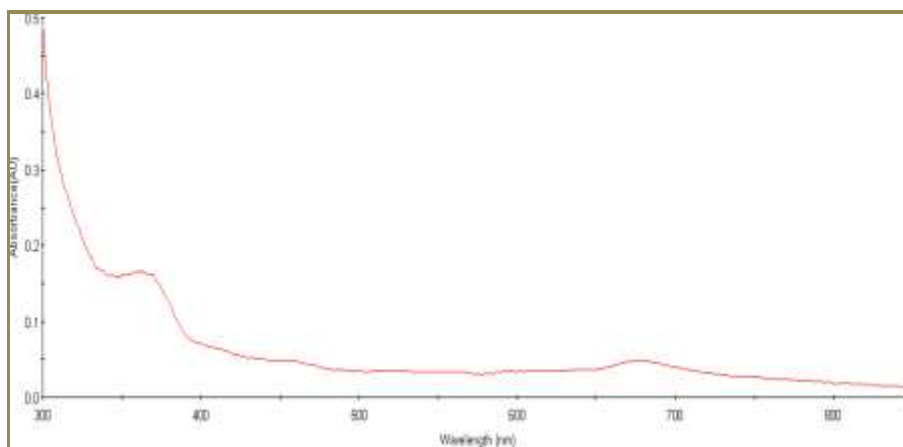


Figure 4.2: UV-Vis spectrum of 4,5-diiodophthalimide (1)

The ^1H NMR spectrum of compound **1** gave 3 protons, a single peak at $\delta = 8.31$ (s, 2H, ArH) depicted for the aromatic protons and another single peak at 11.50 (s, 1H) for -NH as shown in Figure 4.3. The two protons that were chemically equivalent suggests that compound **1** was symmetrical. The ^{13}C NMR spectrum displayed 8 C-atoms with peaks between 70 and 160 ppm representing carbon in aromatic rings as shown in Figure 6.1 (Appendix 1) with the following chemical shifts ^{13}C NMR (100.62 MHz, d-DMSO, 25°C) δ C 167.50, 137.90, 131.70, 127.95, 120.12, and 70.08 (Ar-C) ppm. The HR-MS spectrum of compound **1** gave m/z ratio of 398.8253 while the m/z ratio calculated molecular ion $\text{C}_8\text{H}_3\text{I}_2\text{NO}_2$ [M^+] was 398.9113 as shown in Figure 6.2 (Appendix 1). These values were in agreement with data reported by Dokládlová *et al.* (2014) of a 4,5-

diiodophthalimide with molecular formulae $C_8H_3I_2N_2O_2$ therefore confirming formation of compound **1**

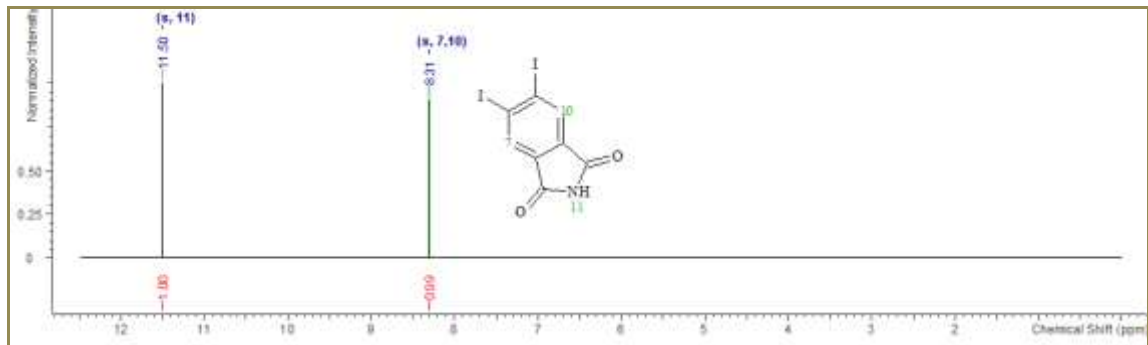


Figure 4.3: 1H NMR spectrum of 4,5-diiodophthalimide (**1**)

Substituted phthalimide **2** and **7** precursors 4-iodo-5-(3-methoxy prop-1-nyl) and 4-iodo-5-ethylsulphonyl phthalimide respectively needed for synthesis of Pcs were derived from 4,5-diiodophthalimide (**1**).

4.1.2 Synthesis of precursors **2** and **7**

Mono-substituted phthalimide **2** and **7** used as coupling agents for Pc precursors was carried out by nucleophilic substitution reactions using compound **1**. Formation of compound **2** yielded a white solid with a mass of 10.20 g. The compound had a melting point of 86-88 °C at 1 atmospheric pressure. While compound **7** yielded a white solid with a mass of 18.50 g with a melting point of 77-80 °C at 1 atmospheric pressure. Both solids were soluble in DCM, $CHCl_3$, THF, acetonitrile, acetone, toluene, DMF and DMSO.

The FTIR spectrum of compound **2** and **7** had characteristic peaks at around 3270-3400 representing N-H, 2740-3010 for C-H stretch and 2020-2580 (C=O) all attributed to phthalimide. Precursor **2** had an extra band at 1890 representing C≡C due to propynyl while precursor **7** showed a distinct peak at 2480 due to sulphonyl group (S-H) (Table 4.1). These values were in agreement with data reported by Yang, 2006 for substituted phthalimide.

Table 4.1: FTIR bands for precursors 2 and 7

Precursors	FTIR (KBr) (cm ⁻¹)		Figure
	Characteristic bands	Other bands	
2	3350, 3270, (N-H), 2890, 2740, 2680 (C-H stretch), 2580, 2440, 2380, 2020 (C=O)	1890 C≡C 1430, 1240 (C=C), 1100, 1020 (C=O)	6.3 (Appendix)
7	3400, 3290 (N-H), 3010, 2980 (C-H stretch), 2430, 2330, 2200, 2100 (C=O)	2640, 2600, 2480 (S-H), 1330 (C-N), 1000, 840	6.4 (Appendix)

¹H NMR spectra of the precursors **2** and **7** were recorded in d-DMSO and the values are given in Table 4.2. Both precursors gave a total of 8-protons, two of which are aromatic proton peaks attributed to phthalimide. The ¹³C NMR spectrum of precursor **2** displayed 12 carbon atom peaks while precursor **7** had 10 C-atoms peaks with peaks between 128 and 158 ppm representing carbon in aromatic rings for both. The values were in agreement with that reported by Eissa, (2014) for ¹³C-NMR of phthalimides compounds with peaks at 120-160 ppm due to aromatic carbons

Table 4.2: ^1H NMR and ^{13}C NMR chemical shifts for precursors 2 and 7

Precursor	^1H NMR		^{13}C NMR		
		Figure	Aromatic carbon	substituents	Figure
2	8.54 (1H; Ar-H); 8.43 (1H; Ar-H); 6.89 (1H; s; -NH); 4.07 (2H; s; -CH ₂ -); 2.96 (3H; s; -CH ₃).	6.5 (Appendix)	δ c 158.50, 151.00, 139.00, 136.90, 135.50	128.00, 120.90, 116.00, 110.90, 78.83, Py-C 27.30 (OCH ₂), 22.90	6.7 (Appendix)
7	8.22 (1H; Ar-H); 7.97 (1H; Ar-H); 6.97 (1H; s; -NH); 4.50 (2H; s; -CH ₂ -); 2.69 (3H; s; -CH ₃).	6.6 (Appendix)	δ c 157.80, 155.40, 144.40, 136.80, 128.10	116.20, 115.90, 40.08, 23.80, 18.30, Py-C	6.8 (Appendix)

The HR-MS spectrum of precursor **2** gave m/z ratio of 341.439 while the m/z ratio calculated molecular ion, C₁₂H₈INO₃ [M⁺] was 341.109 (Figure 6.9). Precursor **7** gave m/z ratio of 332.9320 while the m/z ratio calculated molecular ion, C₁₀H₈INO₂S [M⁺] was 333.1500 (Figure 6.10)

4.1.3 Synthesis of un-substituted ZnPc (**4**)

Formation of compound **4** gave 7.5 g of the desired pure product as deep blue powder. The compound had a melting point of 397-400 °C at 1 atmospheric pressure. It was found soluble in DMF, DCM, DMSO and THF

The FTIR spectrum of **4** had strong absorption peak at 3580 representing N-H stretch, a at 3080 cm⁻¹ peak represent C-H stretching vibration of the aromatic ring. The C=C and

C=N bond have similar bond lengths which appeared at around 1730 cm^{-1} and 1460 cm^{-1} Figure 6.11 (Appendix 1). The UV- Vis spectrum of **4** showed Q band at 672 nm and B or Soret band appeared at 353 nm in DMSO Figure 6.12 (Appendix 1). Both formations of Q and B band confirmed the formation of **4** (Tayfuroğlu *et al.*, 2018).

The formed spectra of **4** showed distinctive ^1H chemical shifts (δ) in the aliphatic (1.23-4.10 δ) and aromatic (7.70-9.30 δ) regions of the spectra Table 4.3 and Figure 6.13 (Appendix 1). The chemical shift of ^{13}C NMR aromatic carbon atoms appeared in the range of δ 120–150.90. The results are comparable to that obtained by (Burat and Karaoğlu, 2020) with aromatic carbons of the Pcs appearing in the region between δ 120 – 160 ppm Table 4.3 and Figure 6.14 (Appendix 1). The HR-MS spectrum of **4** gave m/z ratio of 578.20 while the m/z ratio calculated molecular ion, $\text{C}_{32}\text{H}_{16}\text{N}_8\text{Zn} [\text{M}^+]$ was 576.08

Table 4.3: ^1H NMR and ^{13}C NMR bands for precursors **4**

Precursor	^1H NMR		^{13}C NMR	
4	δ ppm 0.84 (s, 2 H) 1.23 (s, 3 H) 1.73 (ddd, $J=9.98$, 7.05, 3.05 Hz, 1 H) 2.16 (s, 9 H) 2.54 (s, 1 H) 3.58 (s, 4 H) 3.81 (s, 2 H) 4.10 (s, 1 H) 7.70 (d, $J=1.52$ Hz, 1 H) 7.74 (d, $J=1.78$ Hz, 1 H) 8.07 (s, 4 H) 9.04 (s, 1 H) 9.30 (s, 4 H)	Figure 6.13 (Appendix)	δ c 120, 121.85, 127.58, 127.82, 129.24, 130.67, 131.16, 132.17, 136.77, 150.62, 152.90 (ar C)	Figure 6.7 (Appendix)

4.1.4 Synthesis of metal-free Pc 5 and Pc 9

Self-condensation of compound **2** and **7** after purification yielded a blue solid Pc **5** and **9** respectively. Pc **5** had a mass of 4.50 g and a melting point of 327-330 °C while Pc **9** had a mass of 3.12 g and melting point of 350-352 °C. Both the metal-free Pcs were found to be soluble in DCM, DMF, CHCl₃, DMSO and THF

The FTIR spectrum of Pc **5** and **9** gave peaks that depicted skeletal vibration of Pc as shown in Table 4.4. The disappearance of C=O peak in the spectra of pc **5** and **9**, proved the cyclotetramerization of phthalimide **2** and **7** respectively to form metal free Pc **5** and **9**. The result are comparable to that obtained by Ziminov *et al.* (2006). Peaks at 980 and 1040 represents CH due to pyrrole rings formed due to formation of Pc. Sakamoto and Ohno-okumura, 2009 indicated that peaks around 1,600 cm⁻¹ are represent C=C of aromatic ring of the Pc while those between 1,200 cm⁻¹ and 950 cm⁻¹ region represent absorption due to out-of-plane bending for N-H and C-H in pyrrole rings of Pcs.

Table 4.4: FTIR bands for 5 and 9

Pc	FTIR (KBr) (cm ⁻¹)		Figure
	Characteristic bands	Other bands	
5	3450 (N-H stretch), 2870, 2840, 2790, (C-H stretch), 1790 (N-H bending), 1560 (C=C), 1330 (C-H bending), 1190 (C-N), 980 CH in pyrrole ring	2580, 2470, 2350, 2200, 2060, 1950 (C≡C), 1100 (C-O)	6.15
9	3420 (N-H), 2700 (C-H stretch), 2390, 2320, 2260, 2080, 1910, 1860, 1790 (N-H bending), 1580 (C=C), 1460 (C-H bending) 1190 (C-N), 1040 CH in pyrrole ring	2640, 2550 (S-H), 1190, 1130, 700, 580	6.16

4.1.5 Synthesis of Pc 6 and Pc 10

Substituted Pc **6** and Pc **10** were successfully synthesized by cyclotetramerization of purified substituted phthalimide **2** and **7** in presence of zinc acetate to form respective metal Pcs. The use of 4,5-disubstituted phthalimide lead to 2,9,16,23-identical substituted Pcs without forming isomeric mixtures of Pcs.

Formation of Pc **6** yielded 3.47g of the desired pure product as blue solid with melting point of 350-352 °C, while Pc **10** yielded a green solid with a mass of 2.89 g and melting point 327-330 °C. Table 4.5 shows solubility of Pc **6** and Pc **10** in different solvent. Most alkylated compounds have been found to be soluble in organic solvents such as DMSO and DMF. Solvents that are able to dissolve Pcs are important in reducing aggregation of the Pcs. Pc **10** was very soluble in water as compared to Pcs **6** this may be because of the attached sulfonyl group. Because of the high solubility of Pc **10**, it makes it to have stronger absorptions in the Q band as compared to Pc **6**. Figure 4.4 shows the blue and green color of Pc **6** and **10** respectively dissolved in DMSO

Table 4.5: Solubility of Pc 6 and 10 (+++ soluble, ++ sparingly soluble, - not soluble)

Pc	Solubility					
	H ₂ O	DMF	DMSO	THF	Acetone	DCM
Pc 6	++	++	+++	++	-	++
Pc 10	+++	+++	+++	++	-	+++



Figure 4.4: Color of Pc 6 and 10 when dissolved in DMSO

Pc **6** and **10** had FTIR peaks shown in the Table 4.6 The disappearance of the C=O stretching vibration (in precursor **2**) and not appearing in the spectra of Pc **6** and **10**, proved cyclotetramerization of compound **2** and **7** to form substituted metal-Pcs. The result are in agreement with that obtained by Ziminov *et al.* (2006). From Saravanan *et al.* (2006) work, peaks between 1400 cm^{-1} and 1250 cm^{-1} are represent stretching vibrations of C–N of benzene ring forming Pc. The results are also comparable to that reported by Georgescu *et al.* (2015) in which most intense bands of their Pc compound could be seen in the range $1300\text{-}1600\text{ cm}^{-1}$ which is generally due to the C-C pyrole.

Table 4.6: FTIR bands for 6 and 10

Pc	FTIR (KBr) (cm^{-1})		Figure
	Characteristic bands	Other bands	
6	3480, 3400 (N-H), 2710, 2640, 2400 (C-H stretch), 1810, (N-H bend), 1610 (C-C), 1480 (C-H bending)	2320, 2130, 1940 (C \equiv C), 1160 (C-N), 1090 (C-O), 990, 500 (skeletal vibration of Pc)	6.17
10	3530, 3450, 3380 (N-H), 2800 (C-H), 1980, 1840 (N-H bending), 1680 (C-C), 1540 (C-H bending)	2580, 2480 (S-H), 1360, 1230 (C-N), 1140, 1020	6.18

The UV-Vis spectrum of compound **6** and **10** showed Q band at around 600-700 nm in different solvents (Table 4.7). This may be because of transition of $\pi\pi^*$ from the highest occupied molecular orbital to the lowest unoccupied molecular orbital of the Pcs ring (Tayfuroğlu *et al.*, 2018). The B-band for both Pcs was also observed between 300-370 nm in various solvents (Table 4.7), occurring due to deeper π levels to lowest unoccupied molecular orbital transition. The formations of Q- and B-band confirmed the formation of Pcs, as the starting precursor (**2**) had only one elaborate peak at around 360 nm

representing a B-band. The results were comparable to that done by Kantekin *et al.* (2008) which showed B- and Q-bands for their substituted metal-Pc. The absorption B- and Q band of the Pc varied with the solvent used which was in consistency with the work done by Furuyama *et al.* (2019).

Table 4.7: UV-Vis absorption of Pc 6 and 10 in different solvents

Solvent	Pc 6 (Figure 6.19 Appendix 1)		Pc 10 (Figure 6.20 Appendix 1)	
	λ max nm (log ϵ) B Band	λ max nm (log ϵ) Q Band	λ max nm (log ϵ) B Band	λ max nm (log ϵ) Q Band
DMF	345 (4.71)	613 (4.75), 680 (5.40)	365 (5.07)	620 (4.35), 685 (5.04)
DMSO	350 (4.80)	622 (3.99), 680 (4.71)	354 (4.26)	625 (4.40), 698 (5.08)
DCM	364 (4.06)	622 (4.34), 680 (4.70)	360 (4.59)	625 (4.07), 689 (4.41)

A comparison of the position of the Q-band maximum of ZnPc, Pc **6** and **10** (Figure 4.5) revealed that Pc **10** exhibited a red shift in Q-band with comparison to ZnPc and Pc **6** in all solvents, due to the electron withdrawing nature of sulfonyl groups in the compound (Ogata *et al.*, 2003). This was in agreement with the work done by Nemykina and Lukyanets (2010) that revealed substitution with electron-withdrawing groups at peripheral position leads to a red shift of the Q-band.

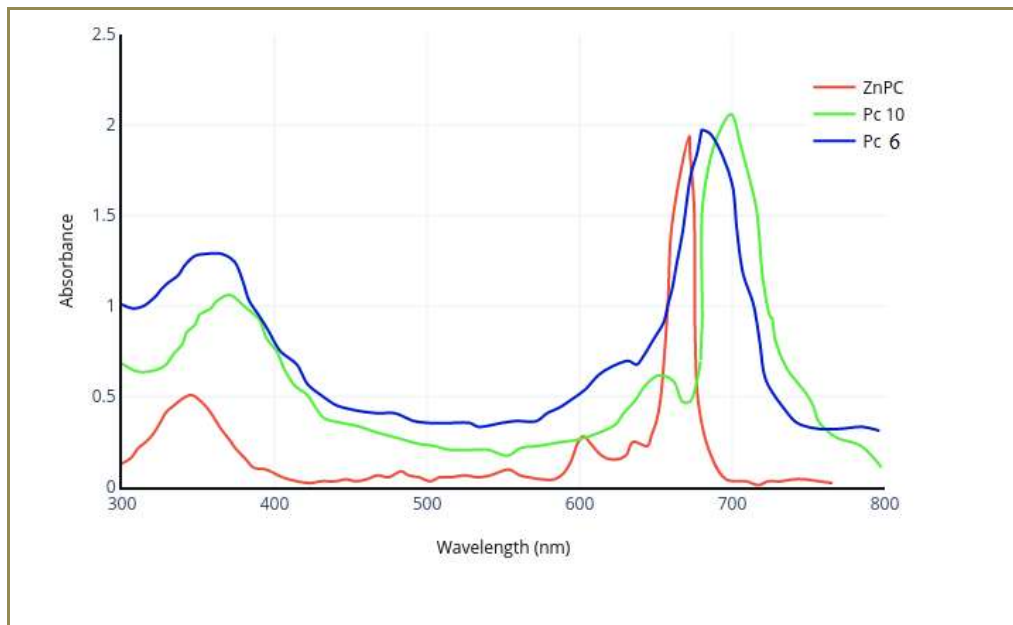


Figure 4.5: UV-Vis spectrum of ZnPc, Pc 6 and Pc 10 in DMSO

^1H NMR spectra of the Pc **6** and **10** were carried out in d-DMSO (Table 4.8). The formed spectra of Pc **6** and **10** showed distinctive ^1H chemical shifts (δ) in the aliphatic (1.39-4.52 δ) and aromatic (7.59-9.04 δ) regions of the spectra. Absorptions in the aliphatic region are attributed to methoxy prop-1-nyl and ethylsulfonyl substituents. In the aromatic region the peaks are as a result of Pc ring. The results were in agreement to that obtained by Tayfuroğlu *et al.* (2018), they found out that protons for aromatic Pc ring for peripherally tetrasubstituted complexes were observed in the range 8.70 to 6.50 ppm and 5.00 to 1.30 for O-CH₃ affiliated to aliphatic protons.

Table 4.8 shows values obtained for ^{13}C -NMR for Pc **6** and **10**. The results in the region 13.79 - 48.69 ppm are associated to unique carbon of aliphatic substituents while aromatic carbons of the Pcs are unique in the region with chemical shift between δ 120 – 160 ppm. Absorptions from the carbons of the synthesized Pc **6** and **10** can be seen as

four tall peaks at this region representing aromatic carbons of the Pcs. The results are comparable to that obtained by Burat and Karaoğlu, (2020) for their synthesized Pc, the chemical shift of ^{13}C NMR aromatic and aliphatic carbon atoms appeared between the values δ 146.6–104.5 ppm and δ 76.0–14.0 ppm, respectively. The results were in agreement to those obtained by Kantekin *et al.* (2008) for nickel Pc with aromatic carbons between the region δ 120-160 ppm.

Table 4.8: ^1H NMR and ^{13}C NMR spectral data of Pc 6 and 10

Pc	^1H NMR			^{13}C NMR		
	Aromatic proton	Substituents	Figure	Aromatic carbon	Substituents	Figure
6	7.66-7.72 (s, 4H, Ar-H), 8.07 (s, 2H, Ar-H), 9.04 (s, 2H, Ar-H)	3.80 (s, 12H, -CH ₃), 4.14 (s, 8H, -CH ₂)	6.21	121.57 (Ar, CH), 121.90 (Ar, CH), 123.50 (Ar, CH), 127.50 (Ar, CH), 136.12, 140.04 (Ar, CH), 154.14 (Ar, CH)	15.03 (Al-CH ₃), 35.62 (N-CH ₃), 40.00, 44.05 (N-CH ₃),	6.23
10	7.59 (1H, d, J = 0.5 Hz-ArH), 7.70 (1H, d, J = 0.5 Hz-ArH), 8.37 (1H, d, J = 0.5 Hz-ArH), 8.46 (1H, d, J = 0.5 Hz-ArH), 8.54 (1H, d, J = 0.5 Hz-ArH), 8.63 (1H, d, J = 0.5 Hz-ArH), 8.70 (1H, d, J = 0.5 Hz-ArH), 8.93 (1H, d, J = 0.5 Hz-ArH).	1.39 (3H, d, J = 7.1 Hz-CH ₃), 1.45 (3H, d, J = 7.4 Hz - CH ₃), 1.47-1.57 (6H, 1.50 (d, J = 7.3 Hz - CH ₃), 1.54 (d, J = 7.3 Hz)), 3.59 (s, 2H), 3.81 (s, 2H), 4.44 (1H, q, J = 7.3 Hz-CH), 4.48-4.55 (3H, 4.53 (q, J = 7.4 Hz-CH), 4.50 (q, J = 7.1 Hz), 4.52 (q, J = 7.3 Hz))	6.22	154.14 (Ar, CH; Pc), 140.07 (Ar, CH; Pc), 136.41, 127.50 (Ar, CH; Pc), 123.54, 122.18 (Ar, CH; Pc)	48.69, 40.07, 35.68, 30.48 (Al-CH ₂), 29.25 (Al-CH ₂), 25.07 (Al-CH ₂), 21.81 (Al-CH ₂), 13.79 (Al-CH ₂)	6.24

The powder X-ray diffraction pattern for the synthesized Pc **6** and **10** obtained is shown Figure 6.25 and 6.26 respectively (Appendix 1). The diffraction patterns for the Pcs are in the range 2θ angles $15-40^\circ$. It showed that they are a β -form with monoclinic structure. For amorphous compound the non crystalline portion always scatters the X-ray beam to give a continuous base line (Eissa, 2014). The X-ray diffraction patterns were comparable to results obtained by Varghese *et al.* (2017). The XRD pattern for Pc **10** was notably different from that of Pc **6**. The peaks for Pc **10** are scattered upto 38° while for Pc **6** the last peak is at 28° . The highest peak for Pc **10** appeared at 25.8° and this may be attributed to the attached functional group ethylsulfonyl.

Mass spectrum of Pc **6** gave m/z ratio of 1288.45 while the m/z ratio calculated molecular ion, $C_{48}H_{28}I_4N_8O_4 [M^+]$ was 1288.40 (Figure 6.17 Appendix 1). The Pc **10** mass spectrum gave m/z ratio of 1256.8015 while the m/z ratio calculated molecular ion, $C_{40}H_{28}I_4N_8S_4 [M^+]$ was 1256.5800 (Figure 6.28 Appendix 1).

4.2 Synthesis and characterization of ZnO-Nps and AgNps

ZnO-Nps and AgNps were synthesized by chemical method through microwave-assisted synthesis. During the synthesise process metal nanoparticles was visually monitored by the color change of the formed solution and through UV-Vis spectrophotometer. The analysis of the synthesized ZnO-Nps and AgNps was carried out using FTIR, Powder XRD, SEM and TEM. The characteristic change of color of AgNp was from cream in low concentration to yellow then to brown in higher concentration as shown in Figure

4.6. This is because of excitation of metal nanoparticle lattice that occurs during formation bringing about surface plasmon resonance (Chhatre *et al.*, 2012).

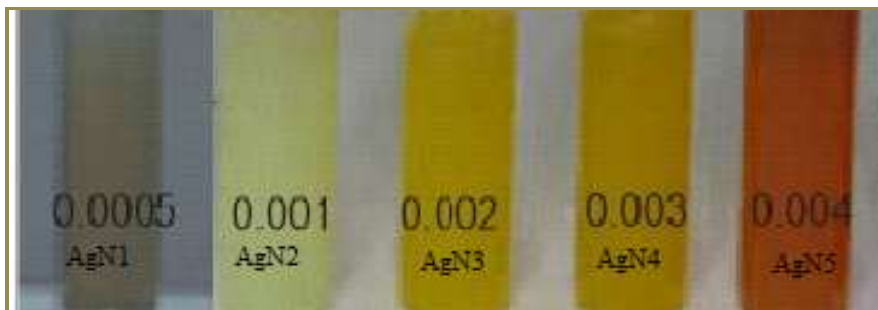


Figure 4.6: Distinctive colour of different sized silver nanoparticles

4.2.1 FTIR spectrum of ZnO-Np and AgNp

The FTIR analytical method was used in order to show the presence of functional groups in the metal nanoparticles. Broad peak occurring at 3430 cm^{-1} for ZnO-Np spectrum represents the OH stretching band brought about by water adsorption on the surface of ZnO-Np while the peak at 670 cm^{-1} represents Zn-O stretching vibration (Figure 6.29 Appendix 1).

Glutathione was used to stabilize AgNp in solution, the FTIR peak at 1840 cm^{-1} represent -SH stretch for thiol group in glutathione. Peak at 1400 cm^{-1} is due to a COO^- functional group and a peak at 3150 cm^{-1} represents NH_3^+ stretches due to glutathione (Figure 6.30 Appendix 1). After addition of glutathione as stabilizing agent to AgNps solution, the FTIR spectra revealed no shift of peak for COO^- functional group. The new spectra had stabilized AgNps had no peak for -SH proving thiol had interacted with the surface of

AgNps. The –SH functional group ends up forming a weak bond with the AgNps due to positive ion charged. This makes stabilization of AgNps with glutathione possible as the positive Ag ions get surrounded by the negatively charged –SH functional group reducing chances of aggregation (Murariu *et al.*, 2014).

4.2.2 Powder XRD analysis of ZnO-Nps and AgNps

Synthesized ZnO-Nps and AgNps crystallinity were analyzed by use of Cu-K α X-ray diffractometer. The XRD diffraction patterns are given Figures 6.31 and 6.32 respectively. The peaks for ZnO-Np appeared at 31.77°, 34.44°, 36.28°, 47.60°, 56.52°, 62.88°, and 67.96°. These peaks were comparable to that reported in the literature report by Pelicano *et al.* (2017) and also well in consistent with standard file (number 01-075-0576) indicating similarities to hexagonal phase of zinc oxide (Pelicano *et al.*, 2017).

The X-ray diffraction of AgNps had the following diffraction angles at $2\theta = 38.20^\circ$, 44.40° , 64.59° and 77.50° as shown in Figure 6.32 (Appendix 1). These peaks are in agreement with faced center cubic lattice planes of Ag at (111), (200), (220) and (311) respectively (Bhatte *et al.*, 2012). This correspond to the standard file of AgNps JCPDS file no. 00-001-1167 (Mehta *et al.*, 2017).

4.2.3 SEM and TEM analysis of ZnO-Nps and AgNps

The SEM and TEM characterization were done to find the surface morphology of ZnO-Nps and AgNps. The SEM micrographs confirmed the information derived from the XRD diffraction patterns of synthesized ZnO-Nps and AgNps. From the SEM

micrograph (Figure 4.7 **a-d**) it can be seen that AgNps are almost spherical in shape and monodispersed.

The AgNps particles formed were of average size 9.94 ± 1.34 nm, 18.45 ± 2.93 nm, 34.96 ± 6.34 nm, 52.40 ± 2.64 nm and 58.5 ± 5.83 nm. ZnO-Nps were of the mean size 95 ± 6.75 nm, 127 ± 11.75 nm and 152 ± 14.75 nm as shown in Table 4.9. For sample AgNp1, spherical particles were found to be much smaller with mean particle size of 9.94 nm as shown in Figure 4.7 (a). In the case of AgNp5, AgNps had large particle size of 58.5 nm. In all samples there were near-spherical and large particles appearing, which could be as a result of agglomeration of particles. The TEM morphological structure and distribution of particles are comparable to that obtained by Hebeish and El-naggar, (2013).

Table 4.9: AgNps and ZnO-Nps of different size under different concentrations

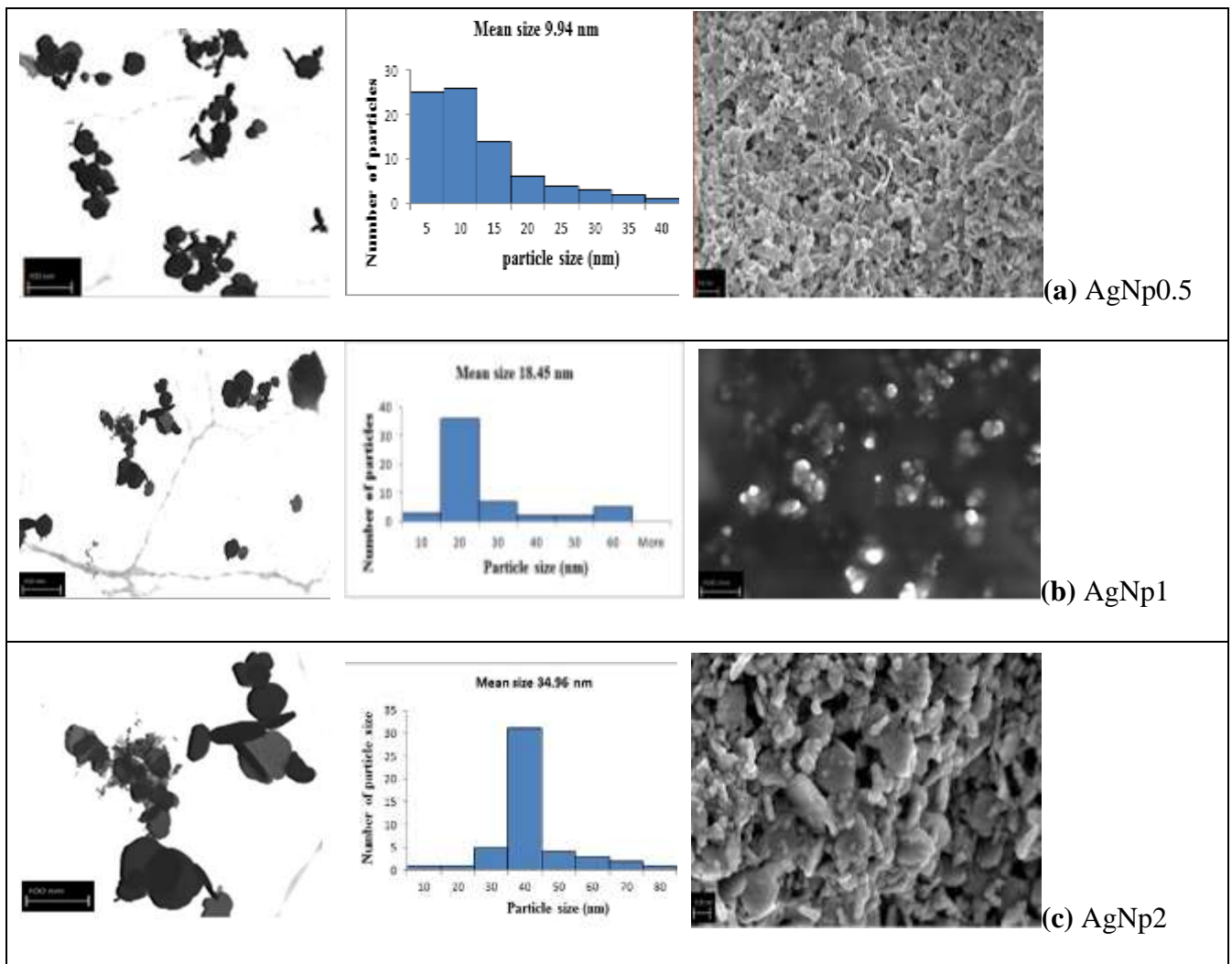
Concentration	AgNps		Concentration	ZnO-Nps	
	Absorbance peak (nm)	Average AgNps size (nm)		Absorbance peak (nm)	Average ZnO-Nps size (nm)
AgNp0.5	394	9.94 ± 1.34^a	ZnO-Np10	358	95 ± 6.75^f
AgNp1	398	18.45 ± 2.93^b	ZnO-Np40	360	127 ± 11.75^g
AgNp2	406	34.96 ± 6.34^c	ZnO-Np80	365	152 ± 14.75^h
AgNp3	411	52.40 ± 2.64^d	-	-	-
AgNp4	420	58.5 ± 5.83^e	-	-	-

Note: Mean value of three replicates with different letters in the same column show a significant difference at $\alpha = 0.05$.

ZnO-Nps had large grains size of > 95 nm with particles being semi- spherical in shape.

The particles observed by SEM images seem aggregated and crowded, consisting of

primary ZnO-Np Figure 4.7 (e). The primary nano crystallites are combined to form a larger particle (secondary particles). The secondary particles are formed as the results of aggregation of the primary crystallites or by fusion of one primary crystalline into another. This made it not possible for it to be conjugated with the synthesized Pc (Suber, 2018).



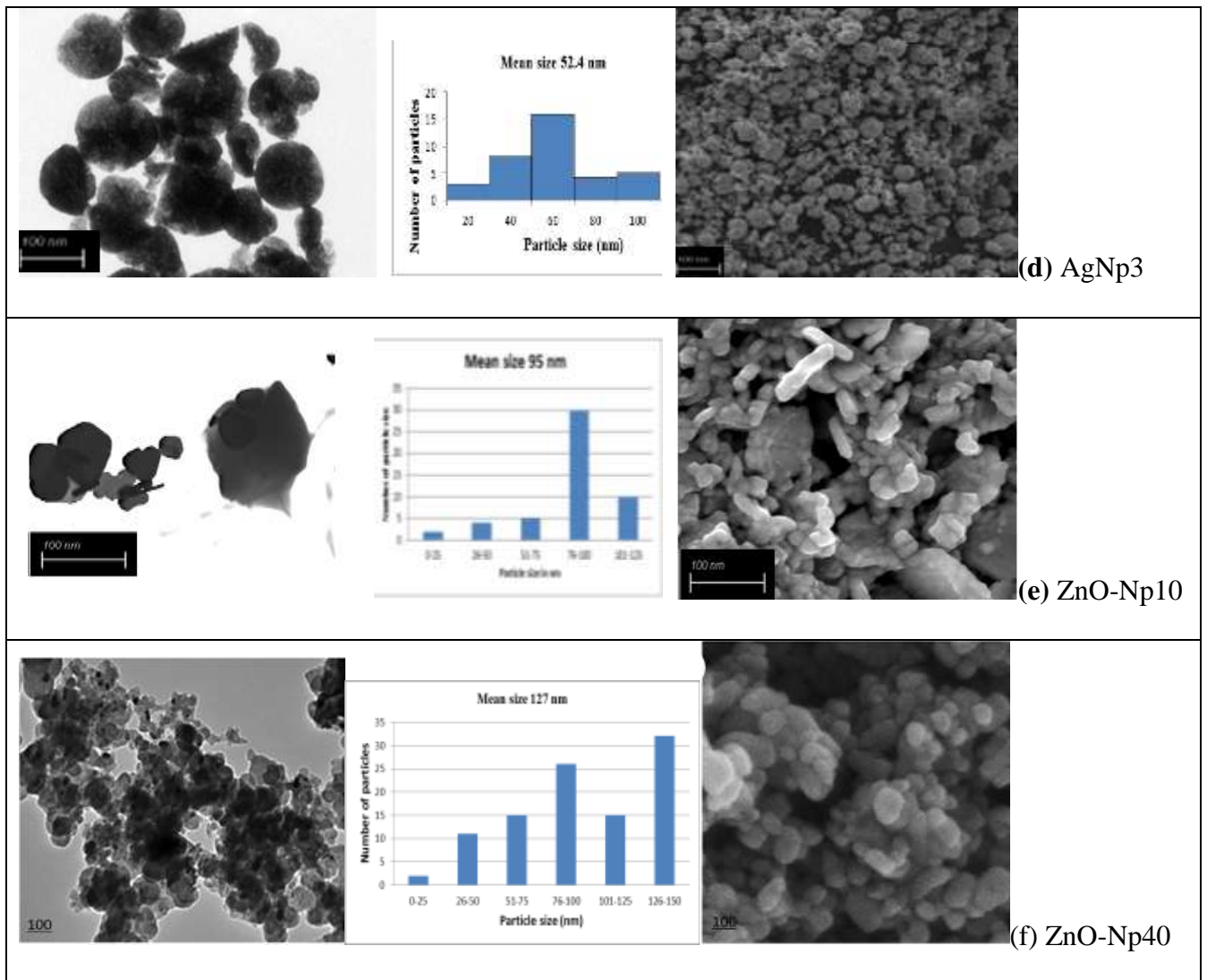


Figure 4.7: TEM images of AgNps of various size ranges (a) 9.94 ± 1.34 nm; (b) 18.45 ± 2.93 ; (c) 34.96 ± 6.34 ; (d) 52.40 ± 2.64 nm; For ZnO-Nps (e) 95 ± 6.75 nm and (f) 127 ± 11.75 . For each image, the corresponding SEM micrograph is shown. The histograms show the range of particle size distribution for each.

4.2.4 UV-Vis spectroscopy of AgNps and ZnO-Nps

The UV-Vis spectrums of the AgNps are shown in Figure 4.8. The samples prepared of the AgNps showed characteristic surface plasmon (De Matteis *et al.*, 2018). The AgNps

of mean 9.94 ± 1.34 nm, 18.45 ± 2.93 nm, 34.96 ± 6.34 nm and 52.40 ± 2.64 nm had a narrow band with maximum occurring at 394 nm, 398 nm, 406 nm and 411 nm respectively. The AgNps of mean size 58.5 ± 5.83 nm had a wider band with a maximum at 420 nm. De Matteis *et al.* (2018) revealed that spherical AgNps had a maximum absorption band at around 400 nm with a blue or red shift when particle size decreases or increases, respectively. For this reason, 9.94 ± 1.34 nm AgNps (AgNp0.5) had a plasmon band, which is blue shifted when compared to that of 58.5 ± 5.83 nm AgNps (AgNp4). The width of absorption plasmon is related to the size distribution of the nanoparticles.

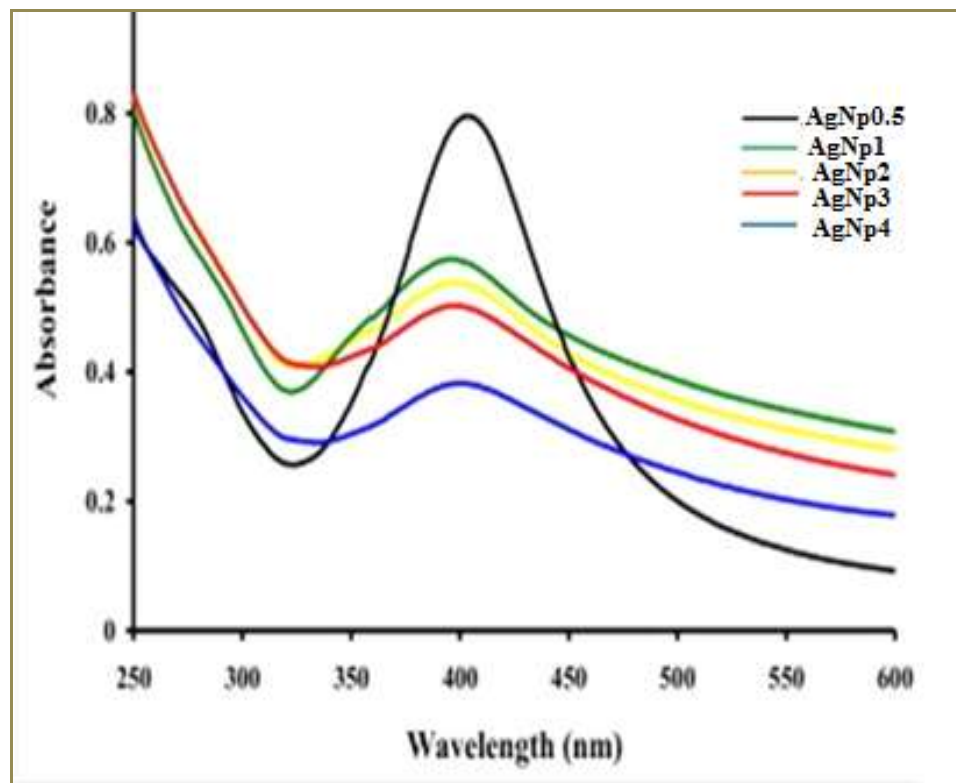


Figure 4.8: UV-Vis spectra of AgNps under different concentration labeled AgNp0.5 AgNp1, AgNp2, AgNp3, and AgNp4

Reduction of zinc ions to ZnO-Nps and its formation were confirmed by the use of UV-Vis spectrum obtained in the range of 200-700 nm. The spectrum showed a distinct peak at around 358 nm as given in Figure 4.9. The formation of ZnO-Nps causes excitation of from ground state to excited state indicating they are sensitive in UV-Vis region. These results were comparable to that done by Ullangula and Ganganaguta (2016).

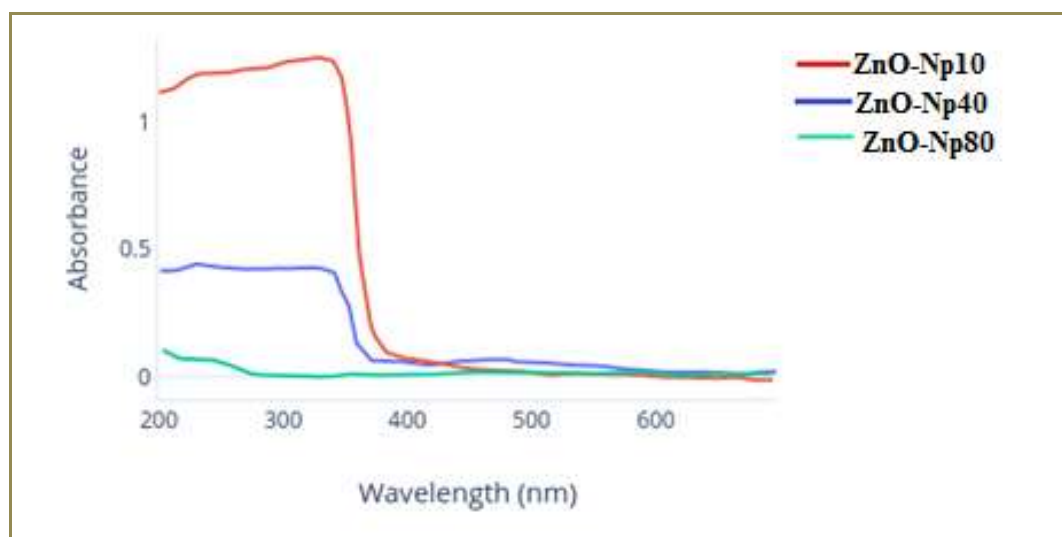


Figure 4.9: UV-Vis spectra of ZnO-Np formed from solution ZnO-Np10, ZnO-Np40 and ZnO-Np80

4.3 Conjugation of AgNps to Pcs

Pc **6** and **10** were covalently linked to AgNps due to an amide coupling agent dicyclohexylcarbodiimide (DCC) to form conjugated Pcs. AgNps have affinity to sulphur and nitrogen. This makes it possible to couple Pcs with compounds having nitrogen and sulphur atoms. For Pc **10** conjugation to AgNps is likely due to Ag-S bonding that occurs due to ethylsulfonyl functional group that has sulphur at the periphery of the Pc ring

Figure 4.10. While Pc **6** conjugation may be due to interaction of Pc metal center with AgNps *via* donating charge to the silver surface (Masilela, *et al.*, 2013).

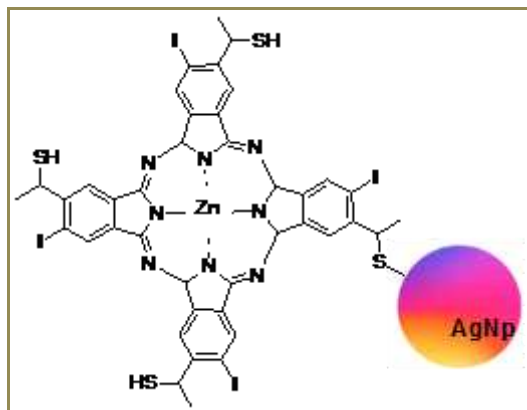


Figure 4.10: Representation of conjugation of Pc to AgNp

On conjugating Pcs with AgNps complexes, TEM images showed ordered arrangement of particles with aggregation forming particularly for conjugated Pc **10** suggesting conjugation has taken place (Figures 4.11)

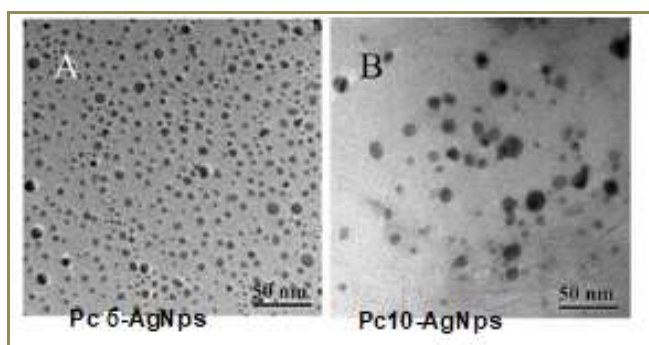


Figure 4.11: TEM images of (A) Pc 6-AgNps and (b) Pc 10-AgNps

The coupling of nanoparticles and Pcs was also confirmed using FTIR spectra (Figure 4.12). The spectra for Pc **10** show the presence of the S-H stretching band at around 2480 cm^{-1} for the free Pc which shifts to 2260 cm^{-1} in the conjugated Pc **10** with AgNps. The conjugation was further proved by sharp peaks corresponding to the N-H stretching band

around 3250 cm^{-1} decreasing in size for the conjugated Pc indicating some activities has taken place during bonding with AgNps.

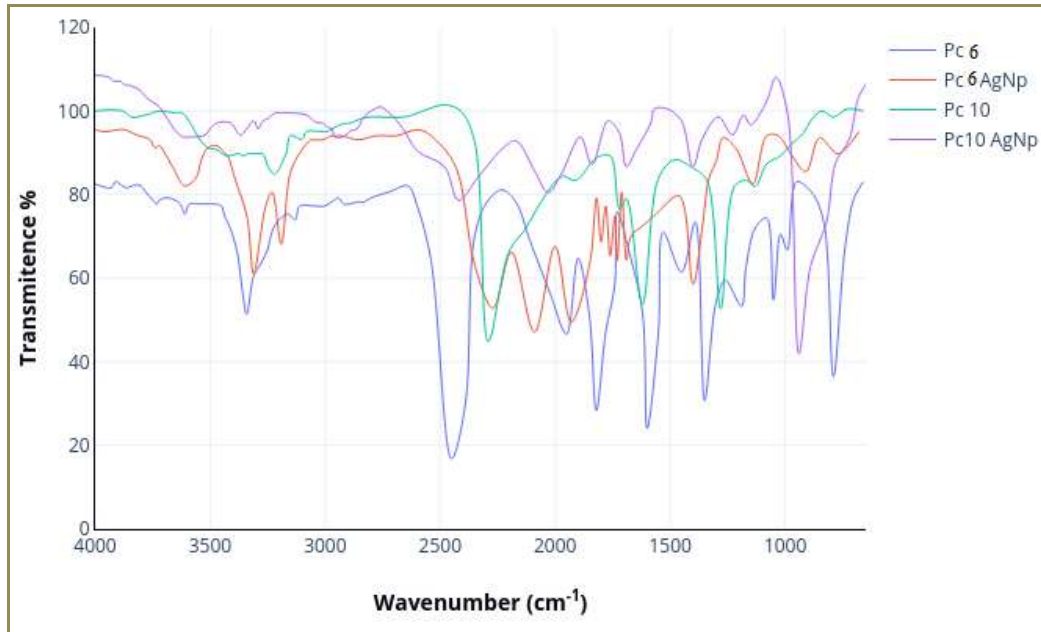


Figure 4.12: Infrared spectra of Pc 6, Pc 10 and their respective AgNps conjugates

The absorption spectra of the Pc 6 and Pc 10 together with their conjugates are shown in Figure 4.13. Pc-AgNps conjugates shows broadening of the B- and Q-band absorption. This is because of tight packing of AgNps and Pcs that tend to make them aggregate as evidenced by TEM images (Khoza and Nyokong, 2015). Apart from broadening of peaks, there is blue shift of band for Pc 6-AgNps conjugate. This shifting of peak is due to the electron deficiency brought about by the Pc 6 and AgNps coupling (Nombona, *et al.*, 2012).

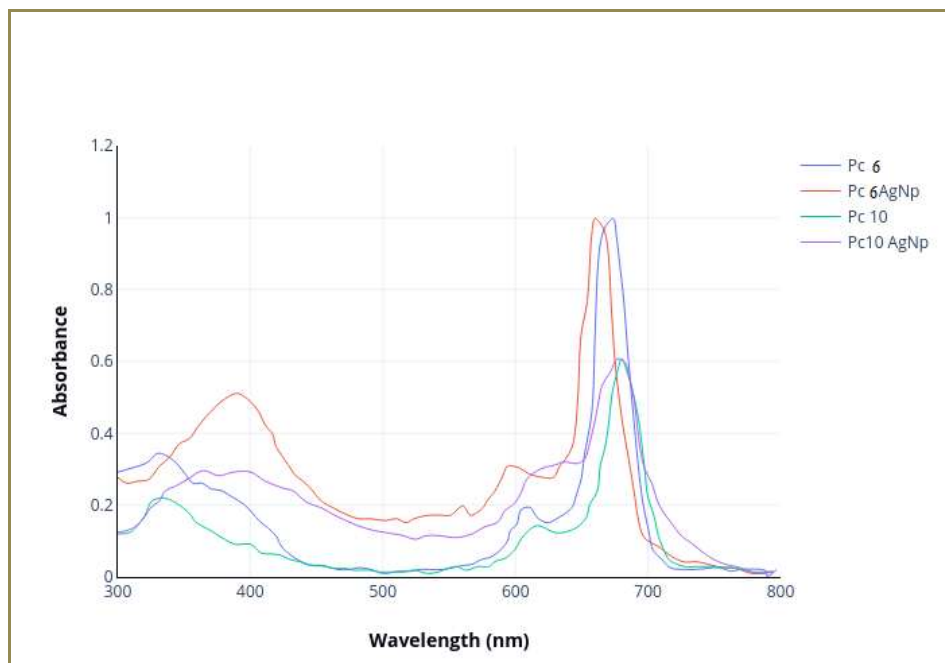


Figure 4.13: Absorption spectra of Pc 6, Pc 10 and their respective AgNps conjugates

4.4 Photochemical analysis

4.4.1 Fluorescence quantum yield Pcs

The Pcs fluorescence and singlet oxygen quantum yield were determined using UV-Vis spectrometer with as ZnPc a reference ($\Phi_F=0.17$ and $\Phi_{\Delta}=0.56$). The Φ_F determined was between 0.12-0.24 (Table 4.10). The values were higher when compared to that obtained by Rapulenyane, (2013) with Φ_F ranging between 0.1 to 0.12. The Φ_F of the substituted Pc in solvent solutions decreased from 0.24 for the ZnPc reference to 0.12 for the conjugated Pc (Table 4.10). Lower Φ_F values are expected for substituted and conjugated compounds. For example Pc **10** has the lowest value of 0.12 caused by the heavy Ag atom effect that result to an enhanced rate of intersystem crossing to the T1 state and hence reduces the fluorescence intensity. The results are consistent with those reported

previously for Pcs complexes conjugated to Pt nanoparticles, Φ_F decreased from 0.23 for ZnPc to 0.14 (Bulgakov *et al.*, 2012).

4.4.2 Singlet oxygen quantum yield of the phthalocyanine (Pcs)

The $\Phi\Delta$ was determined by the absorption decay DPBF measured at 417 nm. The concentration of solutions used to determine $\Phi\Delta$ and photobleaching studies were made to be in order 10^{-6} mol dm^{-3} , where aggregation is less. Spectral changes occurred during the photolysis of Pc **10** in the presence of DPBF for the determination of $\Phi\Delta$ (Figure 4.14). Changes in the spectra of DPBF could be seen without spectral changes happening for the Pc **10**. This proved Pcs does not degrade during the process for $^1\text{O}_2$ generation. Figure 6.33, 6.34 and 6.35 (Appendix 1) indicates the spectral changes that occurred for Pc 5, Pc 10-AgNps and Pc 5-AgNp conjugates respectively.

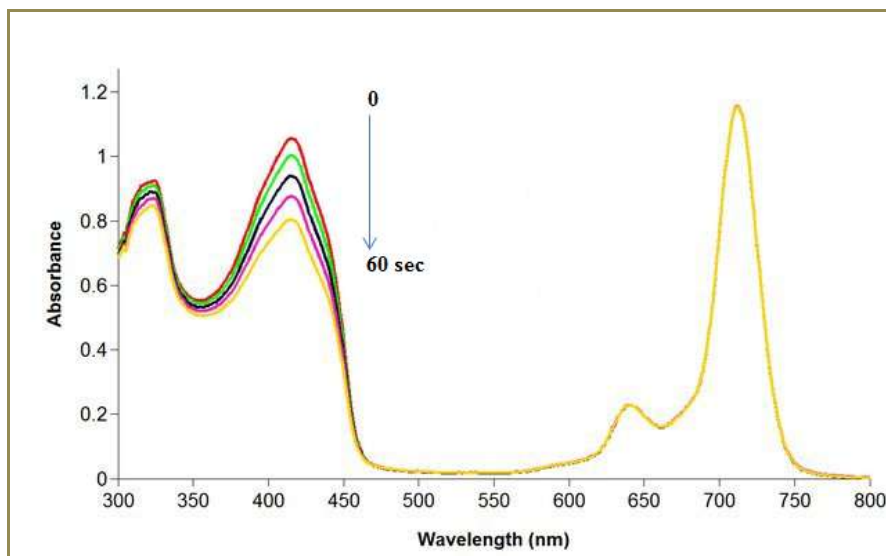


Figure 4.14: Absorption spectra for generation of singlet oxygen using DPBF singlet quencher between 0 and the 60 seconds

The $\Phi\Delta$ generation of ZnPc, Pc **6**, Pc **10** and conjugated Pcs are shown in Table 4.10. The values ranged from 0.51 to 0.75. The Pc **6** and conjugated Pc **6** gave $\Phi\Delta$ of 0.53 and 0.56 respectively. Pc **10** and conjugated Pc **10** with AgNp gave the highest $\Phi\Delta$ of 0.63 and 0.75 respectively. Pc **10** had the highest quantum yield as compared to Pc **6** which was attributed to the attached sulfonyl functional group that might have increased the solubility.

Table 4.10: Photochemical parameters for synthesized Pcs in DMSO

Compound	$\lambda_{\text{max}}^{\text{abs}}$ nm	ΦF	$\Phi\Delta$
ZnPc	672	0.240±0.007 ^b	0.510±0.012 ^c
Pc 6	680	0.140±0.009 ^a	0.530±0.016 ^c
Pc 10	698	0.130±0.008 ^a	0.630±0.016 ^d
Pc 6 conjugated with Ag-np	680	0.130±0.010 ^a	0.560±0.017 ^c
Pc 10 conjugated with Ag-np	698	0.120±0.009 ^a	0.750±0.023 ^e
P value < 0.05			

Means in the same column within groups not followed by the same letter value of superscript are significantly different; (P<0.05)

Other studies done had shown attachment of certain functional groups improved photochemical properties of the Pcs such as increased production of $\Phi\Delta$ and intersystem crossing (Rapulenyane, 2013). In addition, coupling of Pcs to metal nanoparticle improved permeability and reduced aggregation in solution. Aggregation of the Pcs in solution results to decreased photochemical activity due to radiationless decay of excited states. The $\Phi\Delta$ of Pcs with AgNps conjugates were significantly enhanced due to the presence of the silver atoms. The Ag atoms help to increase the energy transfer to the triplet state by enhancing spin-orbit coupling via the heavy atom effect, this increases the

potential of Pcs to be used as photosensitizer possible (Manieri *et al.*, 2015). The $\Phi\Delta$ values for the complexes synthesized in this work are within the range of $\Phi\Delta$ for complexes currently in use of antibacterial (Manieri *et al.*, 2015).

4.5 Antibacterial analysis

4.5.1 Antibacterial activities of silver nanoparticles (AgNps) using disc diffusion test

Effects of different particle sizes labeled AgNp0.5, AgNp1, AgNp2, AgNp3 and AgNp4 on bacteria were determined. The zones of inhibitions for size dependent AgNps against the selected strains *S. typhi*, *B. subtilis*, *S. aureus* and *E. coli* are given in Table 4.11. Ciprofloxacin was used as the positive control. Figure 4.15 is part of the images showing zones of inhibition of AgNps of different particle size against *B. subtilis*.

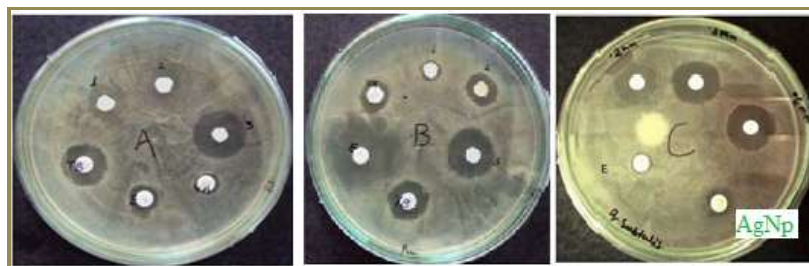


Figure 4.15: Zones of inhibition for AgNps with different particles size against *B. subtilis* done in triplicate

The AgNps with different particles size showed significantly lower value of zone of inhibitions as compared to the positive control ciprofloxacin ($P < 0.05$). Small AgNps particle size with mean value 9.94 nm showed significantly high zone of inhibition as compared to big particle size with mean value 58.50 nm against *S. typhi*, *B. subtilis*, *S.*

aureus and *E. coli* ($P < 0.05$). In conclusion AgNps of small sizes had high zone of inhibition against all the tested bacteria strains as compared to AgNps with large particle sizes. Metal nanoparticles with small mean size have increased surface area and also due to their small particle size they are able to penetrate the cell membrane of bacteria easily as compared to the large particles (Nzekwe *et al.*, 2016). The results are comparable to that obtained by El-Kheshen and El-Rab (2012) with a zone of inhibition ranging between 18 and 25 mm for *S. aureus*. However the zone of inhibition of *E. coli* were above that obtained by Khatoun and the group with average value of 6 mm (Khatoun *et al.*, 2011).

Table 4.11: Mean antibacterial activities of size dependent silver nanoparticles (AgNps) against strains of bacteria

Microbes	Zone of inhibition in millimetres				
	<i>Bacillus subtilis</i>	<i>Escherichia coli</i>	<i>Salmonella typhi</i>	<i>Staphylococcus aureus</i>	
AgNP size (nm)	9.94	17.00 ± 0.20 ^e	10.00 ± 0.30 ^e	13.50 ± 0.20 ^c	21.00 ± 0.10 ^f
	18.45	13.50 ± 0.30 ^d	9.00 ± 0.10 ^c	9.50 ± 0.50 ^b	16.50 ± 0.35 ^e
	34.96	12.20 ± 0.16 ^c	7.60 ± 0.20 ^b	8.80 ± 0.25 ^b	14.70 ± 0.10 ^d
	52.40	11.00 ± 0.30 ^b	7.50 ± 0.35 ^b	-	13.00 ± 0.20 ^c
	58.50	10.30 ± 0.24 ^b	7.00 ± 0.15 ^b	-	11.40 ± 0.35 ^b
Ciprofloxacin (30 µg/disc)	39.00 ± 0.15 ^a	24.00 ± 0.30 ^a	28.00 ± 0.30 ^a	45.00 ± 0.65 ^a	
DMSO	-	-	-	-	

Means in the same column within groups not followed by the same letter value of superscript are significantly different; (P<0.05)

“—” indicates no significant inhibitory effect (< 6 mm)

4.5.2 Antibacterial activities of ZnPc, Pc 6, Pc 10 and their silver conjugates against selected bacterial strains

The antibacterial activities of Pcs against the tested strains of bacteria's were carried by means of disc diffusion method by determining zones of inhibition in triplicate. Figure 4.16 shows zones of inhibition for Pc 6 and 10 against *S. typhi*, *E. coli* and *B. subtilis* respectively. Pc 10 had a higher zone of inhibition as compared to Pc 6 ($P < 0.05$).

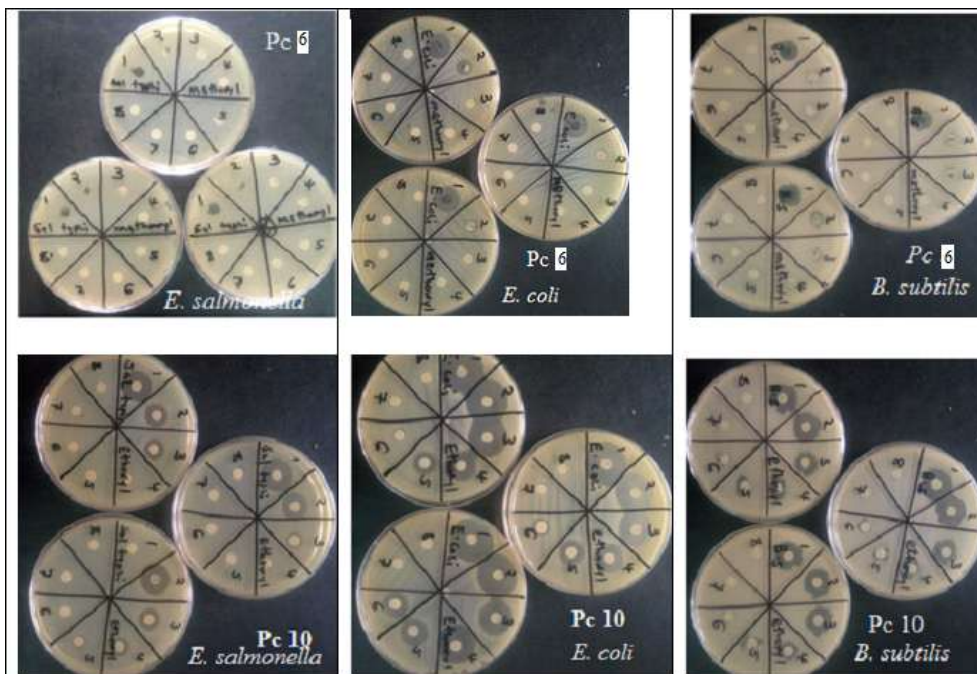


Figure 4.16: Zones of inhibition of inhibition for Pc 6 and 10 against *S. typhi*, *E. coli* and *B. subtilis*

The mean antibacterial activity of the ZnPc, Pc 10 and their conjugates against *S. typhi*, *B. subtilis*, *S. aureus* and *E. coli* are given in Table 4.12 It is notable that the antibacterial activities of the test compound against the tested microbes increased with the increase in

concentration ($\mu\text{g/ml}$) of the Pcs with the exception of *S. typhi* and *E. coli* that showed limited activities in ZnPc and Pc **6**. This therefore, implied that *S. typhi* and *E. coli* were resistant to ZnPc and Pc **6** probably due to the fact that the two are gram-negative bacteria. Gram-negative is made up of an extra layer of phospholipid as compared to gram-positive bacteria (Cieplik *et al.*, 2014; Ruiz-gonzález *et al.*, 2015). The phospholipid layer protects gram-negative bacteria against any foreign materials from outside, making it impermeable to a number of antibacterial (Manieri *et al.*, 2015). For *B. subtilis* and *S. aureus* they are susceptible due to the fact that they are gram-positive and they do not have the phospholipid layer.

The Pc **10** and its silver conjugate exhibited higher zones of inhibition as compared to other Pcs against the bacteria strains. This may be attributed to the attached sulfonyl functional group that makes these Pcs to release more singlet oxygen which causes oxidation of the bacterial cell wall both for gram-negative and -positive bacteria thus improving efficiency to inhibit the bacterial multiplication (Abrahamse and Hamblin, 2016a).

The sensitivity of Pcs against bacteria was significantly enhanced when they were conjugated with AgNps against all strains of bacteria Table 4.12. This is because the generation of singlet oxygen yield was significantly increased for the conjugated Pc (Pc **6** conjugated and Pc **10** conjugated $\Phi\Delta=0.56$ and 0.75 respectively). The enhanced antibacterial effect of the conjugated Pc may also be as a result increased synergistic factor brought about by coupling AgNps to the Pc. Studies done by Asharani, *et al.*

(2009) showed that Ag^+ ions inhibit the phosphate uptake and exchange in bacteria hence affecting its metabolism.

Table 4.12: Antibacterial activities of the synthesized Pcs and their silver conjugate against selected bacteria strains

	Microbes	Mean of inhibition zone diameters (mm)							
Con ($\mu\text{g/ml}$)		500	250	125	62.50	31.25	15.63	7.81	3.91
ZnPc	<i>E. coli</i>	10 \pm 0.12 ^I	-	-	-	-	-	-	-
	<i>S. aureus</i>	12 \pm 0.02 ^{aH}	7 \pm 0.02 ^{bj}	-	-	-	-	-	-
	<i>B. subtilis</i>	15 \pm 0.09 ^{aG}	13 \pm 0.47 ^{bG}	11 \pm 0.67 ^{cH}	7 \pm 0.19 ^{dl}	-	-	-	-
	<i>S. typhi</i>	-	-	-	-	-	-	-	-
Pc 6	<i>E. coli</i>	14 \pm 0.72 ^{aG}	7 \pm 0.62 ^{bj}	-	-	-	-	-	-
	<i>S. aureus</i>	24 \pm 0.26 ^{aE}	22 \pm 0.18 ^{bF}	18 \pm 0.26 ^{cG}	15 \pm 0.14 ^{dG}	11 \pm 0.18 ^{eI}	8 \pm 0.09 ^{fJ}	-	-
	<i>B. subtilis</i>	12 \pm 0.08 ^{aH}	9 \pm 0.26 ^{bi}	8 \pm 0.26 ^{bi}	-	-	-	-	-
	<i>S. typhi</i>	-	-	-	-	-	-	-	-
PC 10	<i>E. coli</i>	25 \pm 0.06 ^{aE}	23 \pm 0.28 ^{bE}	20 \pm 0.06 ^{cF}	18 \pm 0.05 ^{dF}	14 \pm 0.01 ^{eH}	12 \pm 0.64 ^{fi}	-	-
	<i>S. aureus</i>	33 \pm 0.26 ^{aB}	31 \pm 0.10 ^{bC}	29 \pm 0.80 ^{cD}	28 \pm 0.15 ^{cD}	26 \pm 0.05 ^{dE}	25 \pm 0.14 ^{dF}	17 \pm 0.05 ^{eF}	12 \pm 0.05 ^{fG}
	<i>B. subtilis</i>	33 \pm 0.14 ^{aB}	30 \pm 0.93 ^{bC}	26 \pm 0.92 ^{cE}	26 \pm 0.08 ^{cE}	24 \pm 0.05 ^{dF}	18 \pm 0.09 ^{eG}	15 \pm 0.04 ^{fG}	9 \pm 0.03 ^{gH}
	<i>S. typhi</i>	24 \pm 0.82 ^{aE}	24 \pm 0.19 ^{aE}	18 \pm 0.03 ^{bG}	15 \pm 0.13 ^{cG}	11 \pm 0.13 ^{dI}	7 \pm 0.04 ^{eJ}	-	-
Pc 6 -AgNp	<i>E. coli</i>	17 \pm 0.22 ^{aF}	11 \pm 0.12 ^{bH}	8 \pm 0.35 ^{cI}	8 \pm 0.04 ^{cI}	-	-	-	-
	<i>S. aureus</i>	27 \pm 0.12 ^{aD}	23 \pm 0.19 ^{bE}	20 \pm 0.26 ^{cF}	17 \pm 0.13 ^{dF}	13 \pm 0.28 ^{eH}	7 \pm 0.08 ^{fJ}	-	-
	<i>B. subtilis</i>	15 \pm 0.09 ^{aG}	13 \pm 0.97 ^{bG}	11 \pm 0.07 ^{cH}	7 \pm 0.19 ^{dI}	-	-	-	-
	<i>S. typhi</i>	14 \pm 0.85 ^{aG}	13 \pm 0.23 ^{bG}	10 \pm 0.12 ^{cH}	7 \pm 0.10 ^{dI}	-	-	-	-
Pc 10 -AgNp	<i>E. coli</i>	31 \pm 0.18 ^{aC}	28 \pm 0.22 ^{bD}	28 \pm 0.06 ^{bD}	26 \pm 0.05 ^{cE}	18 \pm 0.07 ^{dG}	14 \pm 0.12 ^{eH}	12 \pm 0.11 ^{fH}	9 \pm 0.13 ^{gH}
	<i>S. aureus</i>	36 \pm 0.14 ^{aA}	35 \pm 0.64 ^{aB}	33 \pm 0.44 ^{bB}	33 \pm 0.14 ^{bB}	32 \pm 0.04 ^{cC}	27 \pm 0.05 ^{dE}	24 \pm 0.05 ^{eE}	19 \pm 0.15 ^{fE}
	<i>B. subtilis</i>	37 \pm 0.74 ^{aA}	35 \pm 0.39 ^{bB}	34 \pm 0.14 ^{bB}	32 \pm 0.65 ^{cC}	32 \pm 0.14 ^{cC}	30 \pm 0.19 ^{dD}	23 \pm 0.07 ^{eE}	16 \pm 0.13 ^{fF}
	<i>S. typhi</i>	28 \pm 0.13 ^{aD}	23 \pm 0.10 ^{bE}	18 \pm 0.13 ^{cG}	13 \pm 0.12 ^{dH}	10 \pm 0.05 ^{eI}	8 \pm 0.14 ^{fJ}	7 \pm 0.25 ^{fI}	7 \pm 0.21 ^{fI}

Ciprofloxacin + control 30 µg/mL	<i>E. coli</i>	31±0.20 ^C	31±0.20 ^C	31±0.20 ^C	31±0.20 ^C	31±0.20 ^C	31±0.20 ^C	31±0.20 ^C	31±0.20 ^C
	<i>S. aureus</i>	37±0.11 ^A	37±0.11 ^A	37±0.11 ^A	37±0.11 ^A	37±0.11 ^A	37±0.11 ^A	37±0.11 ^A	37±0.11 ^A
	<i>B. subtilis</i>	34±0.64 ^B	34±0.64 ^B	34±0.64 ^B	34±0.64 ^B	34±0.64 ^B	34±0.64 ^B	34±0.64 ^B	34±0.64 ^B
	<i>S. typhi</i>	29±0.06 ^D	29±0.06 ^D	29±0.06 ^D	29±0.06 ^D	29±0.06 ^D	29±0.06 ^D	29±0.06 ^D	29±0.06 ^D
DMSO	All microbes	-	-	-	-	-	-	-	-

“—” indicates no significant inhibitory effect (< 6 mm)

Means in the same row within groups not followed by the same small letter of superscript are significantly

Means in the same column within groups not followed by the same capital letter value of superscript are significantly different;
(P<0.05).

There were significance increase in zone of inhibition for synthesized Pc against the selected strain of bacteria under irradiation with electric Quartz line lamp (GE EXR 300 W 82 V) after 18 hours inhibition at 30 °C (Figure 4.17) It is notable that the antibacterial activities of the test compound against the tested microbes increased with the increase in concentration ($\mu\text{g/ml}$) of the Pcs during irradiation with light.

From the data, the zone of inhibition of Pc **10** and its conjugates in presence of light are higher than that of Pc **6** and its conjugates. These differences indicate the crucial effect of irradiation on the inhibition of bacteria by photosensitizer. A large zone of inhibition of Pc **10** and its conjugates in light can be explained by the attached ethylsulfonyl functional group which is an electron withdrawing group. From the results obtain in this work, Pc **10** and its conjugates exhibited a red shifted Q band compared to ZnPc and Pc **6** in all solvents, because of electron withdrawing nature of sulfonyl groups in the compound (Ogata *et al.*, 2003). This resulted to it generating more singlet oxygen when irradiated in light as compared to other Pcs. This observation is in agreement with Vallemolinales *et al.* (2015) studies who worked on attaching a carboxylic functional group on Pc to form tetracarboxiphthalocyanine against *E. coli*, *S. aureus* and *Klebsiella pneumoniae*. Their result showed a high zone of inhibition > 80% against the tested bacteria in presence of light. They attributed the increased sensitivity of this Pc to attached electron withdrawing carboxyl functional group in macrocyclic ring of the Pc structure. This increased photochemical properties of the Pc increasing generation of singlet oxygen (Vallemolinales *et al.*, 2015).

Even in the dark, both Pc displayed antibacterial activity; this may be explained by the interaction between the ionic bacterial membrane and the cationic Pcs. The cationic Pcs work by competing with positively charged ions like Ca^{2+} and Mg^{2+} ions found on the surface of microbes that helps to stabilize the cell membrane (Liu *et al.*, 2015). These cationic ions Pcs deteriorate the outer cell membrane of the microbes allowing the intake of Pc that will incapacitate the bacteria metabolic activities (Liu *et al.*, 2015).

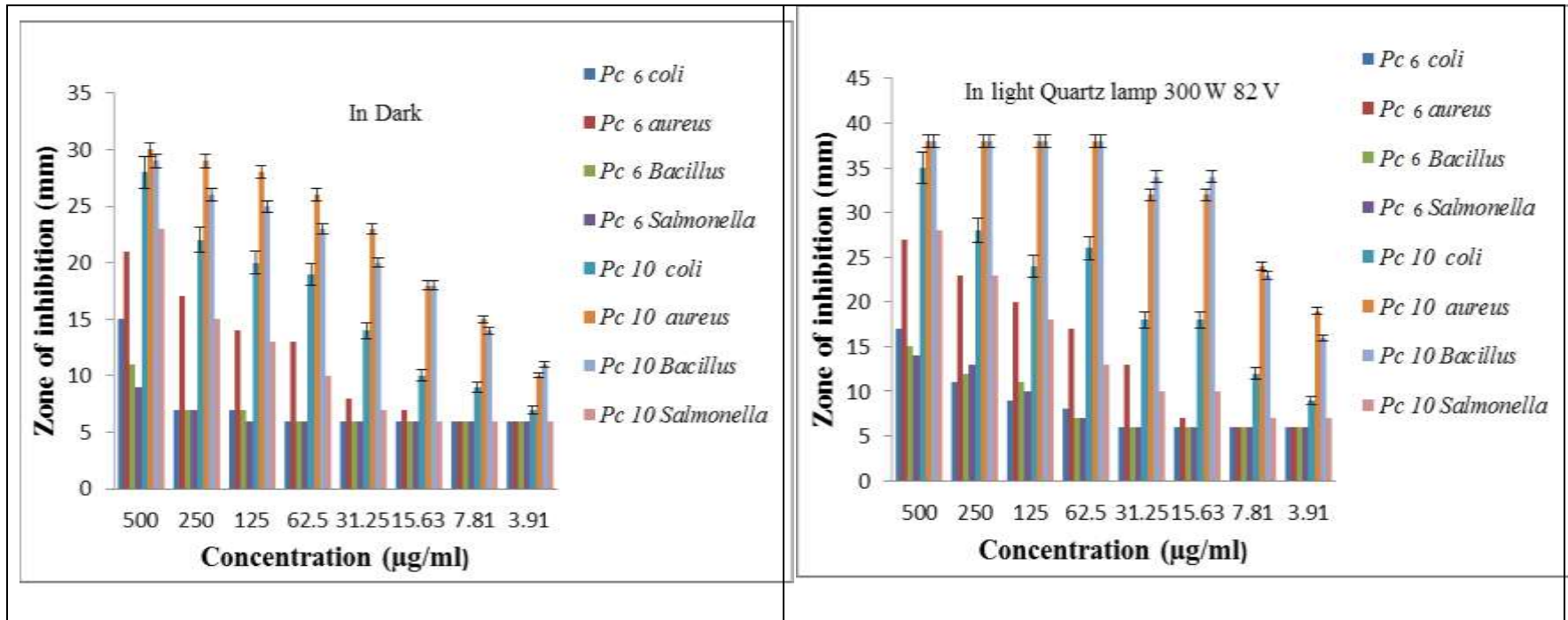


Figure 4.17: Zone of inhibition under different concentration of conjugated Pc 6 and Pc 10 against *E. coli*, *S. aureus*, *B. subtilis* and *S. typhi* in the dark and irradiated in light using general electric quartz line lamp (GE EXR 300 W 82 V) after 18 hours inhibition at 30 °C.

4.5.3 Bactericidal and inhibitory minimum concentration of Pcs

The MIC and MBC for standard, ZnPc, Pc 6, Pc 10 and respective conjugate in different concentration against the bacteria's obtained using broth microdilution are shown in Table 4.13.

Table 4.13: Minimum inhibitory concentration (MIC) and minimum bactericidal concentration (MBC) of the Pcs

Conc (µg/ml)		MIC and MBC								
		500	250	125	62.50	31.25	15.63	7.81	3.91	1.96
ZnPc	<i>E. coli</i>	+	+	+	+	+	+	+	+	+
	<i>S. aureus</i>	+	+	+	+	+	+	+	+	+
	<i>B. subtilis</i>	-	+	+	+	+	+	+	+	+
	<i>S. typhi</i>	+	+	+	+	+	+	+	+	+
Pc 6	<i>E. coli</i>	-	+	+	+	+	+	+	+	+
	<i>S. aureus</i>	-	-	-	-	-	+	+	+	+
	<i>B. subtilis</i>	-	+	+	+	+	+	+	+	+
	<i>S. typhi</i>	-	+	+	+	+	+	+	+	+
Pc 10	<i>E. coli</i>	-	-	-	-	-	-	+	+	+
	<i>S. aureus</i>	-	-	-	-	-	-	-	+	+
	<i>B. subtilis</i>	-	-	-	-	-	-	-	+	+
	<i>S. typhi</i>	-	-	-	-	-	+	+	+	+
Pc 6 conjugated to AgNp	<i>E. coli</i>	-	-	+	+	+	+	+	+	+
	<i>S. aureus</i>	-	-	-	-	-	+	+	+	+
	<i>B. subtilis</i>	-	-	-	+	+	+	+	+	+
	<i>S. typhi</i>	-	-	+	+	+	+	+	+	+
Pc 10 conjugated to AgNp	<i>E. coli</i>	-	-	-	-	-	-	-	+	+
	<i>S. aureus</i>	-	-	-	-	-	-	-	-	+
	<i>B. subtilis</i>	-	-	-	-	-	-	-	-	+
	<i>S. typhi</i>	-	-	-	-	-	+	+	+	+
Ciprofloxacin	<i>E. coli</i>	-	-	-	-	-	-	+	+	+

	<i>S. aureus</i>	-	-	-	-	-	-	-	+	+
	<i>B. subtilis</i>	-	-	-	-	-	-	-	+	+
	<i>S. typhi</i>	-	-	-	-	-	+	+	+	+

NB: “+” indicates turbidity, and “-” indicates inhibition of growth

The MIC and MBC for Pc **6** were found to be (values indicated by blue) 250, 15.63, 250 and 250 µg/ml for *E. coli*, *S. aureus*, *B. subtilis* and *S. typhi* respectively. For Pc **10** it had MIC and MBC of 7.81, 3.91, 3.91 and 15.63 µg/ml for *E. coli*, *S. aureus*, *B. subtilis* and *S. typhi* respectively. We can deduce from the data, that Pc **10** was more effective with lower MIC and MBC concentration as compared to Pc **6**. There was no significant difference between MIC and MBC of Pc **10** and the positive control ciprofloxacin confirming that PC **10** was equally effective.

When the Pc **6** and Pc **10** were conjugated to AgNps their MIC and MBC were greatly enhanced. The MIC and MBC for conjugated Pc **6** were 62.5, 15.63, 62.5 and 125 µg/ml for *E. coli*, *S. aureus*, *B. subtilis* and *S. typhi* respectively. The MIC and MBC for Pc **10** were 3.91, 1.96, 1.96 and 15.63 µg/ml for *E. coli*, *S. aureus*, *B. subtilis* and *S. typhi* respectively. These results are comparable with those obtained by Hajra *et al* (2018) for irradiated zinc Pc with MICs values ranging from 1 to 4 µg/ml for *E. coli*, *S. aureus* and *B. subtilis*.

4.5.6 Cytotoxicity test

Cytotoxicity evaluation was done using the MTT cell viability test. This test used reduction of tetrazolium salt (yellow) to measure cellular metabolic activity in order to determine cell viability. The cytotoxicity of the two compounds (compound **6** and **10** conjugated to AgNps) were assessed on the Vero cells. Figure 4.18 and 4.19 show Vero cells before and after mixing with Pc **6** and **10**. Viable cells turned MTT to a purple colored formazan at absorbance at 590 nm. This is due to active metabolism of live cells. The cytotoxicity response of the Pcs compound was linear and dose-dependent Figure 4.20. The concentration associated with 50% cytotoxicity was calculated by linear regression analysis and was found to be 600 $\mu\text{g/ml}$ for compound **6** while compound **10** was found to be above 1000 $\mu\text{g/ml}$. The tested Pc **5** and **10** had no toxicity on Vero cells as their MIC values were lower than the cytotoxicity concentration (CC 50%). These results were in agreement with that done by Hajra *et al* (2018) for zinc Pc done using HEp-2 cells.

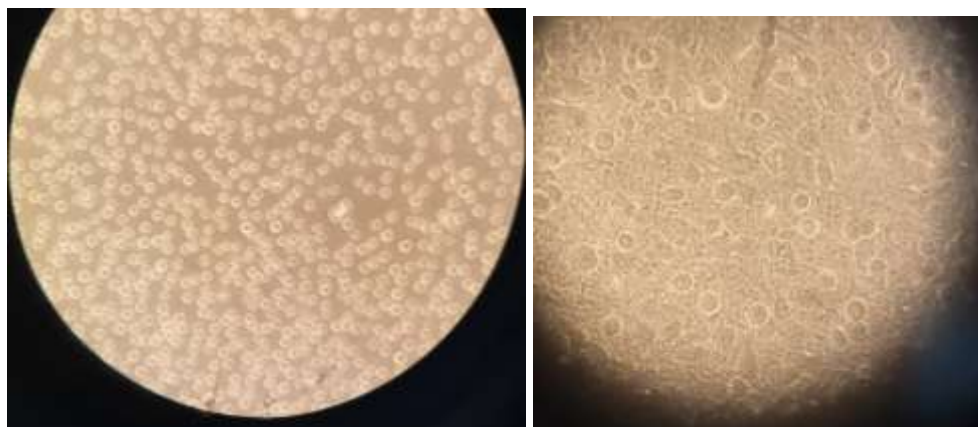


Figure 4.18: Image of Vero cell before and after being subjected to Pc **6** respectively

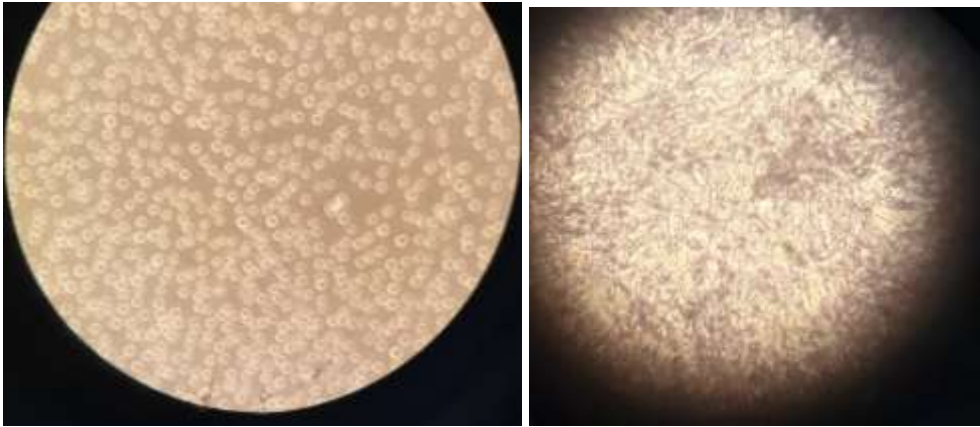


Figure 4.19: Image of Vero cell before and after being subjected to Pc 10 respectively

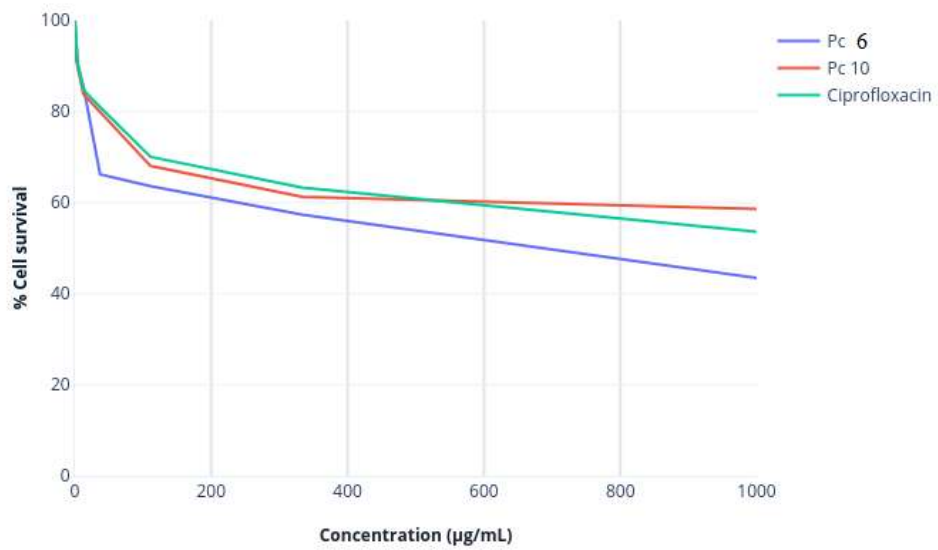


Figure 4.20: Line graph of % cytotoxicity against concentration of compound 6 and 10 in µg/ml

CHAPTER FIVE

CONCLUSIONS AND RECOMMENDATIONS

5.1 Conclusions

Zinc Pc complexes with electron donating and withdrawing functional group were successfully synthesized starting with phthalimide as a precursor and subjected to cyclotetramerization to form Pc **6** and Pc **10** respectively. They were fully characterized and confirmed using FTIR, ¹HNMR, ¹³CNMR, XRD, HR-MS and UV-Vis. Pc **6** compound formed was a blue solid with a yield of 47 %, melting point of 350 °C and its crystal nature confirmed by XRD as β-form in nature with monoclinic structure. It had two absorption bands, 354-365 nm for B-band and 620-640 nm for Q band confirming the formation of Pc **5**.

Pc **10** was a green solid with a yield of 55.5%, melting point 327°C and crystal in nature confirmed by XRD as β-form in nature with monoclinic structure. The UV-Vis spectra of both Pcs indicated two major absorption bands at 345-365 nm for B- band and 680-689 nm bands for Q band in different solvent. This also confirmed the formation of Pc **10**. The photo-chemical properties of these complexes were investigated. Pc **6** and Pc **10** showed the ΦΔ values of 0.53 and 0.63 and ΦF value of 0.14 and 0.13 respectively. Pc **10** with electron withdrawing group had the highest ΦΔ of 0.63.

The Pc discussed in this work demonstrates its potential to be used as antibacterial against *S. typhi*, *B. subtilis*, *S. aureus* and *E. coli* as they showed properties of a good

photosensitizer. They produced reasonably high singlet oxygen yields, especially complex Pc **10**. For Pc **6** the highest zone of inhibition was exhibited in *S. aureus* with a value of 24 ± 0.26 indicating the bacteria were susceptible to the Pc **5**. The Pc **10** exhibited zone of inhibition $>23 \pm 0.12$ mm for all the strains making it more effective as compared to Pc **6**. All the strains of bacteria exhibited zone of inhibition to Pc **10** at the concentration > 15.63 $\mu\text{g/ml}$. This may be due to the attached sulfonyl functional group which is an electron withdrawing group that makes the Pc to release more singlet oxygen.

ZnO-Nps and AgNps were synthesized and characterized using XRD, TEM, FTIR and UV-Vis. The AgNps had absorption at around 400 nm with low concentration of AgNO_3 showing sharp peaks. The particles formed were crystalline, spherical shape and monodispersed. The formed AgNp were of size 9.94 nm, 18.45 nm, 34.96 nm, 52.40 nm and 58.50 nm. FTIR analysis revealed stabilization of glutathione as a capping agent to AgNps. UV-Vis spectra of ZnO-Np showed a distinct peak at 358 nm. TEM results indicated ZnO-Np had non uniform large grain size of size > 95 nm SEM showed aggregation of particles due to primary nanocrystallites combining to form larger secondary particles. This made it difficult to conjugate ZnO-Np with synthesized Pcs

Pc **6** and Pc **10** were successfully conjugated to AgNp and the photo-chemical properties of these Pcs conjugated investigated. Conjugated Pc **6** and Pc **10** to AgNp had $\Phi\Delta$ 0.56 and 0.75 respectively. This showed a significant increase in the produced singlet oxygen generation and as a result improved the antibacterial properties of this compound.

Conjugated Pc **10** had the best MIC and MBC with values 3.91, 1.96, 1.96 and 15.63 µg/ml for *E. coli*, *S. aureus*, *B. subtilis* and *S. typhi* respectively.

The tested compound has no toxicity in Vero cells (for Pc **10** CC50 >1000 and Pc **6** CC50 >600 µg/mL). The synthesized compounds could be considered a promising antibacterial agent and a valuable building block for further design of more potent biological activity against the resistant microbes.

5.2 Recommendations

- i. Phthalocyanine substituted with ethylsulfonyl as electron withdrawing group has potentials to be used in photodynamic antibacterial therapies
- ii. Silver nanoparticles of < 10 nm conjugated to phthalocyanine with electron withdrawing groups could be considered a promising antibacterial agent and an important building block for further derivatization to synthesis more potent compound against drug-resistant microbes.

5.3 Areas for further research

- i. Further studies to establish the safety profiles of the synthesized compounds in an animal model (in-vivo studies) are recommended.

- ii. There is need to determine the mechanism of this compound against the tested bacteria to determine how the singlet oxygen generated kills the microbes as it is not well understood

- iii. There is need to extend the studies to a range of other resistant strains of bacteria and viruses.

- iv. There is need to determine whether synthesizing ZnO-Nps <10 nm can conjugate with the synthesized Pc to increase its antibacterial activities

REFERENCES

- Azce meci, M., Nar, I., and Hamuryudan, E. (2014). Synthesis and electrochemical and spectroelectrochemical characterization of chloromanganese(III) phthalocyanines. *Turkish Journal of Chemistry*, 38(6), 1064–1072.
- Abrahamse, H., and Hamblin, M. R. (2016a). New photosensitizers for photodynamic therapy. *Biochemical Journal*, 473(4), 347–364.
- Abrahamse, H., and Hamblin, M. R. (2016b). *New photosensitizers for photodynamic therapy*. *New photosensitizers for photodynamic therapy*. (February, 2026).
- Agnihotri, S., Mukherji, S., and Mukherji, S. (2014). Size-controlled silver nanoparticles synthesized over the range 5-100 nm using the same protocol and their antibacterial efficacy. *Royal Society of Chemistry Advances*, 4(8), 3974–3983.
- Akhtar, K., Khan, S. A., and Khan, S. B. (2019). *Scanning Electron Microscopy: Principle and Applications in Nanomaterials*. *Scanning Electron Microscopy: Principle and Applications in Nanomaterials Characterization*.
- Amos-Tautua, B. M., Songca, S. P., and Oluwafemi, O. S. (2019). Application of porphyrins in antibacterial photodynamic therapy. *Journal ofMolecules*, 24(13).
- Andrew, F. P., Woods, J. A. O., Akinterinwa, A., Mukhtar, H., and Ndahi, J. A. (2016) Synthesis and Characterization of Some Metal (II) Complexes of Sulfadoxine *The Pharmaceutical and Chemical Journal*, 2016, 3 (2): 99-104
- Aneesh, P. M., Vanaja, K. A., and Jayaraj, M. K. (2007). Synthesis of ZnO nanoparticles by hydrothermal method. *Nanophotonic Materials IV*, 6639(November 2014), 66390J.
- Ashe, B. (2011). A Detail investigation to observe the effect of zinc oxide and Silver nanoparticles in biological system. (Master of Technology (Research)), National Institute Of Technology, National Institute Of Technology India.
- Asharani PV, Low Kah Mun G, Hande MP, and Valiyaveetil S. 2009. Cytotoxicity and Genotoxicity of Silver Nanoparticles in Human Cells. *ACS Nanomanufacturing* 3(2):279-290.
- Bahuguna, A., Khan, I., Bajpai, V. K., and Kang, S. C. (2017). MTT assay to evaluate the cytotoxic potential of a drug. *Journal of chemistry* 115–118.
- Baptista, P. V., McCusker, M. P., Carvalho, A., Ferreira, D. A., Mohan, N. M., Martins, M., and Fernandes, A. R. (2018). Nano-strategies to fight multidrug resistant bacteria-"A Battle of the Titans". *Frontiers in Microbiology*, 9(JUL), 1–26.

- Bata Péter. (2014). Catalytic applications of heterogeneous metal-phthalocyanine complexes. *The theses of Ph.D. dissertation*, (January, 2014), 1–220.
- Belfield, K.D., Corredor, C.C., and Morales, A.R. (2006). Synthesis and Characterization of New Fluorene-Based Singlet Oxygen Sensitizers. *Journal Fluorescence* 16, 105–110
- Berad, B. N., Bhiwagade, S. M., Ulhe, a G., Chemistry, P. G. T. D., Joytiba, M., Educational, F., and Tukadaji, R. (2012). Synthesis and structural studies of Glucosylimino-1,2,4,5-Tetrazine. *Pharma Chemical* 4(4), 1730–1734.
- Beveridge, T. J. (1999). *Minireview Structures of gram-negative cell walls and their derived membrane vesicles*. 181(16), 4725–4733.
- Bhatte, K.D., Deshmukh, K.M., Patil, Y.P., Sawant, D.N., Fujita, S., Arai, M., and Bhanage, B.M. (2012). Synthesis of powdered silver nanoparticles using hydrogen in aqueous medium. *Particuology*, 10, 140-143.
- Braik, M., Dridi, C., Ali, M. ben, Ali, M., Abbas, M., Zabala, M., Bausells, J., and Zine, N. (2015). Development of a capacitive chemical sensor based on Co (II) - phthalocyanine acrylate-polymer for detection of perchlorate. (10) 17–23.
- Bulgakov, R. A., Kuznetsova, N. A., Dolotova, O. V, and Ludmila, I. (2012). *Synthesis and Photophysical Properties of Covalent Conjugates of Aqua Synthesis and photophysical properties of covalent conju - gates of aqua platinum (II) and octacarboxy-substituted zinc phthalocyanine*. (April 2019).
- Bunaciu, A. A., Udriștioiu, E. gabriela, and Aboul-Enein, H.Y. (2015). X-Ray Diffraction: Instrumentation and Applications. *Critical Reviews in Analytical Chemistry*, 45(4), 289–299.
- Burat, H. P. K. and A. K. (2020). α - and β -Substituted Metal-Free Phthalocyanines: Synthesis, *Photophysical and Electrochemical Properties*. 18–21.
- Cells, H., Jensen, T. J., Vicente, M. G. H., Luguaya, R., Norton, J., Frank, R., and Smith, K. M. (2011). Effect of Overall Charge and Charge Distribution on Cellular Uptake, Distribution and Phototoxicity of Cationic Porphyrins in HEP2 Cells. *NIH PublicAccess*. 100(2), 100–111.
- Chauhan, S. M. S., Srinivas, K. A., and Srivastava, P. K. (2003). Solvent-free synthesis of phthalocyanines. *Journal of Porphyrins and Phthalocyanines* 548–550.
- Chernonosov, A. A., Ermilov, E. A., Röder, B., Solovyova, L. I., and Fedorova, O. S. (2014). Effect of Some Substituents Increasing the Solubility of Zn(II) and Al(III) Phthalocyanines on Their Photophysical Properties. *Bioinorganic Chemistry and Applications*, 2014(III).

Chhatre, A., Solasa, P., Sakle, S., Thaokar, R., and Mehra, A. (2012). Color and surface plasmon effects in nanoparticle systems: Case of silver nanoparticles prepared by microemulsion route. *Colloids and Surfaces A: Physicochemical and Engineering Aspects*, 404(July), 83–92.

Cieplik, F., Tabenski, L., Buchalla, W., and Maisch, T. (2014). Antimicrobial photodynamic therapy for inactivation of biofilms formed by oral key pathogens. *Frontiers in Microbiology*, 5(405), 1–17.

CLSI, (1999). *Methods for determining bactericidal activity of antimicrobial agents; Approved guideline. CLSI document M26-A. Wayne, PA; Clinical and laboratory standards institute.*

Consumption, A. (2018). WHO Report on Surveillance of Antibiotic Consumption 2016 - 2018 Early implementation. *WHO Report on Surveillance.*

Cormick, M. P., and Durantini, E.N. (2018). Synthesis, spectroscopic properties and photodynamic activity of a novel Zn (II) phthalocyanine substituted by fluconazole Synthesis of Zn (II) phthalocyanine derivative. (II. *Journal of photochemistry* 1–10.

De Caro, C. (2015). UV-VIS Spectrophotometry. *Mettler-Toledo International*, (September 2015), 4–14.

De Matteis, V., Cascione, M., Toma, C., and Leporatti, S. (2018). Silver Nanoparticles: Synthetic Routes, In Vitro Toxicity and Theranostic Applications for Cancer Disease. *Nanomaterials*, 8(5), 319.

Denekamp, I. M., Veenstra, F. L. P., Jungbacker, P., and Rothenberg, G. (2019). A simple synthesis of symmetric phthalocyanines and their respective perfluoro and transition-metal complexes. *Applied Organometallic Chemistry*, 33(5), 1–7.

Denis, T. G. S., and Hamblin, M. R. (2011). An Introduction to Photoantimicrobials : Photodynamic Therapy as a Novel Method of Microbial Pathogen Eradication. *Science against Microbial Pathogens: Communicating Current Research Anf Technological Advances*, (May), 675–683.

Dokládlová, L., Bureš, F., Kuznik, W., Kityk, I. V., Wojciechowski, A., Mikysek, T., and Ludwig, M. (2014). Dicyanobenzene and dicyanopyrazine derived X-shaped charge-transfer chromophores: Comparative and structure-property relationship study. *Organic and Biomolecular Chemistry*, 12(29), 5517–5527.

Eissa, H. H. (2014). Synthesis of bisphthaldicarboximide via the reaction of phthalic anhydride with diamines and evaluation of its biological activity. *International Journal of ChemTech Research*, 6(1), 95–101.

El-Kheshen, A. A., and El-Rab, S. F. G. (2012). Effect of reducing and protecting agents on size of silver nanoparticles and their anti-bacterial activity. *Der Pharma Chemica*, 4(1), 53–65.

Eleonor A. (2004). Disk diffusion method. In Laboratory manual of standardized methods for antimicrobial sensitivity tests for bacteria isolated from aquatic animals and environment. Aquaculture Department. pp. 13-29

Etter, M., and Dinnebier, R. (2014). A Century of Powder Diffraction: A Brief History. *Zeitschrift Für Anorganische Und Allgemeine Chemie*, 46.

Faculty, S., and Chemistry, O. (2014). *Catalytic applications of heterogeneous metal-phthalocyanine complexes Ágnes Zsigmond Catalytic applications of heterogeneous metal-phthalocyanine complexes Péter Bata.*

Franci, G., Falanga, A., Galdiero, S., Palomba, L., Rai, M., Morelli, G., and Galdiero, M. (2015). Silver nanoparticles as potential antibacterial agents. *Molecules*, 20(5), 8856–8874.

Frère, J.-M., and Rigali, S. (2016). The alarming increase in antibiotic-resistant bacteria. *Drug Target Review*, (May, 2016).

Friedrich, C. L., Moyles, D., Beveridge, T. J., and Hancock, R. E. (2000). Antibacterial action of structurally diverse cationic peptides on gram-positive bacteria. *Antimicrobial Agents and Chemotherapy*, 44(8), 2086–2092.

Fukuda, R., Ehara, M., and Nakatsuji, H. (2010). Excited states and electronic spectra of extended tetraazaporphyrins. *Journal of Chemical Physics*, 133(14), 1–16.

Furuyama, T., Miyaji, Y., Maeda, K., Maeda, H., and Segi, M. (2019). Extremely Photostable Electron-Deficient Phthalocyanines that Generate High Levels of Singlet Oxygen. *Chemistry - A European Journal*, 25(7), 1678–1682.

Georgescu, R., Boscornea, C., Calinescu, I., and State, R. (2015). Raman, IR and UV-Vis spectroscopic investigations of some substituted phthalocyanines. *Revista de Chimie*, 66(10), 1554–1557.

Gerothanassis, I. P., Troganis, A., Exarchou, V., and Barbarossou, K. (2002). Nuclear Magnetic Resonance (Nmr) Spectroscopy: Basic Principles and Phenomena, and Their Applications To Chemistry, Biology and Medicine. *Chem. Educ. Res. Pract.*, 3(2), 229–252.

Ghammamy, S., Azimi, M., and Sedaghat, S. (2012). *Preparation and identification of two new phthalocyanines and study of their anti-cancer activity and anti-bacterial properties.* 7(43), 3751–3757.

Ghorbani, J., Rahban, D., Aghamiri, S., Teymouri, A., and Bahador, A. (2018). Photosensitizers in antibacterial photodynamic therapy: An overview. *Laser Therapy*, 27(4), 293–302.

Gorduk, S., Koyun, O., Avciata, O., Altindal, A., and Avciata, U. (2017). Synthesis of Peripherally Tetrasubstituted Phthalocyanines and Their Applications in Schottky Barrier Diodes. *Journal of Chemistry*, 2017.

Granbohm, H., Larismaa, J., Ali, S., Johansson, L. S., and Hannula, S. P. (2018). Control of the size of silver nanoparticles and release of silver in heat treated SiO₂-Ag composite powders. *Materials*, 11(1), 1–17.

Gümrükçü, G. G., Keser, G., and Karao, L. (2014). *Properties of Zinc Phthalocyanines with Fused or Interrupted Extended Conjugation*. 2014.

Güzel, E., Arslan, B. S., Atmaca, G. Y., Nebioğlu, M., and Erdoğan, A. (2019). High Photosensitized Singlet Oxygen Generating Zinc and Chloroindium Phthalocyanines Bearing (4-isopropylbenzyl)oxy Groups as Potential Agents for Photophysical Applications. *ChemistrySelect*, 4(2), 515–520.

Hajria, A., Jmiib, H., Aloui, F., and Moussa, S. (2018). *Synthesis and Evaluation of Antimicrobial , Antifungal Activity and Cell Viability of Tetrakis- [(4-Methoxy) - Phthalocyaninato] Zn (II)*. 13(Ii), 1–8.

Hanna, J. (2005). *Towards a new horizon of optoelectronic devices with liquid crystals*. 13(4), 259–267.

Hassan, H. S., Elkady, M. F., El-Sayed, E. M., Hamed, A. M., Hussein, A. M., and Mahmoud, I. M. (2018). Synthesis and characterization of zinc oxide nanoparticles using green and chemical synthesis techniques for phenol decontamination. *International Journal of Nanoelectronics and Materials*, 11(2), 179–194.

Hebeish, A., and El-naggar, M. E. (2013). *Nanostructural Features of Silver Nanoparticles Powder Synthesized through Concurrent Formation of the Nanosized Particles of Both Starch and Silver*. 2013.

Hoet, P. H. M., Brüske-Hohlfeld, I., and Salata, O. V. (2004). Nanoparticles - Known and unknown health risks. *Journal of Nanobiotechnology*, 2, 1–15.

Hudzicki, J. (2016). Kirby-Bauer Disk Diffusion Susceptibility Test Protocol. *American Society For Microbiology*, (December 2009), 1–13.

Ince, M., Ocakoglu, K., Hos, M., and Yurt, F. (2019). *Antimicrobial photodynamic therapy against Staphylococcus aureus using zinc phthalocyanine and zinc phthalocyanine- integrated TiO₂ nanoparticles*. 206–212.

Iravani, S., Korbekandi, H., Mirmohammadi, S. V., and Zolfaghari, B. (2014). Synthesis of silver nanoparticles: Chemical, physical and biological methods. *Research in Pharmaceutical Sciences*, 9(6), 385–406.

İşci, Ü., Caner, C., Zorlu, Y., Gürek, A. G., Dumoulin, F., and Ahsen, V. (2014). *Sulfonamide-Substituted Iron Phthalocyanine : Design , Solubility Range , Stability and Oxidation of Olefins*. *Journal of the Chemical Society, Dalton Transactions* 43, 17916-17919.

Isci, U., and N-bridged, N. (2013). Novel N-bridged diiron phthalocyanine complexes : synthesis , characterization and application in oxidation. *Chemical Sciences*, 10(9), 240-260

Jianjun Y.,. (2006). *Synthesis of Novel Red- Shifted Phthalocyanines*. PhD thesis, Dublin City University. (May 2006), 1-200

Joray, M. B., Trucco, L. D., González, M. L., Natalia, G., Napal, D., Palacios, S. M., and Carpinella, M. C. (2015). *Antibacterial and Cytotoxic Activity of Compounds Isolated from Flourensia oolepis*. 2015.

Kalhotka, L., Hrdinová, Z., Kořínková, R., Přichastalová, J., Konečná, M., Kubáč, L., and Lev, J. (2012). *Test of Phthalocyanines Antimicrobial Activity*. 6–11.

Kantekin, H., Gök, Y., Kiliçaslan, M. B., and Acar, I. (2008). Synthesis and characterization of new metal-free and nickel(II) phthalocyanines containing hexaazadioxa macrobicyclic moieties. *Journal of Coordination Chemistry*, 61(2), 229–236.

Kaya, A. (2015). Synthesis, characterization and thermal behaviour of novel phthalocyanines bearing chalcone groups on peripheral positions. *Bulgarian Chemical Communications*, 47(3), 844–848.

Khan, A., Shaheen, A., Mahmood, T., and Rehman, W. (2017). *Novel Synthesis and Characterization of Silver Nanoparticles from Leaf Aqueous Extract of Aloe Vera and their Anti-Microbial Activity*. 1(1).

Khan, M. H. M., Reddy, K. R. V., and Keshavayya, J. (2018). *Antimicrobial Studies on Symmetrically phenyliminophthalocyanine Complexes*. (II).

Khan, M. S., Jabeen, F., Qureshi, N. A., Asghar, M. S., Shakeel, M., and Noureen, A. (2015). Toxicity of silver nanoparticles in fish: a critical review. *Journal of Biology and Environmental Science*, 6(5)

Khatoon, U. T., Rao, K. V., Rao, J. V. R., and Aparna, Y. (2011). Synthesis and characterization of silver nanoparticles by chemical reduction method. *International Conference on Nanoscience, Engineering and Technology (ICONSET 2011)*, 9(05), 97–

99.

Khoza, P., and Nyokong, T. (2015). Photocatalytic behaviour of zinc tetraamino phthalocyanine-silver nanoparticles immobilized on chitosan beads. *Journal of Molecular Catalysis A: Chemical*, 399.

Kim, S. H., Namgoong, J. W., Yuk, S. B., Kim, J. Y., Lee, W., Yoon, C., and Kim, J. P. (2015). Synthesis and characteristics of metal-phthalocyanines tetra-substituted at non-peripheral (α) or peripheral (β) positions, and their applications in LCD color filters. *Journal of Inclusion Phenomena and Macrocyclic Chemistry*, 82(1–2), 195–202.

Kimang'a, A. N. (2012). A situational analysis of antimicrobial drug resistance in Africa: *Ethiopian Journal of Health Sciences*, 22(2), 135–143.

Kirika, R. (2009). *Antimicrobial resistance : The need for action in the East , Central and Southern Africa region*.

Lambert, L., and Mulvey, T. (1996). Ernst Ruska (1906–1988), Designer Extraordinaire of the Electron Microscope: A Memoir. *Advances in Imaging and Electron Physics*, 95, 2-62.

Li, Z., FX Gu, JM Chan, and Wang, R. L. (2007). Therapeutic, Nanoparticles in Medicine: Applications and Developments. *Education Policy Analysis Archives*, 8(5), 761–769.

Li, B., and Webster, T. J. (2018). Bacteria antibiotic resistance: New challenges and opportunities for implant-associated orthopedic infections. *Journal of Orthopaedic Research*, 36(1), 22–32.

Li, W. R., Xie, X. B., Shi, Q. S., Zeng, H. Y., Ou-Yang, Y. S., and Chen, Y. Ben. (2010). Antibacterial activity and mechanism of silver nanoparticles on *Escherichia coli*. *Applied Microbiology and Biotechnology*, 85(4), 1115–1122.

Liang, Y. I., Lu, L. I. M., Chen, Y., and Lin, Y. O. U. K. U. N. (2016). Photodynamic therapy as an antifungal treatment (*Review*). (20), 23–27.

Linares-flores, C., Mendizabal, F., and Arratia-pérez, R. (2015). Substituents role in zinc phthalocyanine derivatives used as dye-sensitized solar cells . A theoretical study using Density Functional Theory. *Chemical Physics Letters*, 639, 172–177.

Liu, Y., Qin, R., Zaat, S. A. J., Breukink, E., and Heger, M. (2015). Antibacterial photodynamic therapy: overview of a promising approach to fight antibiotic-resistant bacterial infections. *Journal of Clinical and Translational Research*, 1(March 2016), 140–167.

- Lu, Z., Rong, K., Li, J., Yang, H., and Chen, R. (2013). Size-dependent antibacterial activities of silver nanoparticles against oral anaerobic pathogenic bacteria. *Journal of Materials Science: Materials in Medicine*, 24(6), 1465–1471.
- Mark, H., Shieh, K.-J., and Qiao, T. X. (2006). Study of Transmission Electron Microscopy (TEM) and Scanning Electron Microscopy (SEM). *Nature and Science*, 4(3), 14–22.
- Manieri, T. M., Cerchiaro, G., and Ribeiro, A. O. (2015). *Photochemical and Photophysical Properties of Phthalocyanines Modified with Optically Active Alcohols*. 13575–13590.
- Mantareva, V. (2010). *Metallophthalocyanines as photodynamic sensitizers for treatment of pathogenic bacteria, uptake and photoinactivation. Metallophthalocyanines for antimicrobial photodynamic therapy: an overview of our experience*. (September 2015).
- Masilela, N., Antunes, E., and Nyokong, T. (2013). Axial coordination of zinc and silicon phthalocyanines to silver and gold nanoparticles: an investigation of their photophysicochemical and antimicrobial behavior. *Journal of Porphyrins and Phthalocyanines*, 17, 417-430.
- Meci, M., Nar, I., and Hamuryudan, E. (2014). Synthesis and electrochemical and spectroelectrochemical characterization of chloromanganese(III) phthalocyanines. *Turkish Journal of Chemistry*, 38, 1064-1072.
- Mehta, B. K., Chhajlani, M., and Shrivastava, D. (2017). Green synthesis of silver nanoparticles and their characterization by XRD. *Frontiers of Physics and Plasma Science IOP Publishing IOP Conf. Series: Journal of Physics*: 836.
- Midatharahalli, M., Shivayogeeswar, C., and Kotresh, E. N. (2019). Green synthesis of Zinc oxide nanoparticles (ZnONps) and their biological activity. *Applied Sciences*, 1(1), 1–10.
- MO, T. (2017). Emerging Antibiotic Resistance in Africa, Threat to Healthcare Delivery. *MOJ Biology and Medicine*, 1(4), 2–4.
- Moeur, H. P., Zanella, A., and Poon, T. (2006). An introduction to UV-vis spectroscopy using sunscreens. *Journal of Chemical Education*, 83(5), 769.
- Mohammed, H. A., and Kareem, M. M. (2017). *Synthesis and Characterization of New Zinc- phthalocyanine with Four Dodecanyl-benzoic Pendant Groups*. (2).
- Mondal, D. and Bera, S. (2014). Porphyrins and phthalocyanines: Promising molecules for light-triggered antibacterial nanoparticles. *Advances in Natural Sciences: Nanoscience and Nanotechnology*, 5(3).

Mosmann, T. (1983). Rapid colorimetric assay for cellular growth and survival: Application to proliferation and cytotoxicity assays. *Journal of Immunological Methods*, 65(1–2), 55–63.

Mugdad, E. (2016). *Preparation, characterization and biological activity of chromium phthalocyanine chloride complex*.

Murariu, M., Stoica, I., Gradinaru, R., Drochioiu, G., and Mangalagiu, I. (2014). Glutathione-based silver nanoparticles with dual biomedical activity. *Revue Roumaine de Chimie*, 59(10), 867–874.

Nandiyanto, A. B. D., Oktiani, R., and Ragadhita, R. (2019). How to read and interpret FTIR spectroscopy of organic material. *Indonesian Journal of Science and Technology*, 4(1), 97–118.

Nasr, M., Elkhatib, W. F., and Eltayeb, W. N. (2018). *In Vitro Evaluation of Antimicrobial Activity and Cytotoxicity of Different Nanobiotics Targeting Multidrug Resistant and Biofilm Forming Staphylococci*. 2018.

Nayab, P. S., Pulaganti, M., Chitta, S. K., Oves, M., and Rahisuddin. (2015). Synthesis, spectroscopic studies of novel N-substituted phthalimides and evaluation of their antibacterial, antioxidant, DNA binding and molecular docking studies. *Bangladesh Journal of Pharmacology*, 10(3), 703–713.

Nemykina, V. N., and Lukyanets, E. A. (2010). Synthesis of substituted phthalocyanines. *Arkivoc*, 2010(1), 136–208.

Nikalje, A. P. (2016). *Nanotechnology and its Applications in Medicine Nanotechnology and its Applications in Medicine*. (March 2015).

Nikolić, M., Vasić, S., Đurđević, J., Stefanović, O., and Čomić, L. (2014). Antibacterial and anti-biofilm activity of ginger Ethanolic extract. *Kragujevac J. Sci. UDC*, 36192548(581), 129–136.

Nombona, N., Maduray, K., Antunes, E., Karsten, A., and Nyokong, T. (2012). Synthesis of phthalocyanine conjugates with gold nanoparticles and liposomes for photodynamic therapy. *J Photochemistry Photobiol B*, 107, 35–44.

Noroozi, M., Zakaria, A., Moxsin, M. M., Wahab, Z. A., and Abedini, A. (2012). Green formation of spherical and dendritic silver nanostructures under microwave irradiation without reducing agent. *International Journal of Molecular Sciences*, 13(7), 8086–8096.

Nwahara, N., Britton, J., and Nyokong, T. (2017). Improving singlet oxygen generating abilities of phthalocyanines : aluminum tetrasulfonated phthalocyanine in the presence of graphene quantum dots and folic acid. *Journal of Coordination Chemistry*, 8972.

- Nyokong, T. (2007). Effects of substituents on the photochemical and photophysical properties of main group metal phthalocyanines. *Coordination Chemistry Reviews*, 251, 1707–1722.
- Nzekwe, I., Agubata, C., Umeyor, C., Okoye, I., and Ogwueleka, C. (2016). Synthesis of Silver Nanoparticles by Sodium Borohydride Reduction Method: Optimization of Conditions for High Anti-staphylococcal Activity. *British Journal of Pharmaceutical Research*, 14(5), 1–9.
- Ogata, H., Nonaka, N., and Lukyanets, E. (2003). Effect of Peripheral Substitution on the Electronic Absorption and Fluorescence Spectra of Metal-Free and Zinc Phthalocyanines. *Chemistry (Weinheim an Der Bergstrasse, Germany)*, 9, 5123–5134.
- Okeke, I. N. and Sosa, A. (2010). Antibiotic Resistance in Africa – Discerning the enemy and plotting a defense. *APUA Research*, 1–19.
- Ombaka, L. M., Ndungu, P. G., and Nyamori, V. O. (2015). Pyrrolic nitrogen-doped carbon nanotubes: Physicochemical properties, interactions with Pd and their role in the selective hydrogenation of nitrobenzophenone. *RSC Advances*, 5(1), 109–122.
- Ombaka, L. M., Ndungu, P. G., Omondi, B., and Nyamori, V. O. (2014). Mechanochemical synthesis and spectroscopic properties of 1,1'-ferrocenyldiacrylonitriles: The effect of para -substituents. *Journal of Coordination Chemistry*, 67(11), 1905–1922.
- Owuama, C. I. (2017). *Determination of minimum inhibitory concentration (MIC) and minimum bactericidal concentration (MBC) using a novel dilution tube method*. 11(23), 977–980.
- Özdemir, P. S., Özgüney, A. T., Kaya Kantar, G., Şaşmaz, S., and Seventekin, N. (2016). An investigation of fastness and antibacterial properties of cotton fabric coloured with water-soluble zinc phthalocyanine containing Azo groups. *Tekstil ve Konfeksiyon*, 26(1), 92–99.
- Paschoal, M. A., and Duarte, S. (2017). *Photodynamic antimicrobial chemotherapy for prevention and treatment of dental caries : a critical review*. 1–5.
- Patir, A., Hwang, G. B., Nair, S. P., Allan, E., and Parkin, I. P. (2018). Photobactericidal Activity of Dual Dyes Encapsulated in Silicone Enhanced by Silver Nanoparticles. *ACS Omega*, 3(6), 6779–6786.
- Pelicano, C. M., Rapadas, N. J., and Magdaluyo, E. (2017). X-ray peak profile analysis of zinc oxide nanoparticles formed by simple precipitation method. *AIP Conference Proceedings*, 1901(December).

- Preetha, D., Arun, R., Kumari, P., and Aarti, C. (2013). Synthesis and characterization of silver nanoparticles using cannonball leaves and their cytotoxic activity against MCF-7 cell line. *Journal of Nanotechnology*, 2013, 1–5.
- Ragàs, X., He, X., Agut, M., Roxo-Rosa, M., Gonsalves, A. R., Serra, A. C., and Nonell, S. (2013). Singlet oxygen in antimicrobial photodynamic therapy: photosensitizer-dependent production and decay in *E. coli*. *Molecules (Basel, Switzerland)*, 18(3), 2712–2725.
- Rapulenyane, N. (2013). *Photophysicochemical and photodynamic antimicrobial chemotherapeutic studies of novel phthalocyanines conjugated to silver master of science of nomasonto rapulenyane*. (February, 2013), 1–134.
- Revuelta-maza, M. A., Nonell, S., Torre, G. De, and Torres, T. (2019). *Biomolecular Chemistry Boosting the singlet oxygen photosensitization abilities of Zn (II) phthalocyanines through functionalization with bulky fluorinated*. 7448–7454.
- Ruiz-gonzález, R., Reddi, E., and Nonell, S. (2015). *A Comparative Study on Two Cationic Porphycenes : Photophysical and Antimicrobial Photoinactivation Evaluation*. 27072–27086.
- Sadiku, E. R., Agboola, O., Agboola, O., Ibrahim, I. D., Olubambi, P. A., Avabaram, B., and Chima, B. (2018). Nanotechnology in Paints and Coatings. In *Advanced Coating Materials*.
- Sakamoto, K., and Ohno-okumura, E. (2009). *Syntheses and Functional Properties of Phthalocyanines*. 1127–1179.
- Salia M., Agirtas., Ilkay Gu~mus., and Saitizgi M., (2012). Synthesis and reactivity in organic, metal-organic and nano-metal chemistry, (42) 1327-1333.
- Santra, T. S., Tseng, F.-G. (Kevin), and Barik, T. K. (2015). Biosynthesis of Silver and Gold Nanoparticles for Potential Biomedical Applications—A Brief Review. *Journal of Nanopharmaceutics and Drug Delivery*, 2(4), 249–265.
- Saravanan, S., Anantharaman, M. R., and Venkatachalam, S. (2006). Structural and electrical studies on tetrameric cobalt phthalocyanine and polyaniline composites. *Materials Science and Engineering B: Solid-State Materials for Advanced Technology*, 135(2), 113–119.
- Sergeyev, S., Pouzet, E., Debever, O., Levin, J., Gierschner, J., Cornil, J., and Geerts, Y. H. (2007). Liquid crystalline octaalkoxycarbonyl phthalocyanines: Design, synthesis, electronic structure, self-aggregation and mesomorphism. *Journal of Materials Chemistry*, 17(18), 1777–1784.

Seyforth, J. A. (2015). Scanning Electron Microscopy (SEM): An Introduction to the use of SEM for characterising the Surface Topology and Composition of Matter with Further Applications. *Experimental Techniques In Condensed Matter Physics*, (June, 2015).

Shaabani, A. (1999). *Synthesis of mettalophthalocyanines under solvent-free conditions using microwave irradiation*.

Shieh, K., and Qiao, T. X. (2006). Study of Transmission Electron Microscopy (TEM) and Scanning Electron Microscopy (SEM). *Nature and Science* (3), 14–22.

Simões, C., Gomes, M. C., Neves, M. G. P. M. S., Cunha, Â., Tomé, J. P. C., Tomé, A. C., and Faustino, M. A. F. (2016). *Photodynamic inactivation of Escherichia coli with cationic meso -tetraarylporphyrins – The charge number and charge distribution effects*. 266, 197–204.

Soni, M., Mehta, P., Soni, A., and Goswami, G. K. (2018). Green Nanoparticles : Synthesis and Applications Green Nanoparticles : Synthesis and Applications Manish Soni , Priya Mehta , Anjali Soni And Girish K . Goswami *. *IOSR Journal of Biotechnology and Biochemistry*, 4(3), 78–83.

Staicu, A., Pascu, A., Nuta, A., Sorescu, A., Raditoiu, V., and Pascu, M. L. (2013). Studies about phthalocyanine photosensitizers to be used in photodynamic therapy. *Romanian Reports in Physics*, 65(3), 1032–1051.

Suber, L. (2018). Formation and Oriented Aggregation of Tabular Hexagonal Silver Particles. *Condensed Matter*, 3(2), 13.

Suriati, G., Mariatti, J., and Azizan, A. (2014). Synthesis of silver nanoparticles by chemical reduction method: Effect of reducing agent and surfactant concentration. *International Journal of Automotive and Mechanical Engineering*, 10(December), 1920–1927.

Svedberg, U. (2004). Fourier Transform Infrared Spectroscopy in Industrial Hygiene Applications. *Medicine*, 1–58.

Tadesse, B. T., Ashley, E. A., Ongarello, S., Havumaki, J., Wijegoonewardena, M., González, I. J., and Dittrich, S. (2017). Antimicrobial resistance in Africa: A systematic review. *BMC Infectious Diseases*, 17(1), 1–17.

Tahershamsi, L., Gerasymchuk, Y., Wedzynska, A., Ptak, M., Tretyakova, I., and Lukowiak, A. (2019). Synthesis, Spectroscopic Characterization and Photoactivity of Zr(IV) Phthalocyanines Functionalized with Aminobenzoic Acids and Their GO-Based Composites. *C — Journal of Carbon Research*, 6(1), 1.

Taiwo M. (2017). Emerging Antibiotic Resistance in Africa, Threat to Healthcare Delivery. *Biology and Medicine*, 1(4), 2–4.

Tayfuroğlu, Ö., Kılıçarslan, F. A., Atmaca, G. Y., and Erdogmus, A. (2018). Synthesis, characterization of new phthalocyanines and investigation of photophysical, photochemical properties and theoretical studies. *Journal of Porphyrins and Phthalocyanines*, 22(1–3), 250–265.

Tubiana M. (1996). *Wilhelm Conrad Röntgen et la découverte des rayons X [Wilhelm Conrad Röntgen and the discovery of X-rays]*. *Bulletin de l'Academie nationale de medecine*, 180(1), 97–108.

Ullangula, S., V., R. A., and Ganganaguta, S. (2016). Preparation and Characterization of ZnO Nanoparticles: Application to Sensor Devices. *Sensors and Transducers*, 198(April, 2016), 25–31.

Vallemolinales, R. H., Romero, P. R. D., Quigua, O. R. M., Vallejo, L. W. A. and Arboleda, V. J. W. (2015). Antimicrobial activity of metallo tetra (4-carboxyphenyl) phthalocyanine useful in photodynamic therapy. *Pharmacologyonline*, 2, 131–137.

Varghese, T. (2017). *Nanocomposite for electronic applications. Synthesis and characterization of silver tungstate / iron phthalocyanine nanocomposite for electronic applications*. February 2018.

Walter, M. G., Rudine, A. B., and Wamser, C. C. (2010). *Porphyrins and phthalocyanines in solar photovoltaic cells*. 759–792.

Wang, L., Hu, C., and Shao, L. (2017). The-antimicrobial-activity-of-nanoparticles--present-situati. *International Journal of Nanomedicine*, 12, 1227–1249.

Wang, W., Arshad, M. I., Khurshid, M., Rasool, M. H., Nisar, M. A., Aslam, M. A., and Qamar, M. U. (2018). Antibiotic resistance : a rundown of a global crisis. *Infection and Drug Resistance*, 1645–1658.

Wangai, F. K., Masika, M. M., Lule, G. N., Karari, E. M., Maritim, M. C., Jaoko, and W. G., Kuria, A. (2019). Bridging antimicrobial resistance knowledge gaps: The East African perspective on a global problem. *PLoS ONE*, 14(2), 1–12.

WHO. (2014). Antimicrobial resistance. *Bulletin of the World Health Organization*, 61(3), 383–394.

Wicramarachchi, P., and Hettiarachchi, M. (2011). Synthesis of chitosan stabilised silver nanoparticles using gamma ray radiation and characterisation. *Journal of Scinece*, 6, 65–75.

Wöhrle, D., Schnurpfeil, G., Makarov, S. G., Kazarin, A., and Suvorova, O. N. (2012). Practical Applications of Phthalocyanines – from Dyes and Pigments to Materials for Optical, Electronic and Photo-electronic Devices. *Macroheterocycles*, 5(3), 191–202.

Yamamoto, K., Takagi, A., Hada, M., Taniwaki, R., Mizutani, T., Kimura, Y., Takao, Y., Moriwaki, K., Matsumoto, F., Ito, T., Iwai, T., Hida, K., Mizuno, T., and Ohno, T. (2016). Synthesis and optoelectronic properties of hexachloro- and hexaiodosubnaphthalocyanines as organic electronic materials. *Tetrahedron*, 72, 4918-4924.

Yogesh, B., Deshpande, T., Patil, V., Badgujar, N., Chaudhari, R., and Kulkarni, R., (2014). Synthesis of copper phthalocyanine blue pigment: Comparative evaluations of fusion, solvent and microwave techniques. *International Journal of Applied Engineering Research*. 9. 1271-1278.

Zafar, I., Arfan, M., Rap, N., and Aji, S. (2016). *Austin Biomolecules : Open Access Aluminum Phthalocyanine Derivatives : Potential in Antimicrobial PDT and Photodiagnosis*. 1(2), 1-7.

Zhang, FX Gu, JM Chan, A. Z., and Wang, R. L. (2007). Therapeutic, Nanoparticles in Medicine: Applications and Developments. *Education Policy Analysis Archives*, 8(5), 761-769.

Ziminov, A. V., Ramsh, S. M., Terukov, E. I., Trapeznikova, I. N., Shamanin, V. V., and Yurre, T. A. (2006). Correlation dependences in infrared spectra of metal phthalocyanines. *Semiconductors*, 40(10), 1131-1136.

APPENDICES

6.0: APPENDIX I: Spectrums for synthesized compounds

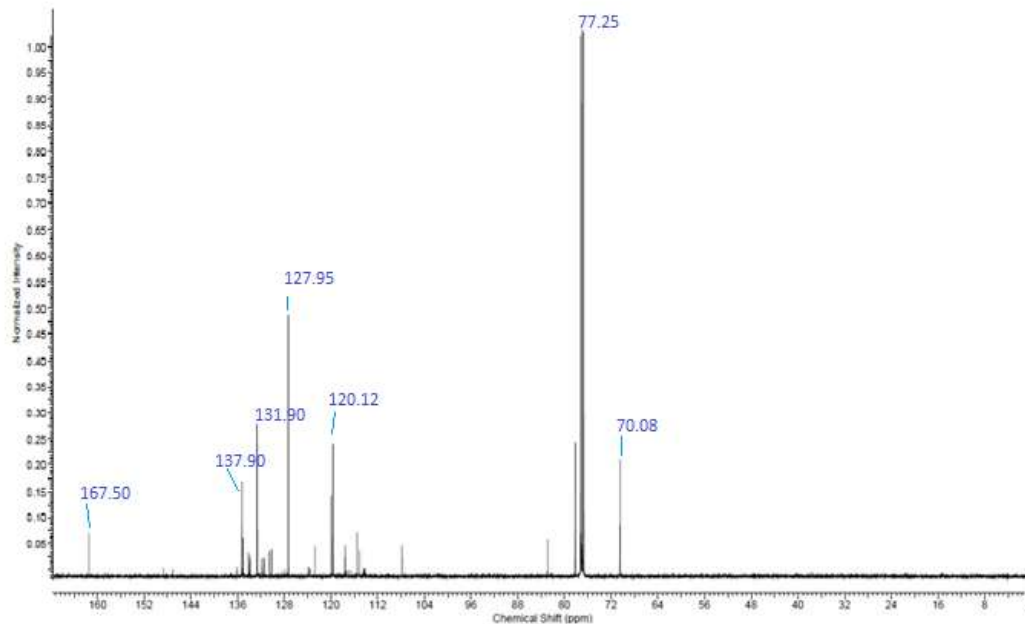
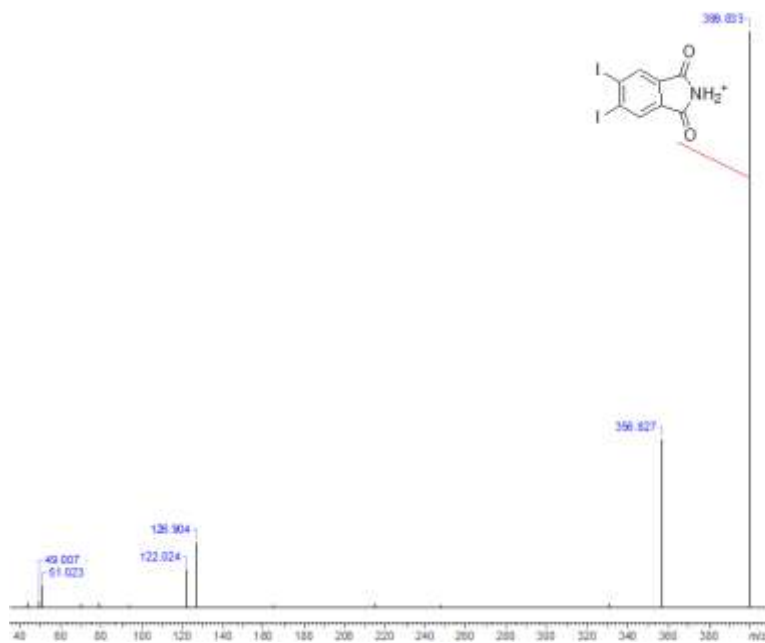
Figure 6.1: ^{13}C NMR spectrum of 4,5-diiodophthalimide (1)

Figure 6.2: HRMS spectrum of 4,5-diiodophthalimide (1)

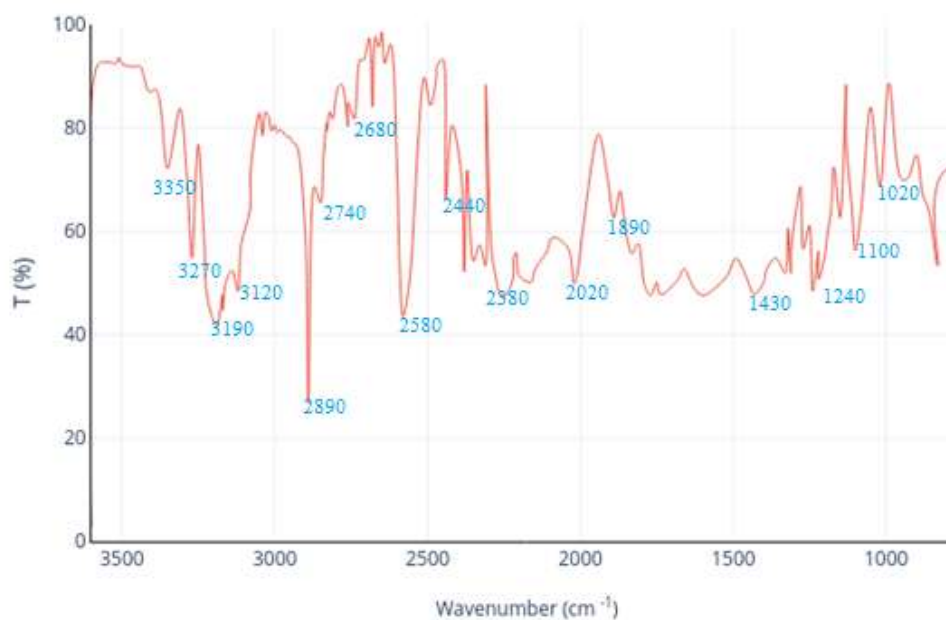


Figure 6.3: FTIR spectrum of 4-iodo-5-(3-methoxy prop-1-nyl) phthalimide (2)

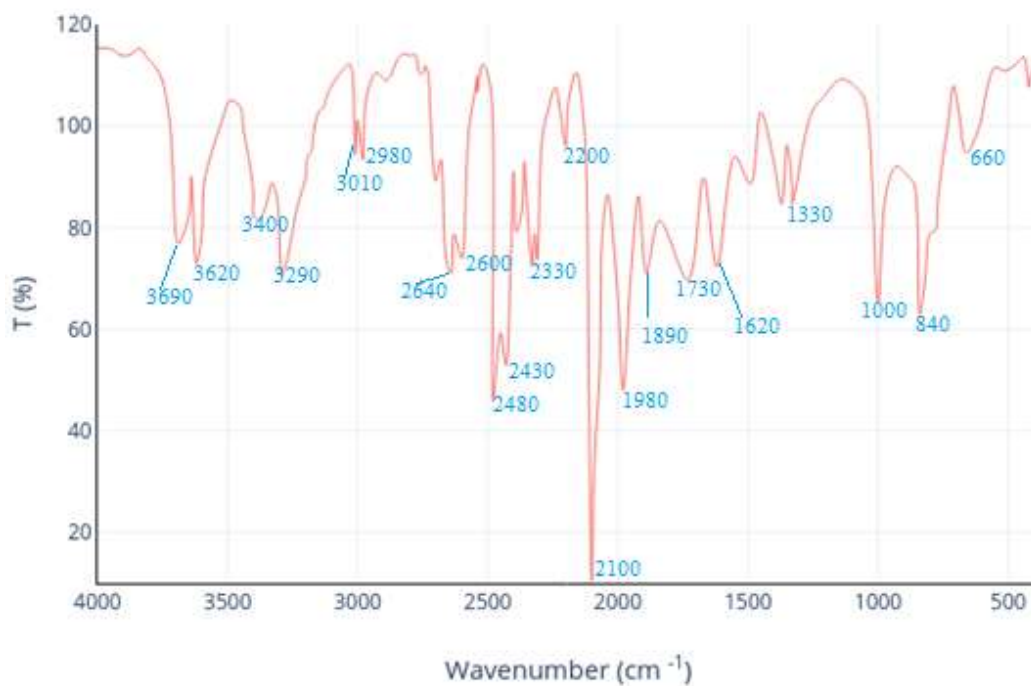


Figure 6.4: FTIR spectrum of 4-iodo-5-ethylsulphonyl phthalimide (7)

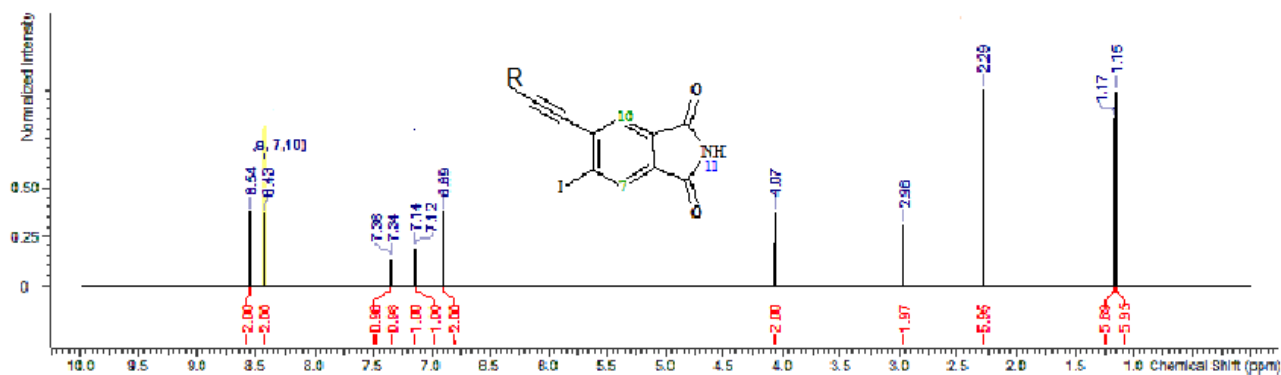


Figure 6.5: ^1H NMR spectrum of 4-iodo-5-(3-methoxy prop-1-nyl) phthalimide (2)

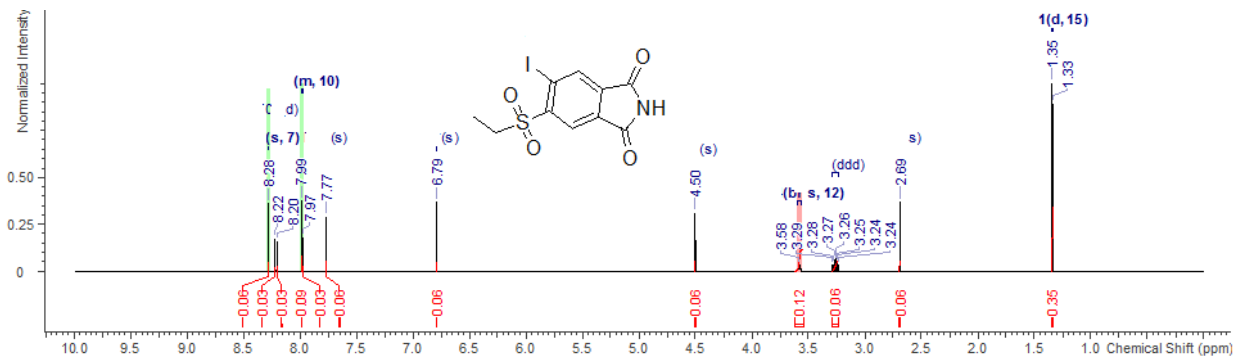


Figure 6.6: ^1H NMR spectrum of 4-iodo-5-ethylsulphonyl phthalimide (7)

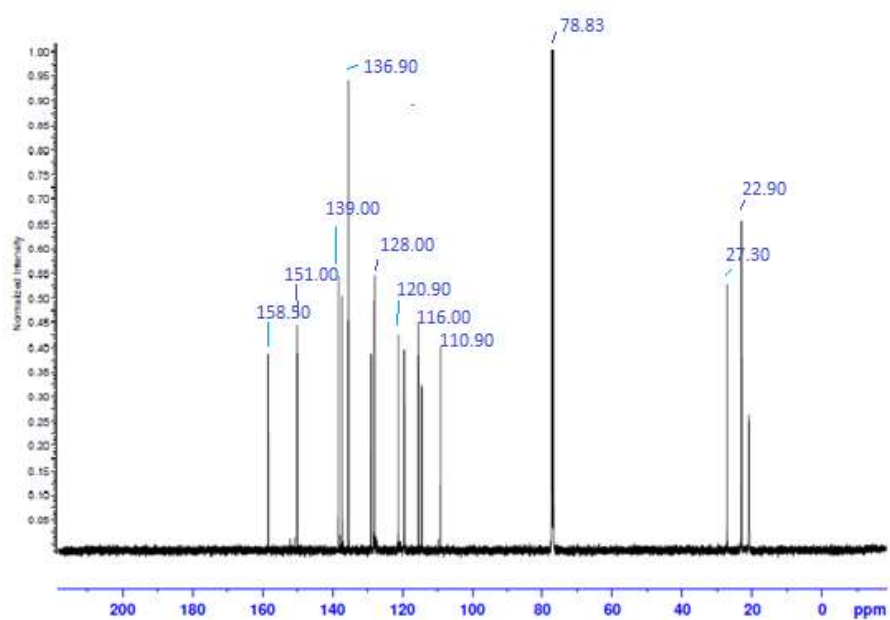


Figure 6.7: ^{13}C NMR spectrum of 4-iodo-5-(3-methoxy prop-1-nyl) phthalimide (2)

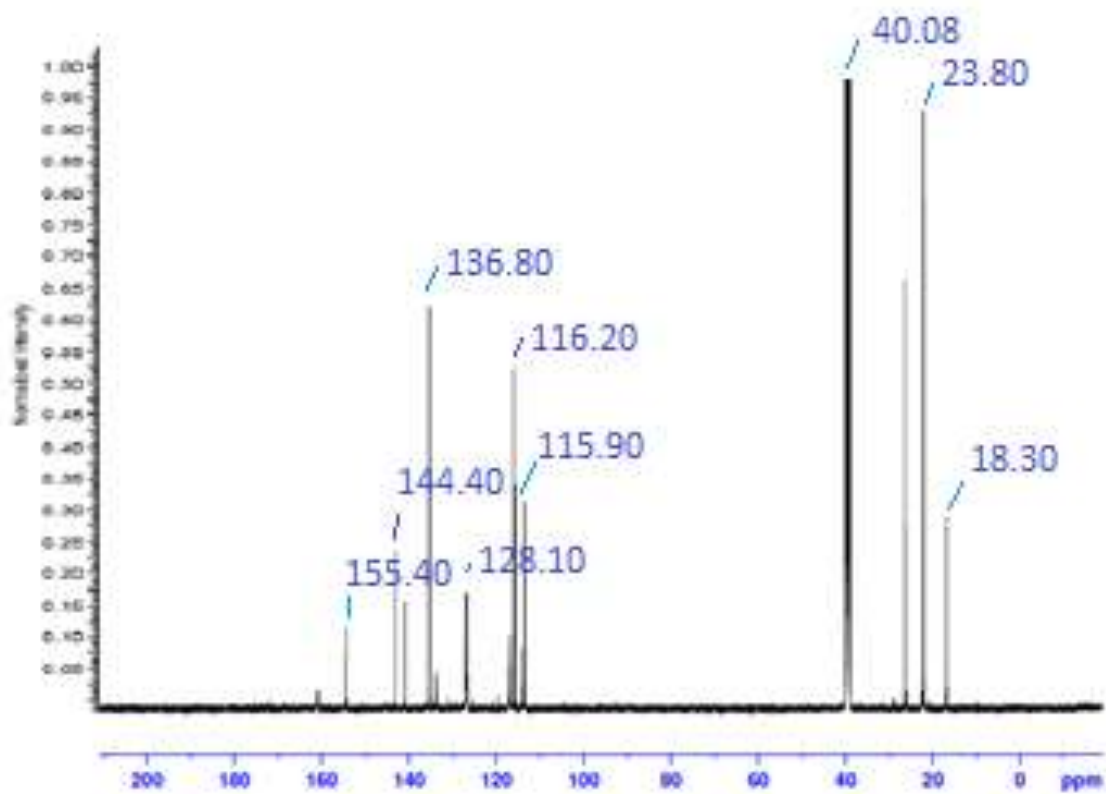


Figure 6.8: ^{13}C NMR spectrum of 4-iodo-5-ethylsulphonyl phthalimide (7)

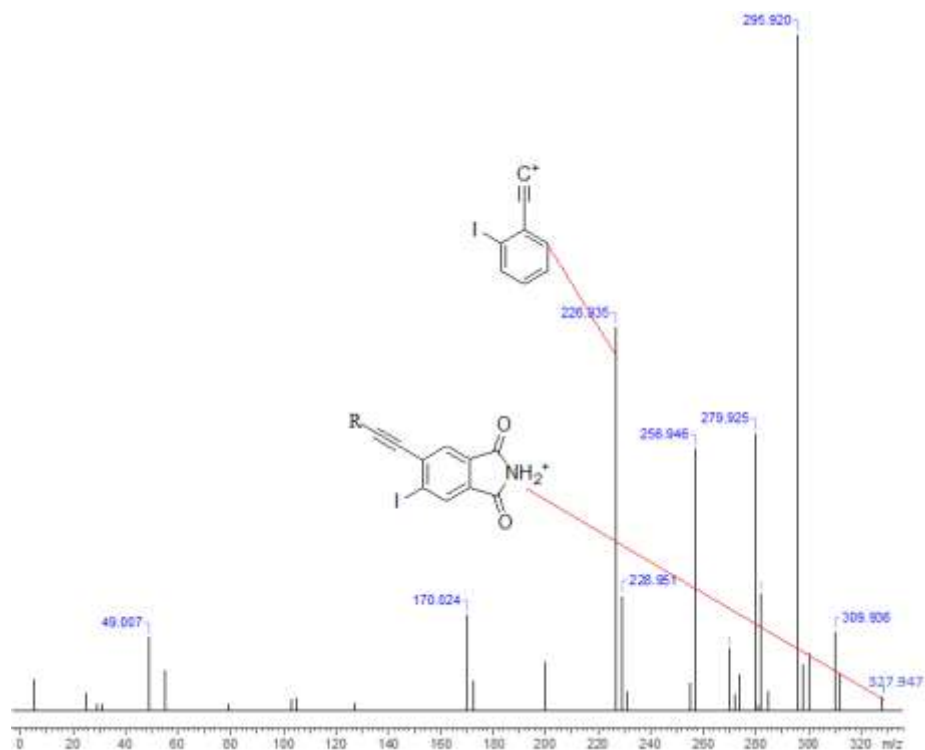


Figure 6.9: HR-MS spectrum of 4-iodo-5-(3-methoxy prop-1-nyl) phthalimide (2)

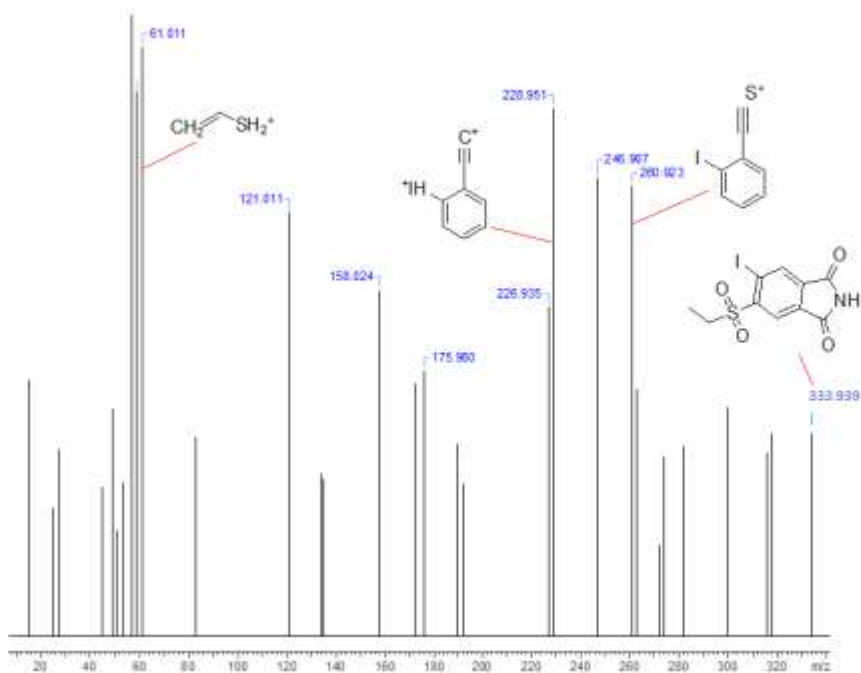


Figure 6.10: HR-MS spectrum of 4-iodo-5-Ethylsulphonyl phthalimide (7)

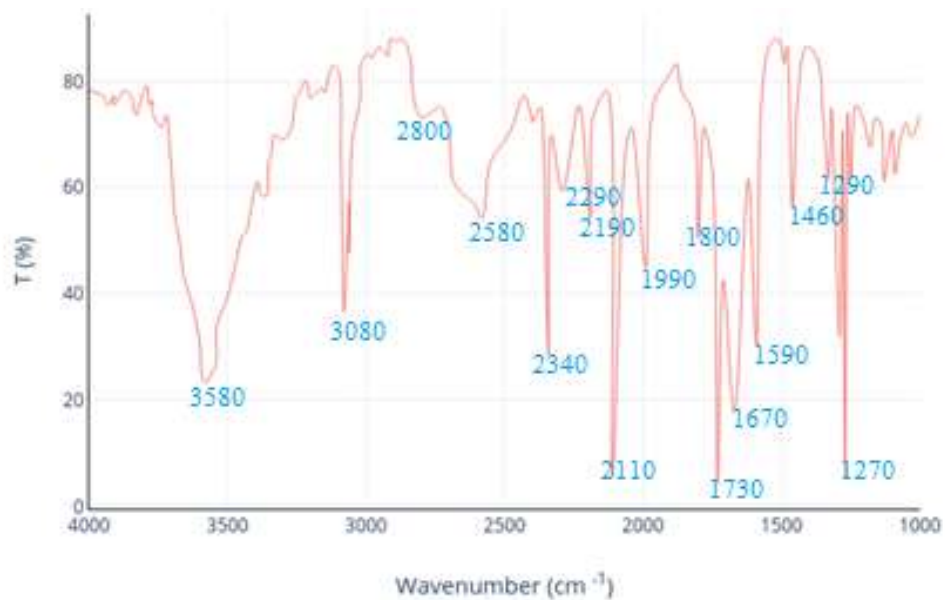


Figure 6.11: FTIR spectrum of ZnPc (4)

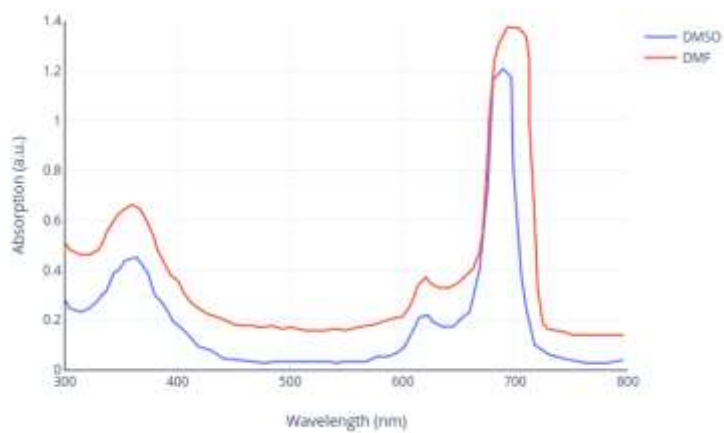


Figure 6.12: UV-VIS spectrum of ZnPc (4)

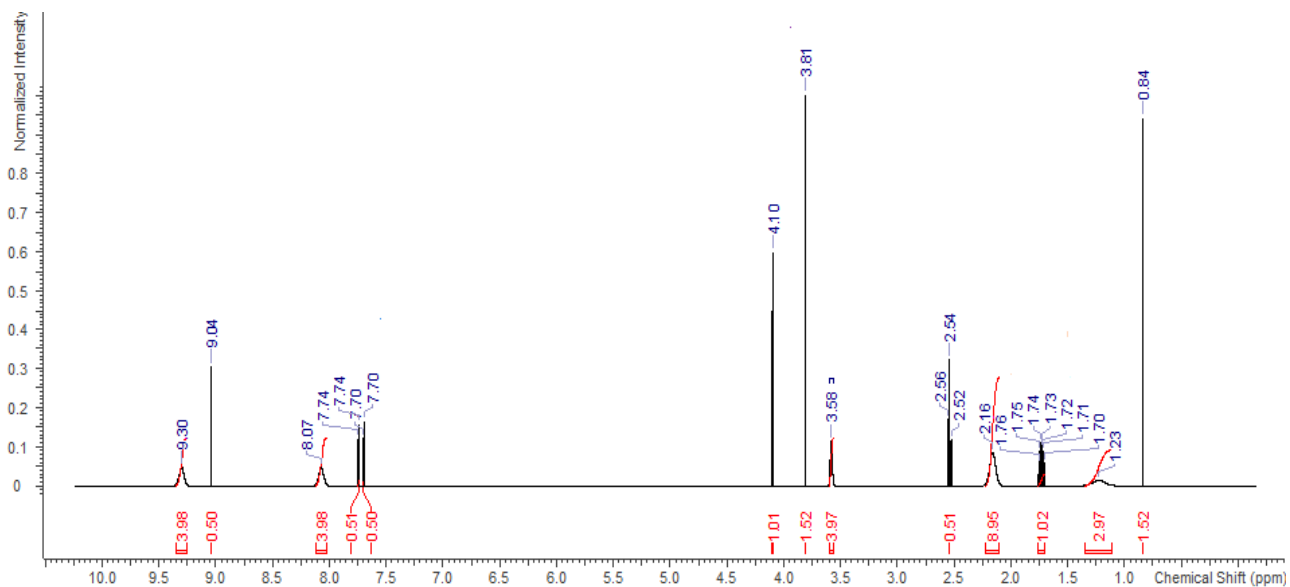


Figure 6.13: ^1H NMR spectrum of ZnPc (4)

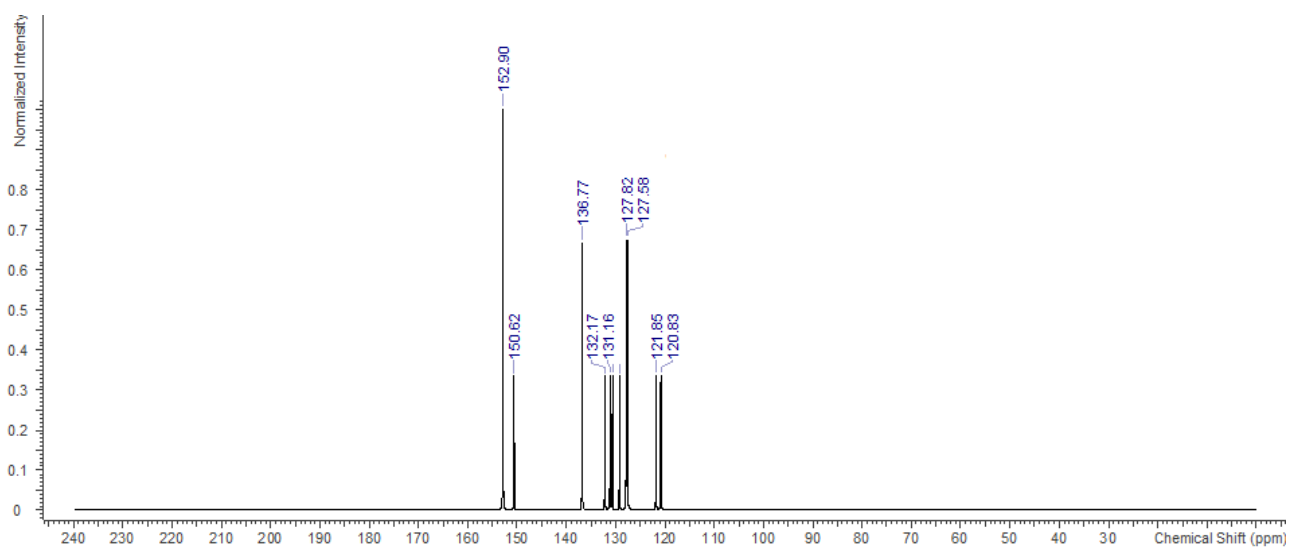


Figure 6.14: ^{13}C NMR spectrum of ZnPc (4)

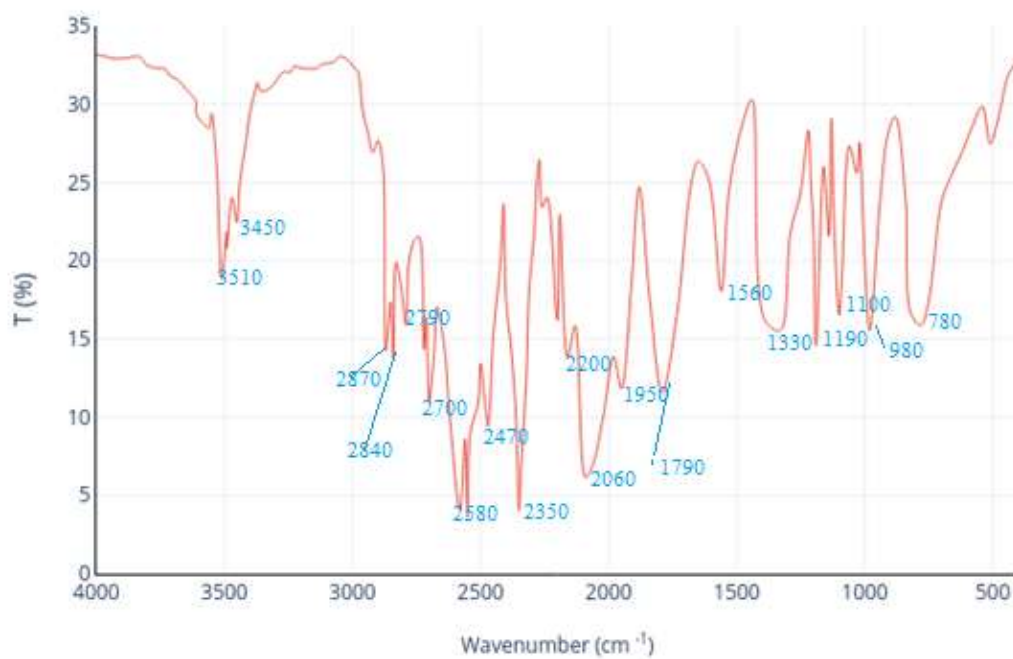


Figure 6.15: FTIR spectrum of 2,9,16,23-tetraiodo-3,10,17,24-tetra(3-methoxyprop-1-nyl) Pc (5)

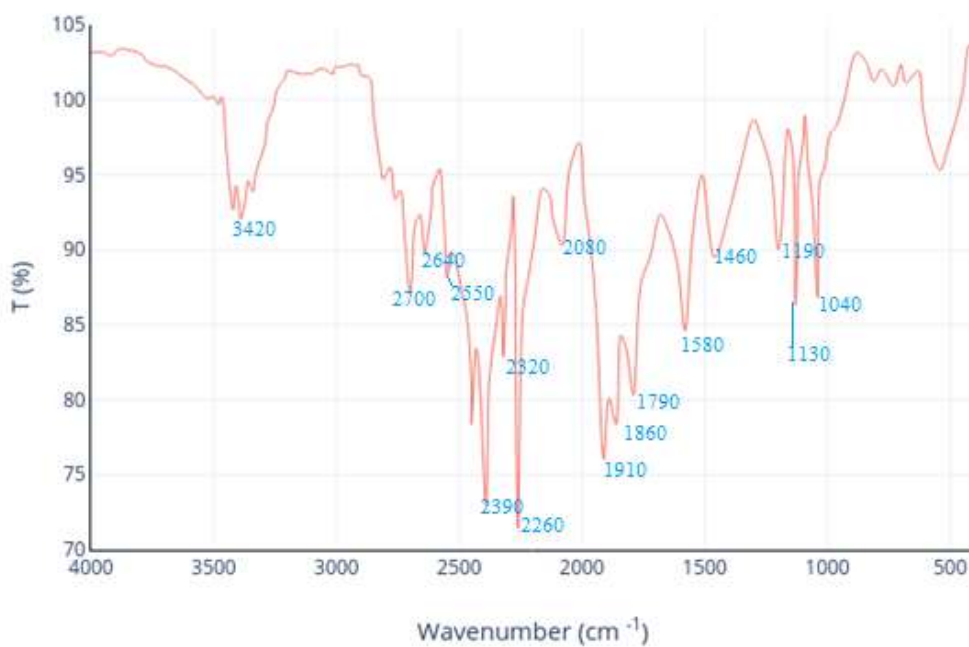


Figure 6.16: FTIR spectrum of 2,9,16,23-tetraiodo-3,10,17,24-tetra ethylsulfonyl Pc (9)

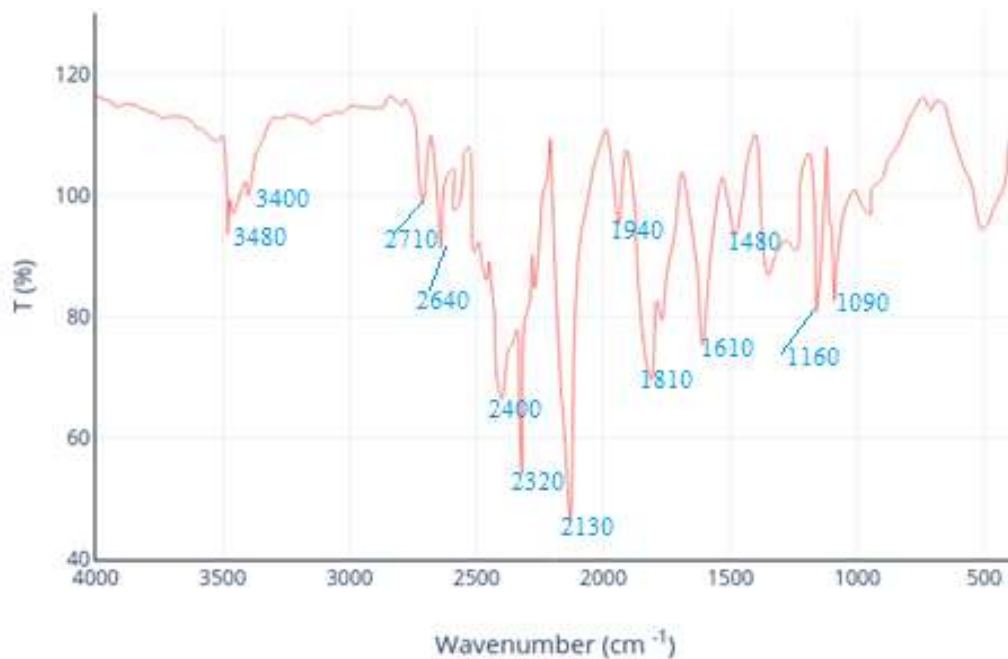


Figure 6.17: FTIR spectrum of 2,9,16,23-tetraiodo-3,10,17,24-tetra(3-methoxy prop-1-nyl) zinc Pc (6)

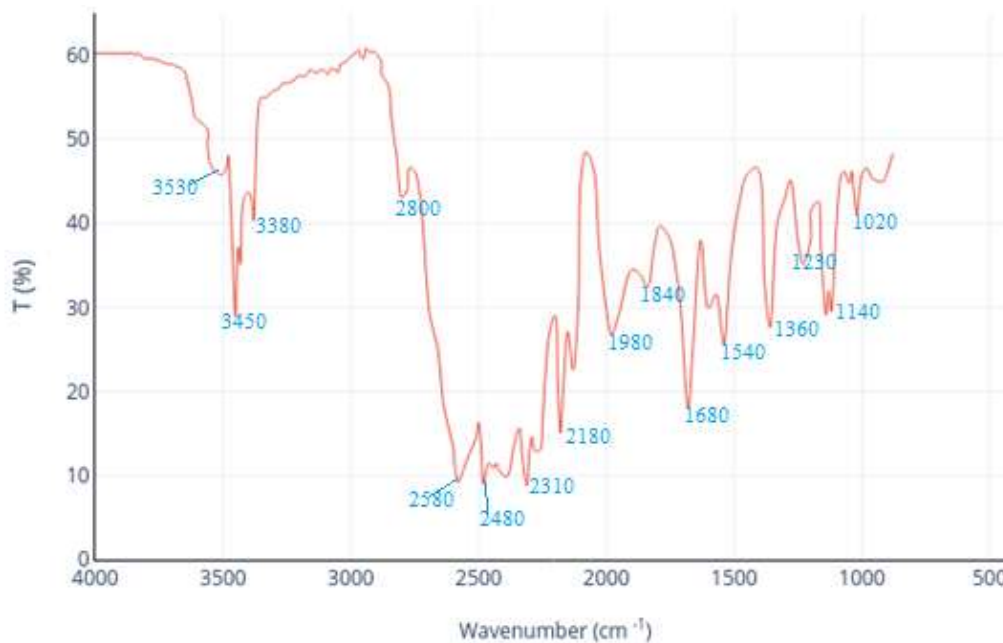


Figure 6.18: FTIR spectrum of 2,9,16,23-tetraiodo-3,10,17,24-tetraethylsulfonyl zinc Pc (10)

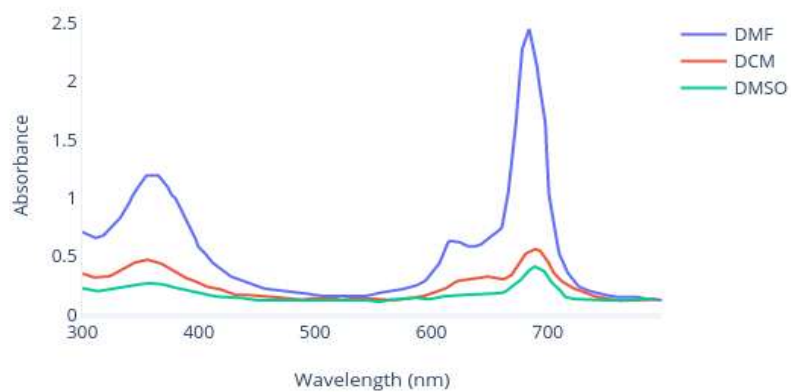


Figure 6.19: UV-Vis spectrum of Pc 6 in different solvent

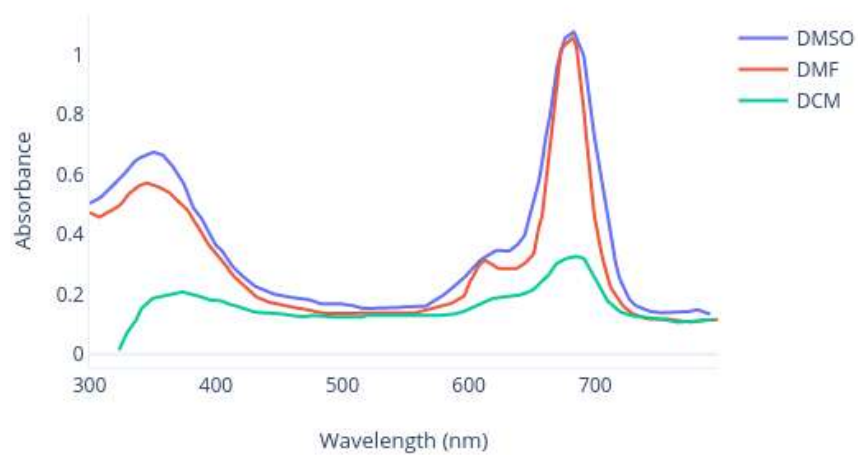


Figure 6.20: UV-Vis spectrum of Pc 10 in different solvent

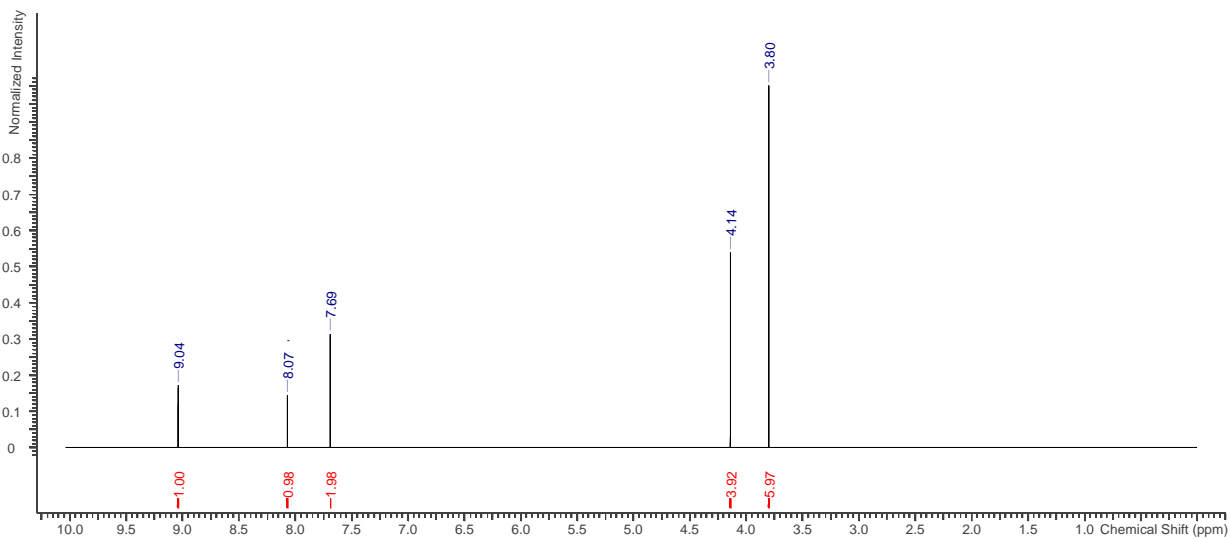


Figure 6.21: ^1H NMR spectrum of Pc 6

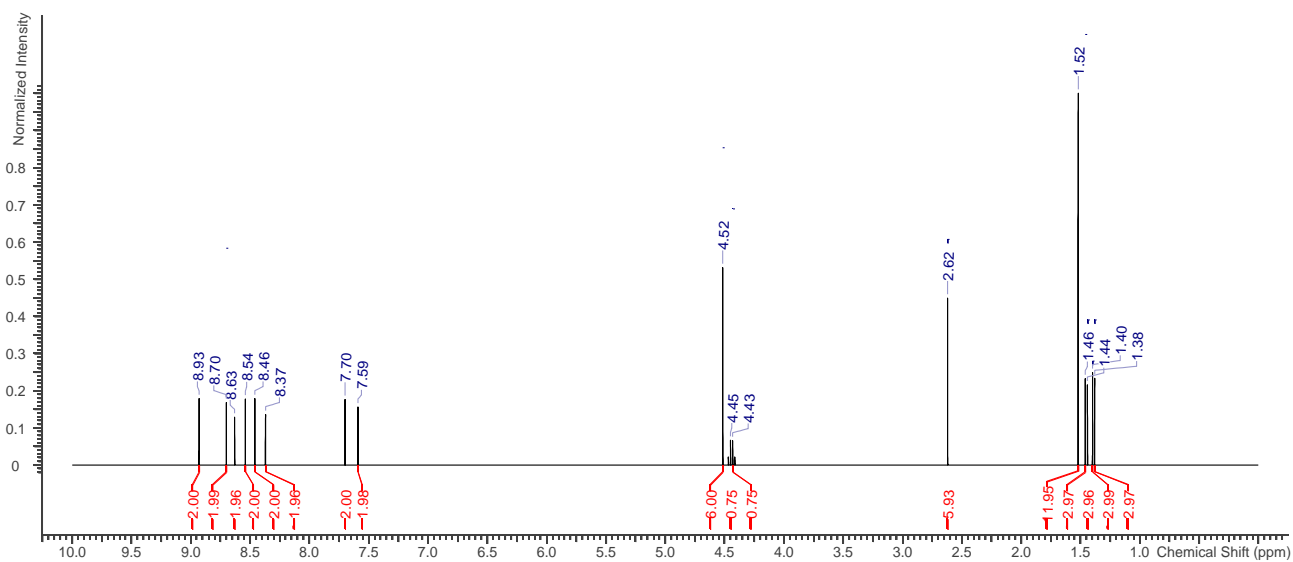


Figure 6.22: ^1H NMR spectrum of Pc 10

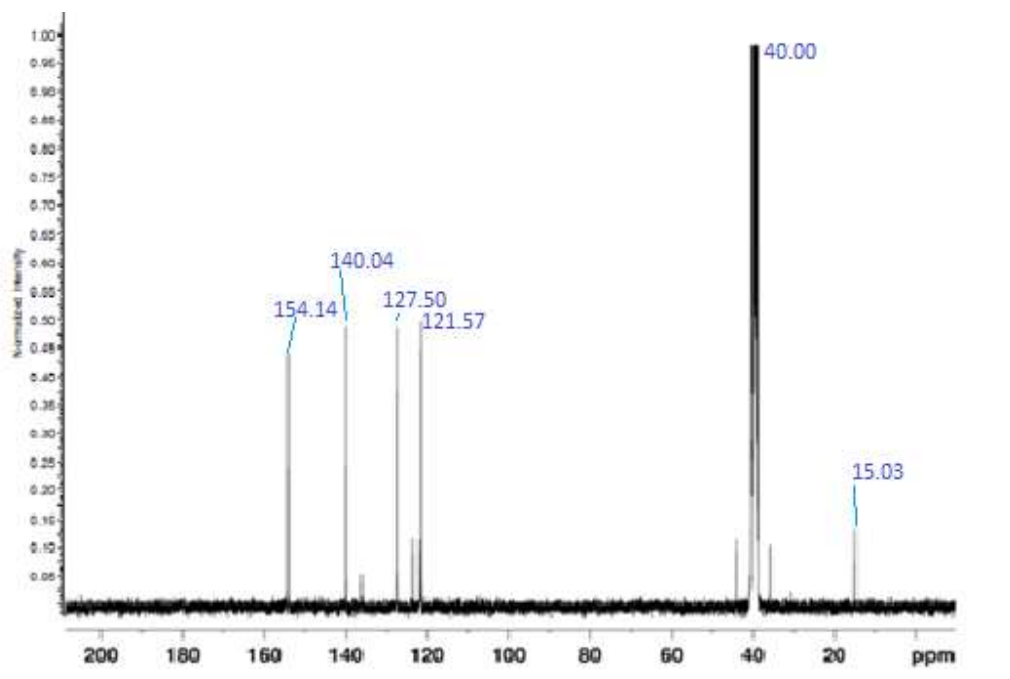


Figure 6.23: ^{13}C NMR spectrum of Pc 6

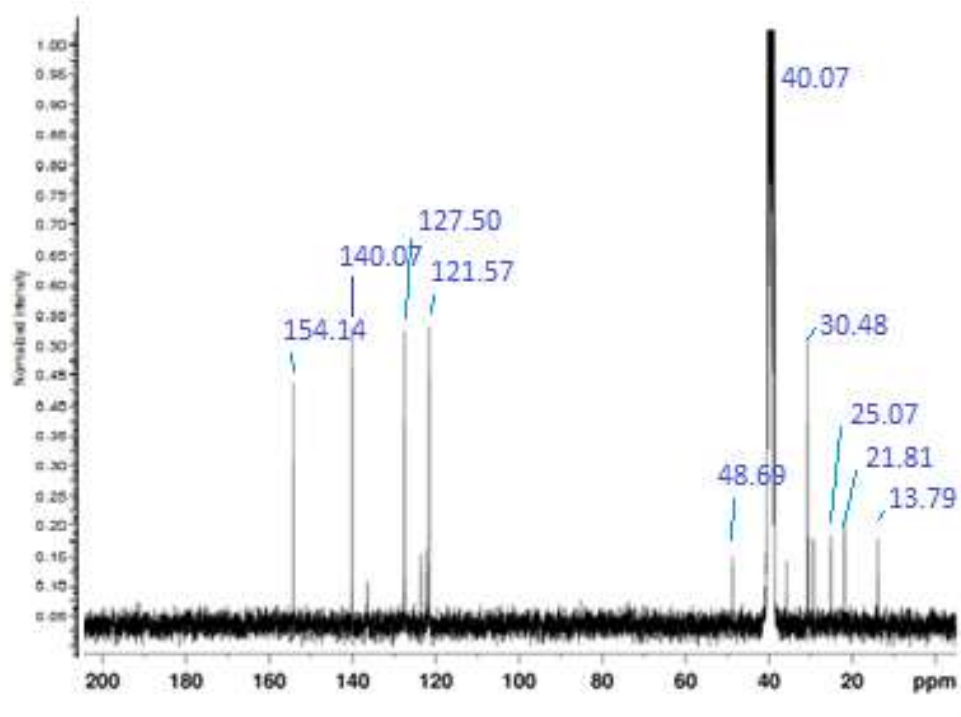


Figure 6.24: ^{13}C NMR spectrum of Pc 10

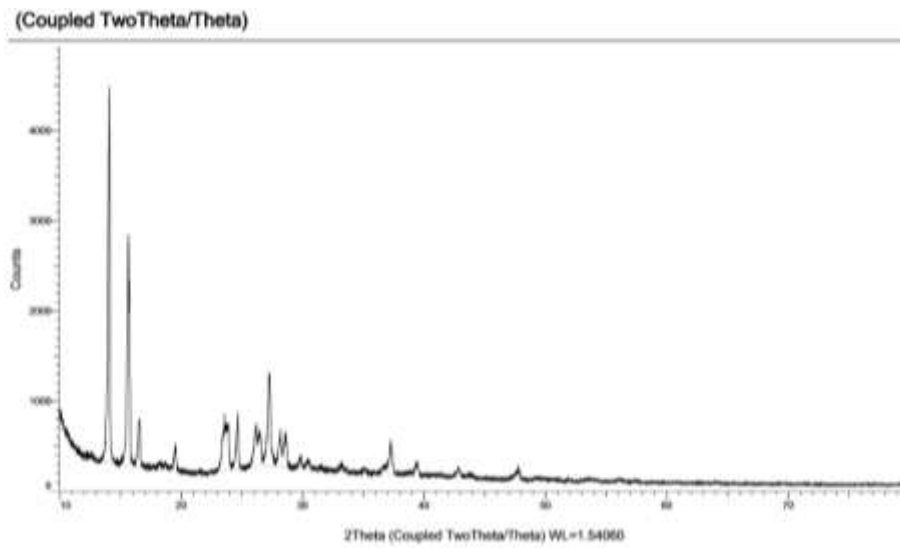


Figure 6.25: XRD spectrum of Pc 6

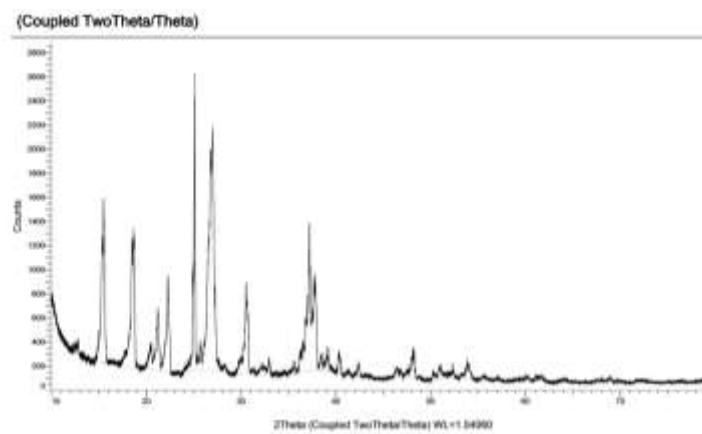


Figure 6.26: XRD spectrum of Pc 10

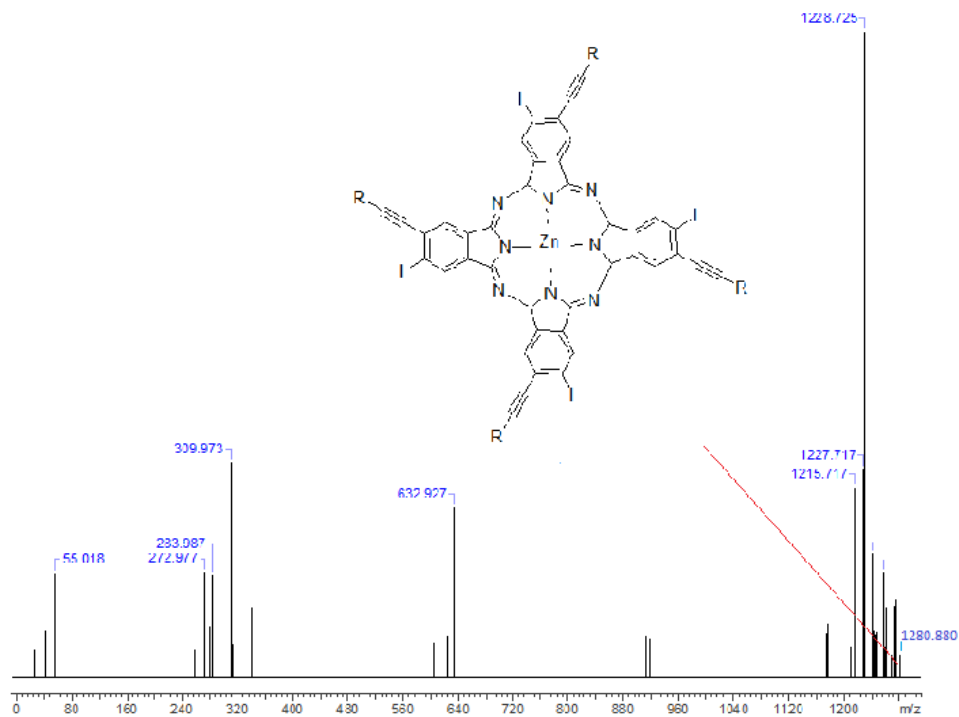


Figure 6.27: HR-MS spectrum of Pc 6

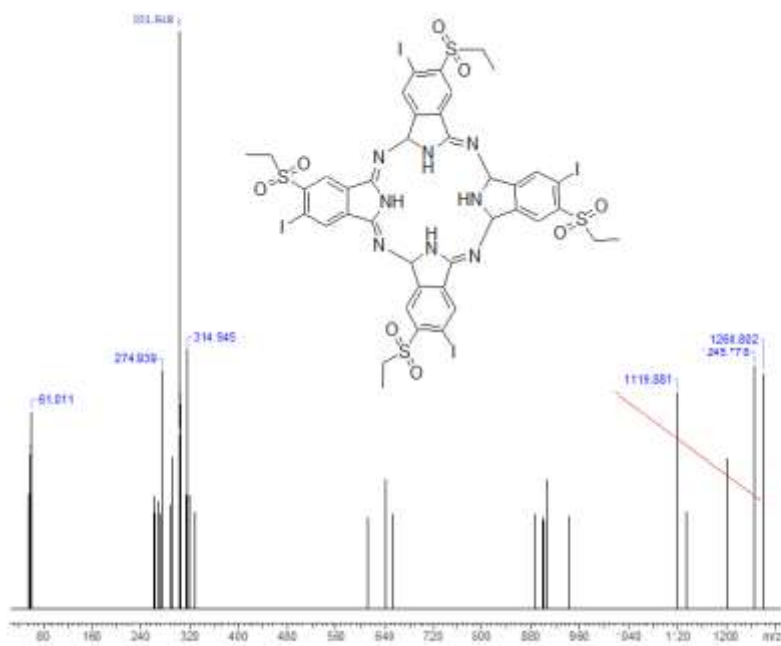


Figure 6.28: HR-MS spectrum of Pc 10

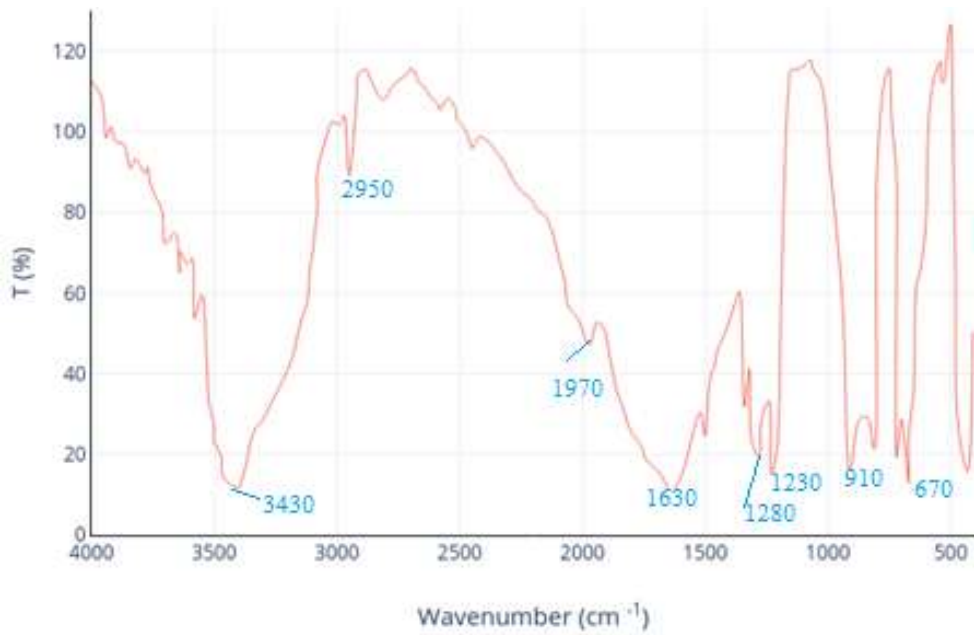


Figure 6.29: FTIR spectrum of ZnO-Np

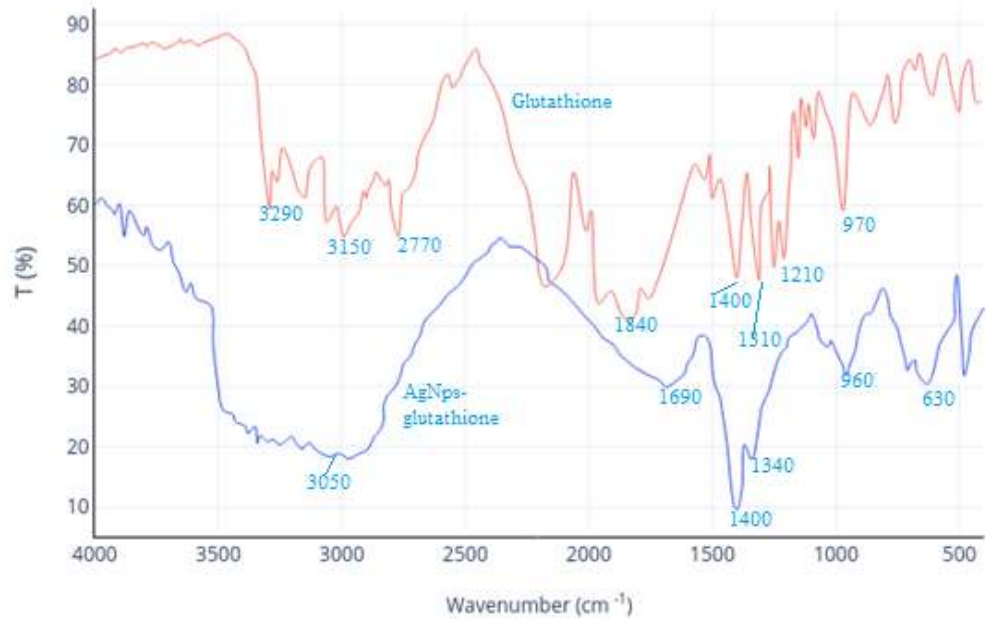


Figure 6.30: FTIR spectrum of glutathione and that of AgNP stabilized with glutathione

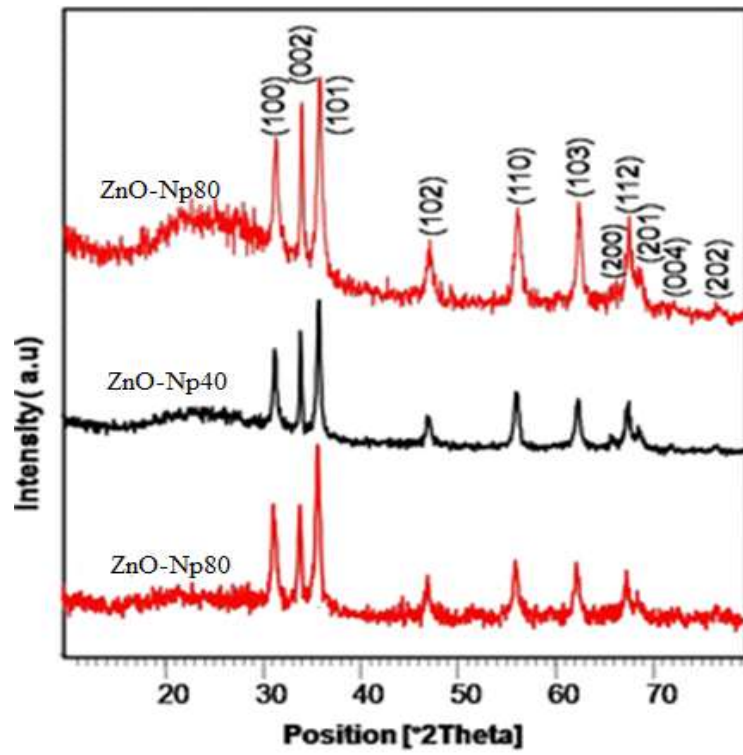


Figure 6.31: XRD pattern of ZnO-Nps

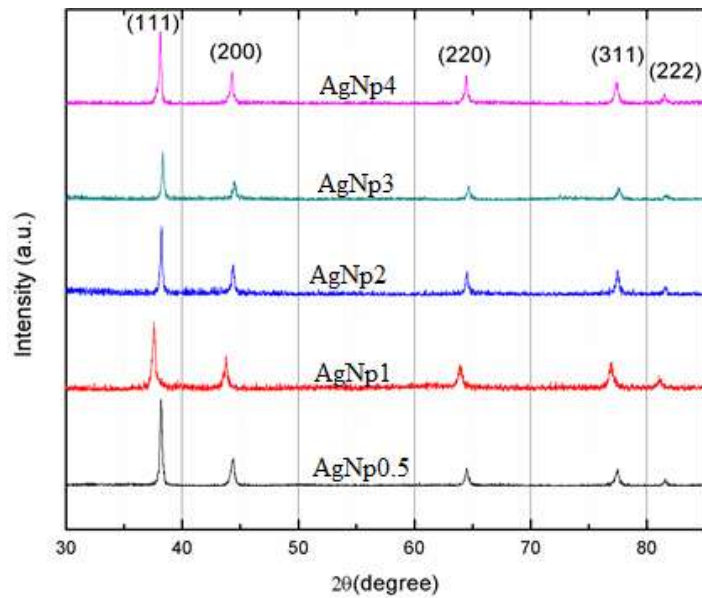


Figure 6.32: XRD pattern of AgNps

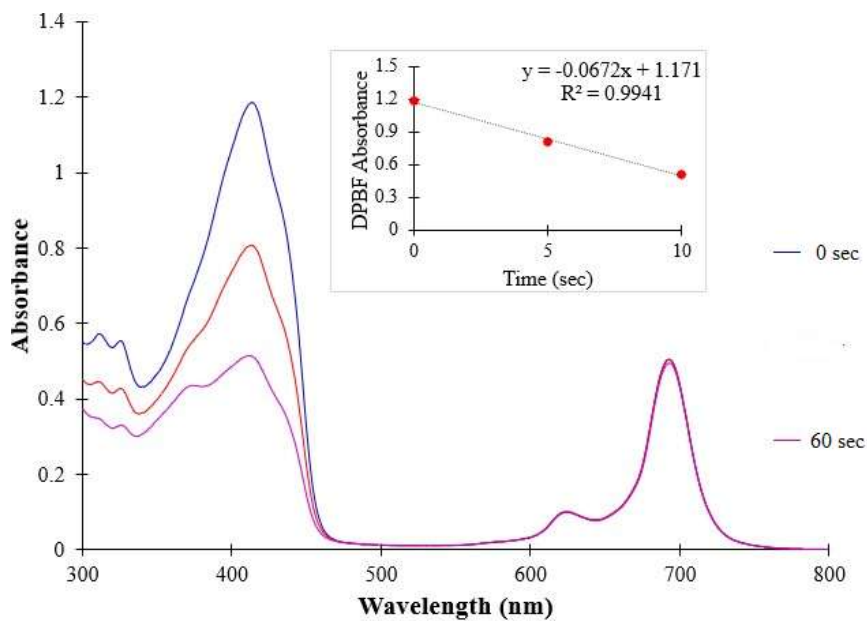


Figure 6.33: UV-Vis spectrum changes of Pc 6 along with the singlet oxygen quantum yield (Solvent: DMSO, $C=1 \times 10^{-5} M$).

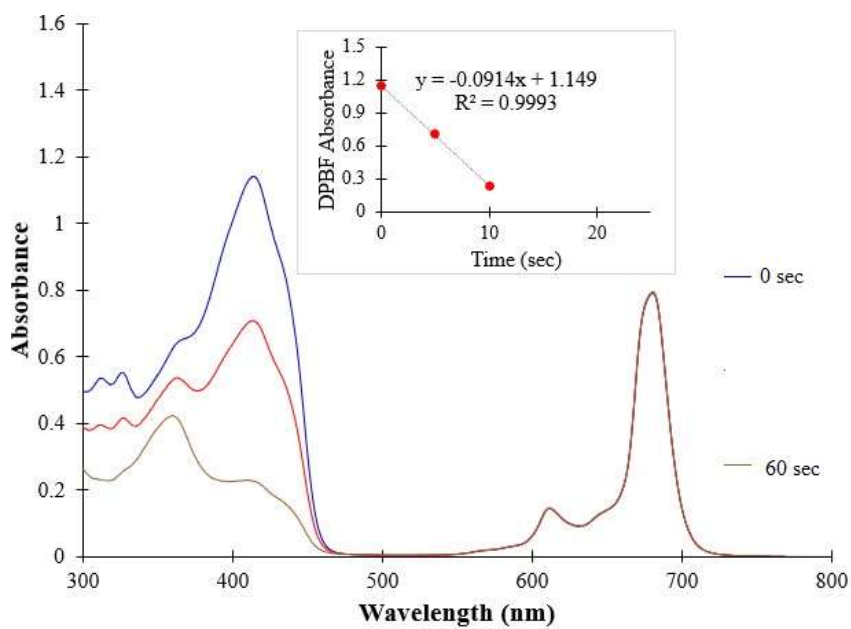


Figure 6.34: UV-Vis spectrum changes of Pc 6-AgNp with the singlet oxygen quantum yield (Solvent: DMSO, $C=1 \times 10^{-5} M$).

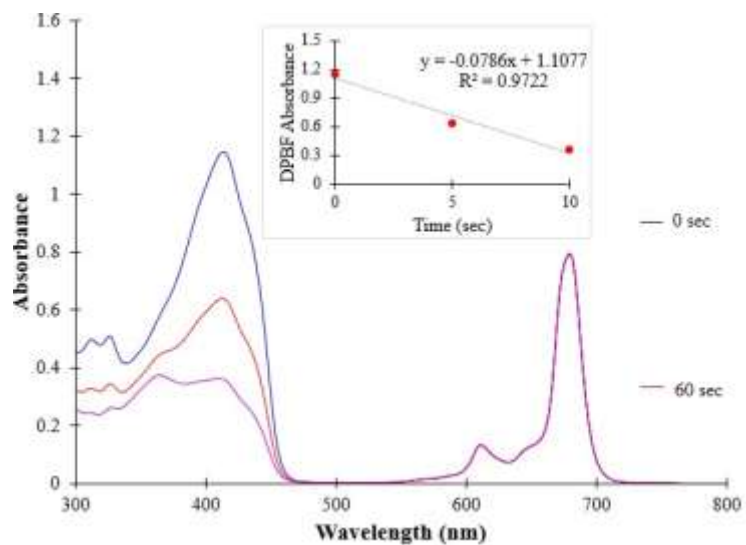



Figure 6.35: UV-Vis spectrum changes of Pc 10-AgNps along with the singlet oxygen quantum yield (Solvent: DMSO, $C=1 \times 10^{-5} \text{ M}$).

APPENDIX 2: Published paper

ORIGINAL ARTICLE

One-pot microwave-assisted synthesis of size-dependent L-glutathione-capped spherical silver nanoparticles suitable for materials with antibacterial properties

Samuel N. Nyamu,^{1*}  Lucy Ombaka,² Eric Masika¹ & Margaret Ng'ang'a¹

¹ Department of Chemistry, Kenyatta University, P.O. Box 43844, 00100, Nairobi, Kenya

² Department of Chemistry, Technical University of Kenya, P.O. Box 52428, 00200, Nairobi, Kenya

Keywords

Capping agent, glutathione size dependent, microwave synthesis, silver nanoparticles.

*Correspondence to: Samuel N. Nyamu, Department of Chemistry, Kenyatta University, P.O. Box 43844, 00100 Nairobi, Kenya. Email: nyamusamnju@gmail.com

FUNDING INFORMATION

Kenyatta University; National Research Fund Kenya (NRF); Ministry of Higher Education Kenya; Africa Development Bank

Received: 10 April 2019;

Revised: 09 June 2019;

Accepted: 20 June 2019

Journal of Interdisciplinary
Nanomedicine,
2019; 4(3), doi: 10.1002/jin2.62

Abstract

In the last years, there has been an alarming increase in antibiotic resistance by pathogenic microbes, which has become a major public health concern. There is a great interest in developing new antimicrobial for reducing the impact. Silver nanoparticles (AgNPs) as antibacterial agents are currently being studied to be used to fight these pathogenic microbes. The aim of the present study was to synthesize AgNPs of different sizes through the use of microwave and determine their antimicrobial activities. Synthesis of size-dependent L-glutathione-capped spherical nanoparticles through one-pot microwave synthesis was achieved, and their antimicrobial properties were determined. Different sizes of AgNPs between 5–10, 15–35, and 50–80 nm were made by varying the concentration of silver nitrate and using sodium borohydride (NaBH₄) as a reducing agent. L-glutathione was used to stabilize the AgNPs to prevent them from aggregation in the colloidal solution. The synthesized AgNPs showed ultraviolet absorption at around 400 nm with high concentration of AgNO₃ having sharp peaks. The formed particles were crystalline in nature with uniform spherical shape. The formed AgNPs were of crystalline size of 9.94, 18.45, 34.96, 52.40, and 58.50 nm. Fourier transform infrared analysis confirmed conjugation of glutathione as a capping agent to AgNPs as the result of the formed spectra showing the absence of νSH stretch. The high temperature generated by microwave helped to synthesize nanoparticles within a short time and by varying the concentration of AgNO₃ helped obtain the desired particle size. Glutathione conjugated well with AgNPs as a result of interaction of negative thiol resulting to colloidal stabilization and reduced aggregation. The antibacterial activity of AgNPs was found to be size dependent with the smaller size of 9.94 nm being more efficient than 18.45, 34.96, 52.40, and 58.50 nm against the tested strains *Bacillus subtilis* (ATCC 6633), *Escherichia coli* (ATCC 25922), *Salmonella* spp. (ATCC 700623), and *Staphylococcus aureus* (ATCC 25923). Of the four stains, *E. coli* was found to be the least affected by all three different particle sizes of the synthesized AgNPs.

Review Article

Antimicrobial Photodynamic Activity of Phthalocyanine Derivatives

Samuel N. Nyamu ¹, Lucy Ombaka,² Eric Masika,¹ and Margaret Ng'ang'a¹

¹Department of Chemistry, Kenyatta University, P.O. Box 43844-00100, Nairobi, Kenya

²Department of Chemical Science and Technology, Technical University of Kenya, P.O. Box 52428-00200, Nairobi, Kenya

Correspondence should be addressed to Samuel N. Nyamu; nyamusamnju@gmail.com

Received 27 September 2017; Revised 11 December 2017; Accepted 15 January 2018; Published 19 March 2018

Academic Editor: Viktor O. Iaroshenko

Copyright © 2018 Samuel N. Nyamu et al. This is an open access article distributed under the Creative Commons Attribution License, which permits unrestricted use, distribution, and reproduction in any medium, provided the original work is properly cited.

Microbial pathogens have increasingly shown multidrug resistance posing a serious threat to the public health. Advances in technology are opening novel avenues for discovery of compounds that will mitigate the ever-increasing drug-resistant microbes. Use of photodynamic photosensitizer is one of the promising alternative approaches since they offer low risk of bacteria resistance as they use generated reactive oxygen species to kill the microbes. Phthalocyanine (Pc) is one such photosensitizer which has already shown promising antimicrobial photodynamic therapeutic properties. Previous studies have shown effectiveness of the Pc against Gram-positive bacteria. However, its effectiveness toward Gram-negative bacteria is limited by the impermeability of the bacteria's outer membrane which is made up of lipopolysaccharides layer. The effectiveness of this photosensitizer is determined by its photophysical and photochemical properties such as singlet/triplet lifetimes, singlet oxygen quantum yields, and fluorescence quantum yield. Therefore, this review focuses on the recent significance advances on designing Pc that have this improved property by either conjugating with nanoparticles, quantum dots, functional groups in peripheral position, considering effect of cationic charge, and its position on the macrocycle.

1. Introduction

Drugs that are effective against microbes are used in both curative and preventive measures in protecting patients against diseases that are fatal to the extent of some resulting in death. Despite the extensive research in area of microbial pathogenesis and the emergence of new antibiotic drugs in the market, morbidity and mortality linked with the pathogens infections keep on increasing [1, 2]. There is alarming growth in antibiotic resistance by pathogenic microbes with an estimate of 45% of all deaths being caused by pathogenic microbes [3]. Antimicrobial resistance is thus one of the most serious health threats. This calls for new effort to discover new ways of eradicating these microbial pathogens [4].

The use of photosensitizers and light is complementary as well as alternate method to the conventional way of fighting against pathogenic microbes. When light of a specific wavelength is illuminated to such photosensitizer molecule, particles with high reactivity are generated that can destroy

pathogenic microbial cells [5]. Previous studies have reported high quantum yield of oxygen production, high photo toxicity when light of specific wavelength is illuminated on them, and high stability in physiological conditions [6, 7]. Photosensitizers that are currently being studied in fighting these microbes include porphyrins, phenothiazines, and phthalocyanine [7].

2. Antibiotic Resistance in Some Parts of Africa

Microbe's causes a big proportion of infection and death in Africa. However, the rise of antibiotic resistance has dented the hope to reduce the infection and death caused by these pathogens [8]. The increasing trend of antibiotic resistance and the slow pace of developing new antibiotics pose a danger to African countries. Resistance to most antibiotics has been shown by microbes like *Vibrio cholera* which has been



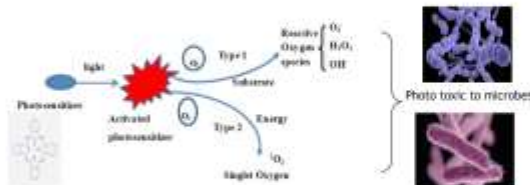
MICROWAVE ASSISTED SYNTHESIS OF PHTHALOCYANINE CONJUGATED TO SILVER NANOPARTICLES AS ANTIMICROBIAL

Nyamu N. Samuel¹, Lucy Ombaka², Eric Masika¹, Margaret Ng'ang'a¹

¹Corresponding author Email: nyamasamuel@gmail.com, ²Department of Chemistry Kenyatta University P.O Box 43844-00100 Nairobi Kenya, ³Department of Chemistry Technical University of Kenya P.O. Box 52428 – 00200 Nairobi- Kenya

Introduction

Phthalocyanine compounds have attracted more attention as photosensitizers for photodynamic therapy due to their photo toxicity when in light and low toxicity in dark. They are also promising compound in fight of resistant microbes. Their antimicrobial properties may be increased by conjugating them with nanoparticles. Phthalocyanine dyes have been synthesized using various solvents which are not environmental friendly. We therefore, synthesized novel phthalocyanines(2,9,16,23-tetra-iodo-3,10,17,24-tetra-(3-methoxypropyl-2-yl) Phthalocyanine (A) and 2,9,16,23-tetra-iodo-3,10,17,24-tetra-ethylsulfonyl Phthalocyanine (B) and conjugated to silver nanoparticles(Ag-Nps) through microwave-assisted green chemistry. We utilized microwave oven to speed up the reaction, minimize the use and generation of hazardous substances. Compound A and B showed good antimicrobial property compared to the control.



Results

- Compound A- had yield of 43% IR: (KBr) ν_{max} 2355 (C-H); 1112; 961; 836 cm^{-1}
- Compound B- had yield 37% IR: (KBr) ν_{max} 3098 (C-H), 1668, 1590 (C-C), 1437, 1408, 1387 (C-H), 728 (C-S-C), cm^{-1}

XRD indicated the silver nano particles formed were crystalline in nature, SEM and TEM results showed particles with uniform spherical shape with size 9.96 nm, 14.85 nm, 34.96 nm and 59.25 nm

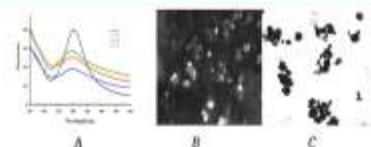


Figure A UV-visible for silver nanoparticle in different concentration, Figure B showing SEM image of Ag-Nps Figure C. TEM image Ag-Nps

Figure D shows UV spectra of phthalocyanine ranging 600-700 nm attributed to the $\pi-\pi^*$ transition and 300-350 nm, arising from the $n-\pi$ bond. B exhibits a red shifted Q band nearly 8 nm compared to cpd A in solvents, due to the e^- -withdrawing nature of sulfonyl groups in compound

Table 1 Antimicrobial of compound A and B

Compound	Zone of inhibition test (mm)			
	<i>B. subtilis</i>	<i>E. coli</i>	<i>S. aureus</i>	<i>S. pneumoniae</i>
A	23	18	27	24
B	35	24	35	28
DMSO	0.0	0.0	0.0	0.0
Standard (Ciprofloxacin)	36	36	37	39

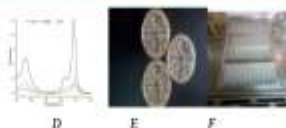


Figure D UV-visible of phthalocyanine, Figure E, Zone of inhibition for microbes, Figure F showing double dilution for compound A and B against microbes

Materials and Methods



Conclusion

In this present work compound A and B were successfully synthesized by use of microwave thus reducing the amount of solvent being used. The compounds were analyzed with FTIR, C-NMR and H-NMR. The compound were conjugated with synthesized silver nanoparticles (analyzed using TEM and SEM) and tested for antimicrobial. The study showed lack of bacteria growth and confirmed successful bacteria inhibition.